Investigation of ABS-Paraffin Based 3-D Printed Hybrid Rocket Fuels

Jacob Bresler

Investigation of ABS-Paraffin Based 3-D Printed Hybrid Rocket Fuels

Research Thesis

Submitted in Partial Fulfillment of the Requirements for the Degree of
Master of Science in Aerospace Engineering

Jacob Bresler

Submitted to the Senate of the Technion - Israel Institute of Technology

Av 5778 Haifa August 2018

The research for this thesis was performed under the supervision of Professor Benny Natan in the Faculty of Aerospace Engineering.

I would like to thank my parents, Mark Bresler, and Trudy Posner for supporting the choices that I have made that brought me to this point. Additionally, I would like to thank my father for being an example of an engineer for me to look up to as I grew up. I would also like to thank my entire family including my brother Joshua Bresler for supporting my decision to study in Israel as well as the moral support over the years when things got tough. I could not have gotten here without you.

I would like to thank my physics and engineering teachers from Council Rock High School South, Joseph Warwick and Fred Bauer. I already had a strong interest in physics, space and engineering when I started High school but your summer camp as well as your excellent instruction during my high school career had a strong lasting impact on my academic choices since graduation. Mr. Warwick, I still remember several of your mnemonics for physics equations, although one or two of them have not aged particularly well.

I would like to thank Benny Natan for his guidance and suggestions over the last two years, as well as for his patience during all the difficulties that were encountered over the course of this research. I know there were times during my time here where you were leaning towards suggesting that I change my research track but thank you for sticking with me when I chose to press onward.

I would like to thank everyone at the Fine Rocket Propulsion Center for making my time here enjoyable. In particular I would like to thank Professor Alon Gany and Daniel Kormornik for their quick suggestions when I encountered issues so that I could get them resolved quickly without having to schedule a meeting with Benny. Thanks to Doron Har-Lev for his assistance in designing the modification to the test stand as well as putting in the extended days during the testing period.

This Work was supported by the PMRI- Peter Munk Research Institute- Technion.

The generous financial help of the Technion is gratefully acknowledged**.**

Table of Contents

Table of Contents (cont.)

List of Figures

List of Figures (cont.)

List of Figures (cont.)

List of Tables

Abstract

Chemical rocket propulsion systems can be divided into solid, liquid, and hybrid propellant systems. Despite the numerous benefits that hybrid rocket systems enjoy over both solid and liquid propellant systems, their widespread implementation has not yet been achieved. This is due to the low regression rates of classical non-liquefying hybrid fuels, as well as the poor mechanical properties generally possessed by higher performance liquefying hybrid fuels.

Previous works into improving the mechanical properties of liquefying fuels, such as paraffin, generally were limited to the blending of the paraffin with polyethylene, which does provide some improvement, but also slightly decreases the regression rate of the paraffin fuel. Only one case of the attempt to utilize paraffin with an internal skeleton manufactured through additive manufacturing technology was found; however, that research was focused on the use of swirl flow to improve the regression rate, and actually caused a slight decrease in regression rate of the paraffin fuel. Therefore, any research into the use of internal skeletons to improve the performance of paraffin should be considered novel.

This research presents an investigation on the effect of the addition of an internal skeleton composed of acrylonitrile butadiene styrene (ABS) on the performance of a Paraffin/GOX hybrid propellant system.

The most important findings of this research were the significantly increased regression rate observed for the grains that possessed ABS structures when compared to the regression rate for grains composed solely of paraffin, this added regression rate was also accompanied by better mixing between the fuel and oxidizer, as well as a higher combustion efficiency. For the oxidizer fluxes studies the regression rates of the

ABS grain was approximately 0.2 mm/s, of the pure paraffin grain about 1 mm/s whereas for the ABS-paraffin structure the regression rate reached 1.4-1.6 mm/s, which seems to be a significant improvement.

The regression rate of hybrids has been one of the major hurdles that has held back its widespread implementation, the discovery in the mid 1990's of liquefying propellants allowed for new research that could allow for adoption of this safer and simpler chemical propulsion technology.

No research directly similar to the research detailed in this thesis has been reported in the literature. Additionally, these were the first experiments conducted at the Technion that utilize additive manufacturing to improve the performance of paraffin wax. This research provides new and original data.

Nomenclature

A- Area (m^2)

a- multiplication factor for power law correlations

ABS- Acrylonitrile Butadiene Styrene

C*- Rocket Characteristic Velocity (m/s)

CEA- Chemical Equilibrium Analysis

F- Thrust (N)

FDM- Fused Deposition Modeling

$F/\dot{m}_a$- Specific Thrust (m/s)

G- Mass flux $\left(\frac{kg}{m^2 \cdot s}\right)$

HIPS- High Impact Polystyrene

HTPB- Hydroxyl-Terminated Polybutadiene

I_{sp}- Specific Impulse (S)

l- Length (mm)

L/D- Length/Diameter ratio for fuel grains

LDPE- Low Density Polyethylene

$\dot{m}$ - Mass flow rate$\left(\frac{g}{s}\right)$

N- Integer number of walls in grain

n- Power Law Exponent for Solid and Hybrid Propellant regression rate

O/F- ratio between oxidizer and fuel mass flow rates

P- Pressure (bar)

PLA- Polylactic Acid

R- Gas Specific Gas Constant

RFNA- Red Fuming Nitric Acid

$\dot{r}$- Regression rate (mm/s)

SSME- Space Shuttle Main Engine

T- Temperature (K)

t- Time (s)

u- Velocity (m/s)

γ- Ratio between gas specific heats

ρ- Density (kg/s)

ϕ- Ratio of tested fuel to oxidizer ratio to stoichiometric value

Subscripts

f- Final

i- Initial

ox- oxygen

p- Paraffin

1. Introduction and Literature Review

1.1 Chemical Rockets Overview

Most modern chemical rocket propulsion systems can be classified as either solid or liquid propellant systems. Both of these technologies rely on the combustion of a fuel and an oxidizer both carried on board the vehicle to provide the energy required in order to propel the vehicle. The fuel and oxidizer can be mutually referred to as the propellant.

Chemical rocket propulsion systems differ from airbreathing propulsion systems such as turbojets, and ramjets in that they carry all of their oxidizer on board and do not intake it from the surroundings. One of the more important factors in designing a propulsion system is its propulsive efficiency, which can be measured in among several other metrics, the specific impulse (I_{sp}) or the thrust of the system divided by the mass flow rate of the on-board fuel and oxidizer. Since airbreathing systems get most if not all of their oxidizer from their surroundings, they can obtain significantly higher specific impulses than chemical rocket propulsion systems as can be seen in Fig. 1.

However, chemical rocket propulsion systems do have several benefits over airbreathing systems. The first is that they are not limited to certain flight speed regimes, as airbreathing engines are, as can be seen in Fig. 1. This is due to the various methods used to compress the inlet air in airbreathing engines, which are only efficient or even usable at certain flight speed regimes.

An additional parameter that limits airbreathing propulsion systems is the specific thrust defined as $F/\dot{m}_a$. This parameter determines the maximum drag that can be overcome by the propulsion system; it is infinity for rocket propulsion systems since they intake no air. Because of this rocket propulsion systems do not have a maximum cruise speed, other than the one imposed by the structural limitations of the rest of the system.

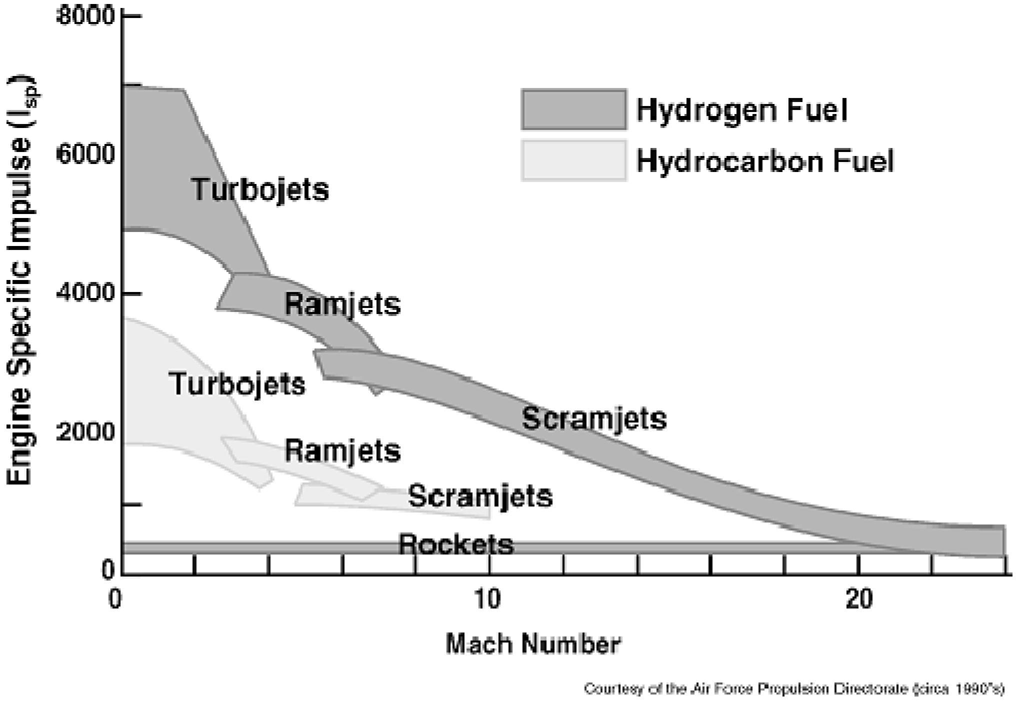

Figure 1 Isp vs Mach, and general operation regimes of various propulsive systems (Air Force Propulsion Directorate 1990's).

1.2 Solid Propellant Rockets

1.2.1 Solid Propellant Introduction

Solid Propellant Rockets contain their propellant combination in a single solid phase. Combustion occurs at the outer surface of that solid phase once the ignition temperature has been reached. The reaction rate at the burning surface and the surface area size determine the total amount of mass exiting the engine. The reaction rate of solid propellants is determined by the fuel and oxidizer ratio, as well as the chamber pressure, the equations generally used to calculate the regression rate and resultant mass flow can be seen in Eqs. (1) and (2) respectively (Hill and Peterson 1992), the values of a and n vary depending on propellant composition and are determined experimentally. It should also be noted that since the flow in the chamber is also choked at the nozzle, the pressure in the chamber will depend on the mass flow rate from the propellant according to Eq. (3) (NASA Glenn Research Center), this means that sudden increases in the burning area of the grain will result in corresponding increases in chamber pressure. This will then cause an increase in the regression rate and this cycle can very easily result in a catastrophic failure of the casing. In addition, values of n above 1 also indicate that a propellant will result in a catastrophic failure.

$$\dot{r} = a \cdot P_c^n \tag{1}$$

$$\dot{m} = A_b \cdot a \cdot P_c^n \cdot \rho_P \tag{2}$$

$$\dot{m} = \frac{A_t P_t}{\sqrt{T_t}} \sqrt{\frac{\gamma}{R}} \left(\frac{\gamma + 1}{2}\right)^{-\frac{\gamma+1}{2(\gamma-1)}} \tag{3}$$

End burning propellant grains provide a constant surface area, therefore, they provide a relatively constant thrust. Any variances in thrust of an end burning grain will occur due to an increase in the volume of the chamber that is not occupied by the solid propellant grain, which could cause efficiency losses over the duration of the burn. Increasing the burning area is possible by adding a port through the grain; however, as can be seen in Fig. 2, a cylindrical port will provide a progressive thrust profile, or a thrust profile that gradually increases as the grain burns, due to the increasing surface area of the reacting surface. A neutral or relatively constant thrust profile can be achieved through a star shaped port or a rod and tube port, however, it is generally easier to cast a star shaped port, so that port geometry is more commonly used. Double anchor, or cross shaped ports (4 and 5 in Fig. 2 will provide different thrust profiles, however both would be classified as regressive, since the thrust decreases with burning time due to the decreasing burning area. A cog shaped port such as is seen in grain 6 in the figure provides a high initial thrust and then rapidly drops to a relatively constant lower thrust.

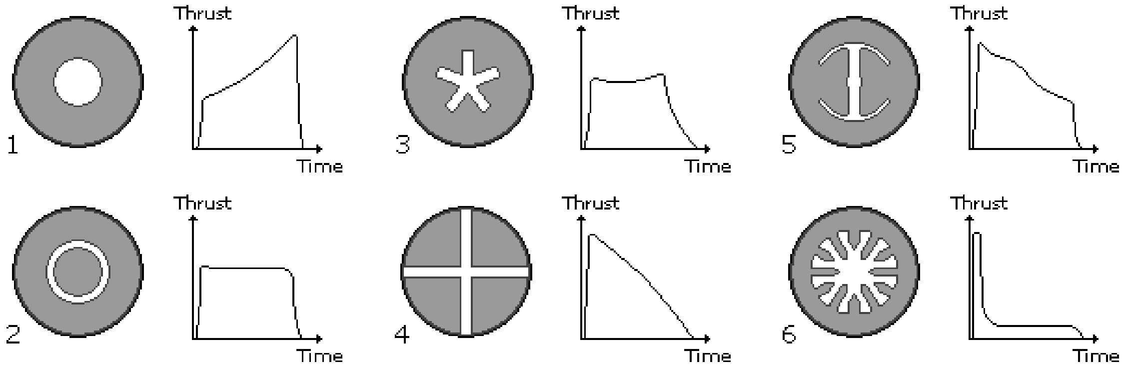

Figure 1.14

Figure 2 Port geometries for various thrust profiles (Raiano 2013).

1.2.2 Solid Propellant Rocket Advantages and Drawbacks

Solid propellants have many advantages over other chemical propulsion classes. One of their largest advantages is their storability, provided proper storage conditions, it is possible to store solid propellant grains for several years with them remaining in a state that allows for them to be used with a relatively short setup time. Additionally, unlike liquid or hybrid systems, no system is required to pump a liquid into the combustion chamber, as both propellants are stored in a solid form in the combustion chamber. Another benefit that solid propellants have is that they generally provide a higher thrust to weight ratio than liquid and hybrid systems, at the cost of a lower specific impulse due to the higher molecular weight of the exhaust gasses, as well as a lower heat of reaction. Finally, since solid propellants are in a solid phase after casting, it is possible to add performance-enhancing materials such as powdered metals, of which Aluminum is most commonly used in order to improve their performance characteristics. However, despite these benefits, there are several drawbacks to solid propellants, many of which are related to safety and reliability of the systems. The first drawback is that since the regression rate of solid propellants are strongly tied to the chamber pressure, small cracks or imperfections in the grain, which increase the burning area can cause a spike in chamber pressure. This can lead to a spike in burning rate, which will rapidly cause the pressure to exceed the maximum operating pressure, and will cause the motor to explode. Additionally, aside from changing the port geometry as was previously discussed, there is no way to throttle a solid propellant rocket, solid propellants also lack stop and re-start capability. A simple schematic of a solid propellant system can be seen below in Fig. 3. (Science Learning Hub)

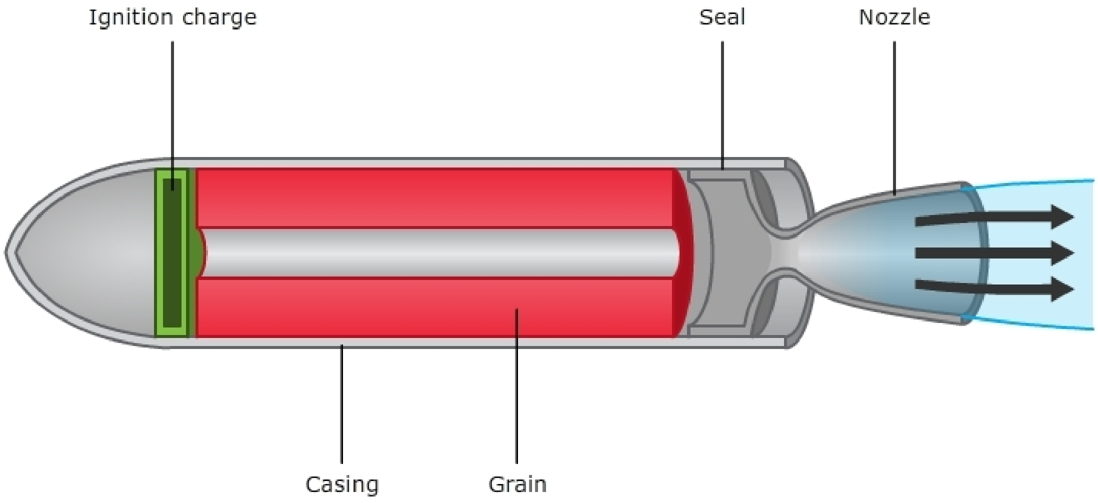

Figure 3 Schematic of a solid propellant rocket (Science Learning Hub).

1.3 Liquid Propellant Rockets

1.3.1 Liquid Propellant Rocket Introduction

Liquid Propellant Rockets store their propellants in liquid form in a storage tank and then pump and inject it into the combustion chamber as it is needed. Two subclasses of liquid propellant systems are in common use, these are the mono-propellant and bi-propellant liquid propellants. In a mono-propellant system a single working fluid is utilized, common mono-propellants are highly reactive liquids that are passed over a catalyst bed in order to be decomposed and then ejected through the exhaust nozzle. Unlike mono-propellant systems, bi-propellant systems consist of a fuel and an oxidizer that are both pumped into the combustion chamber in a pre-set O/F ratio, which is not always stoichiometric as peak performance can sometimes be obtained in a fuel rich O/F ratio. One specific example is the SSME, which ran fuel rich in order to obtain a higher I_{sp}.

1.3.2 Liquid Propellant Rocket Advantages and Drawbacks

Unlike Solid Propellant Systems, Liquid propellant systems can be easily throttled by changing the mass flow rates of the propellants. Additionally, unlike solid propellant systems, liquid propellant systems can be shut down by simply shutting off the flow of the propellants into the combustion chamber, they can also be restarted as long as a suitable ignition system is in place. This is best demonstrated by the Merlin Engine utilized on the Falcon 9 Launch Vehicle, during the launch and recovery process of the Falcon 9, the engines on the booster can be shut down and re-started several times during a single launch.

As was stated previously, two different sub-classes of liquid propellants are in common use in the industry. Mono-propellants typically have lower performance characteristics than even solid propellant systems as they derive their chemical energy from the decomposition of a single chemical rather than combustion of a fuel and oxidizer; however, they still enjoy the benefits of liquid systems in that they can be shut down and restarted, as well as throttled. Additionally, as there is only one liquid that needs to be moved from the storage tank to the decomposition chamber, they are significantly simpler than liquid bi-propellant systems. As such, they are commonly used in systems where simplicity and reliability are the most important factors in design, and some efficiency can be sacrificed, such as attitude control systems. Some commonly utilized mono-propellants include Hydrogen Peroxide, which is highly reactive and has handling restrictions as such, and Hydrazines, which are both highly reactive and highly toxic and as such are very difficult and expensive to handle.

Liquid Bi-Propellant systems on the other hand enjoy the highest performance characteristics of any commonly used chemical propulsion method. However, this performance comes at the cost of significantly more complicated plumbing systems in order to obtain the proper O/F ratio in the combustion chamber. Additionally, unlike in mono-propellant systems, there is a wider range of fuels and oxidizers that can be used. Certain applications of liquid bi-propellant systems also utilize highly toxic or reactive fuels and oxidizers such as Hydrazines, Red Fuming Nitric Acid, and Nitrogen Tetroxide. These propellants are commonly utilized due to their storability at non-cryogenic conditions as well as hypergolic ignition capability, which allow for their use on certain deep space missions where higher thrust capabilities are required. The highest performing liquid propellants also commonly require cryogenic storage, this requirement significantly limits their storability and therefore their usability on longer range missions.

Liquid propellants also have their own safety risks, including the fact that it is relatively easy for them to mix in combustible ratios in the case of a tank rupture. One of the most recent examples of this was the pad fire of the Falcon 9 in September of 2016, during the course of that incident one of the oxygen tanks on the Launch vehicle experienced a rupture in the presence of an ignition source, once this failure occurred it was likely exacerbated by the presence of the RP-1 fuel, once the fire was underway, it was extremely easy for the two propellants to mix and further combust, leading to significant damage to the Launch Pad.

A schematic of a liquid propellant system can be seen below in Fig. 4, when compared to Fig. 3, the added complexity of a liquid propellant system can be easily observed.

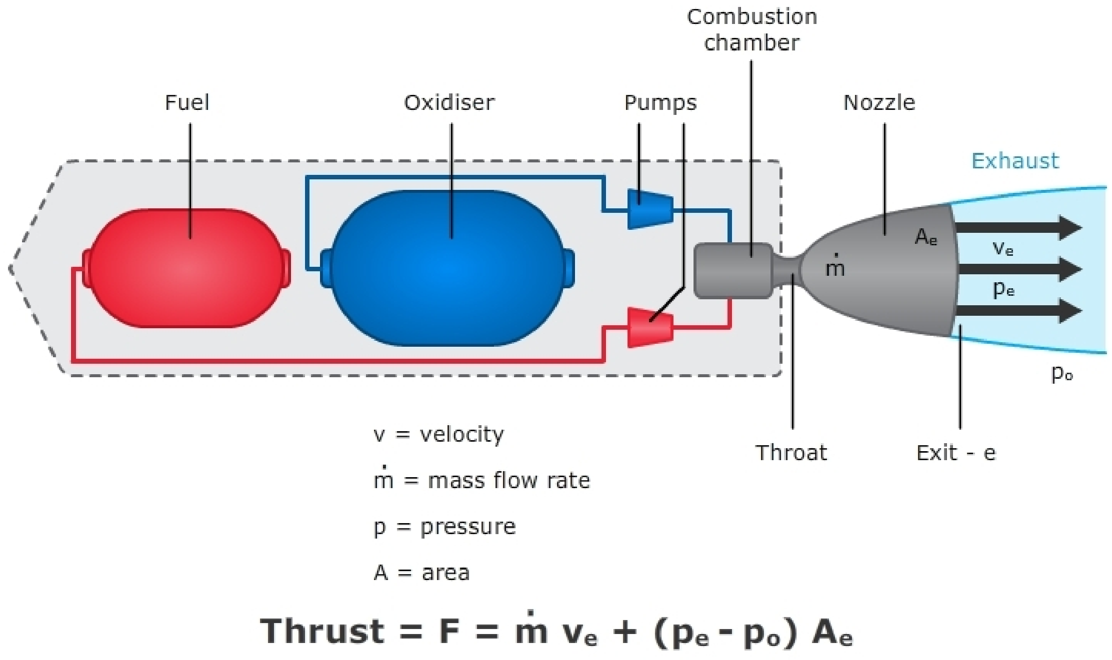

Figure 4 Schematic of a liquid propellant system (Science Learning Hub).

1.4 Classical Hybrid Propellant Rocket

1.4.1 Classical Hybrid Rocket Introduction

In general, most hybrid rockets use a fuel that is in solid phase, with an oxidizer that is in a liquid phase as can be seen in Fig. 6. Unlike in solid propellants, the regression rate in hybrid rockets can generally be characterized by Eq. (4), as can be seen, the regression rate is not tied to chamber pressure, and thus pressure runaway due to cracks in the grain cannot occur. It should be noted that for Eq. (5), due to the difficulty in measuring instantaneous radius of the grain, Eq. (4) is generally calculated using an average radius during an entire test. Additionally, since the oxidizer mass flow will generally be constant, but the fuel mass flow will vary with the instantaneous radius of the grain according to Eq. (7), the fuel to oxidizer ratio will not remain constant during the duration of a burn with the exception of the case where n=.5, in which case the radius term becomes equal to 1.

Classical Hybrid fuels generally consist of fuels such as HTPB, or several plastics or acrylics. In classical hybrid, the only location where fuel in the gas phase enters the flow is from the regressing surface of the fuel itself, and the rate at which this occurs is limited by heat transfer from the remote flame front back to the fuel.

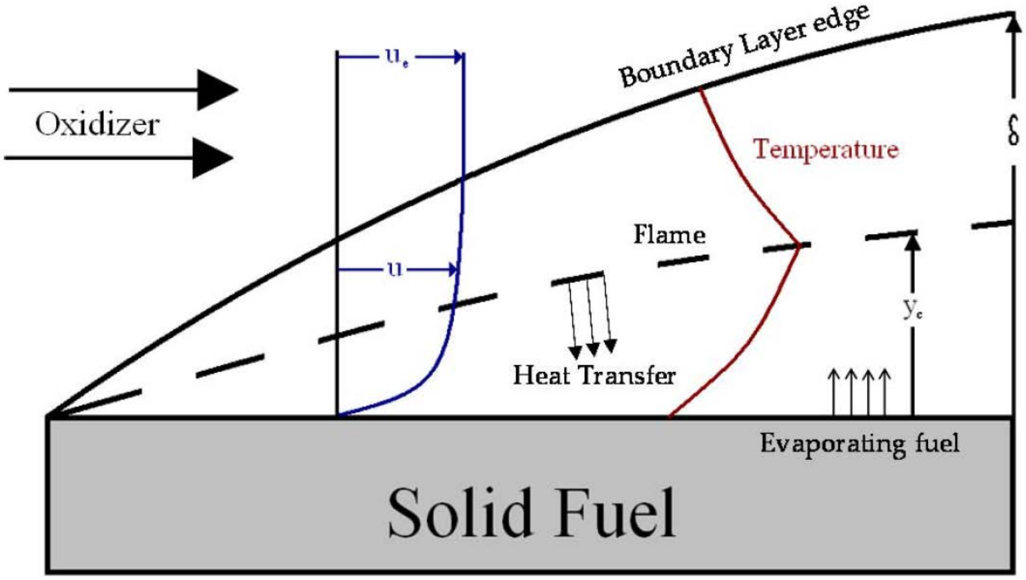

Figure 5 Schematics of the combustion within the boundary layer of a hybrid combustion chamber (Komornik 2014).

$$\dot{r} = aG_{ox}^{n} \tag{4}$$

$$G_{ox} = \frac{\dot{m}_{ox}}{\pi \cdot r_b^2} \tag{5}$$

$$\dot{m}_f = A_b \cdot \dot{r} \cdot \rho_f = 2 \cdot \pi \cdot r_b \cdot l_b \cdot a \cdot G_{ox}^{n} \cdot \rho_f \tag{6}$$

$$\frac{O}{F} = \frac{\dot{m}_{ox}}{\dot{m}_f} = \frac{1}{2} \cdot \pi^{n-1} \cdot r_b^{2n-1} \cdot l_b^{-1} \cdot a^{-1} \cdot \dot{m}_{ox}^{n-1} \cdot \rho_f^{-1} \tag{7}$$

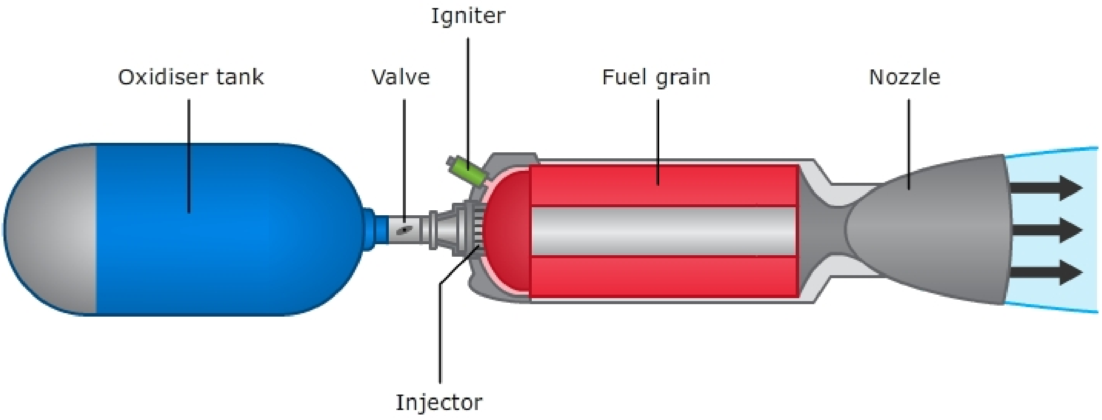

Figure 6 Schematic of a hybrid propellant system (Science Learning Hub).

1.4.2 Classical Hybrid Rocket Advantages and Drawbacks

Hybrid propellants exhibit several significant theoretical advantages over both solid and liquid propellants, as well as a few disadvantages. Hybrid propellants incorporate several of the advantages that solid propellants have over liquid propellants. Since the fuel is stored in a solid phase, performance enhancing additives such as metal particles can be suspended in the matrix. In certain cases, the performance of hybrid propellants using these additives can approach the performance of liquid bi-propellant systems. Additionally, since the fuel and oxidizer are stored separately, catalytic particles can be suspended in the fuel in order to obtain hypergolic ignition with suitable oxidizers such as Hydrogen Peroxide (Castaneda and Natan 2018). This is an advantage unique to hybrid propellants since hypergolic propellants in liquid propulsion are generally highly toxic.

Hybrid propellants also incorporate the relative simplicity of a liquid mono-propellant system, but possess significantly higher theoretical performance characteristics since the source of the heat is a combustion process rather than a decomposition process. Hybrid propellant systems can also be throttled, shut down and re-started in a similar manner to liquid propellant systems, which is an advantage over solid propellants. However, hybrid propellants also share the added complexity of mono-propellant systems over solid propellants.

In addition to the advantages and disadvantages shared with both solid and liquid propellants over each other, hybrid propellants have several unique advantages over both solid and liquid propellants. One of the most important advantage that hybrid propellants have over both solid and liquid propellant systems is a significantly higher safety factor. The safety factor over solid propellants is achieved by the separate storage of the fuel and oxidizer, which increases the difficulty of them accidentally mixing in a manner conducive to causing an uncontrollable fire. The safety factor over liquid propellants is achieved by the solid state of the fuel, which makes it much more difficult to achieve an accidental fire.

Unfortunately, hybrid propellants do have several drawbacks, the most significant of which is that the regression of the fuel is controlled by heat transfer from the flame to the fuel. In solid propellants the flame occurs very close to the propellant due to the fact that both of the propellants are pre-mixed, however, in hybrid propellants the flame front is significantly more remote due to the need for the fuel and oxidizer to diffuse towards each other until suitable conditions are achieved for combustion. In classical hybrid propellants this can significantly limit the regression rate of the propellant in comparison to solid propellants.

1.4.3 Improving Regression Rate of Classical Hybrid Rockets

Due to their limited regression rate, most work on improving the performance of Hybrid Propellants revolves around methods of increasing either the regression rate of the propellant, or the overall fuel mass flow into the total flow through the engine. The simplest method of increasing the mass flow is to increase the length of the grain; this method is infeasible as it results in very large L/D ratios in the grain and thus low efficiency in volumetric storage, as well as possible structural issues in the overall rocket.

Another method of increasing the fuel mass flow rate is to use multiple ports through the length of the fuel grain; this method dramatically increases the cross-sectional area of fuel available to regress and allows for shorter grains to achieve the same O/F ratios as longer single port designs. However, multi-port systems also have several significant issues, as with grains with high L/D ratios they do not have particularly good volumetric loading. Additionally, as the ports burn towards each other the grain can experience integrity issues, also for safety reasons, the fuel grains cannot usually be burned to completion leaving parasitic mass on the system. Finally, individual ports may not burn identically, and there is an increased risk of instabilities (Karabeyoglu et al. 2001).

Both of the previous methods of increasing the fuel mass flow into the oxidizer stream focused on increasing the mass flow without directly modifying the regression rate of the fuel, however there has also been significant work on directly increasing the regression rate of the fuel itself. In 1971, the effect of placing mechanical diaphragms was investigated on the regression rate of a polyester fuel with RFNA as the oxidizer. It was found that the diaphragms created a large local increase in the regression rate of the fuel immediately after the device itself, but that the overall regression of the fuel was largely unaffected (Gany and Manheimer-Timnat 1972).

Rotational flow through the port has also been found to increase the regression rate of hybrid fuel grains. Swirl can be induced through the injection, however, without structures in the grain itself, the effect of the swirl is generally localized to near the injector. Several papers have investigated the use of additive manufacturing techniques to create helical ports, or port structures that would otherwise maintain a rotational flow. These structures would generally be impossible to generate with conventional manufacturing techniques. Increased regression rates have been achieved, but the regression rate of the fuels is still below optimal, additionally, rotational flow can cause issues with traditional nozzles (Whitmore et al. 2015) (Lee et al. 2005) (Fuller et al. 2011) (Armold et al. 2013).

Other methods of improving either the heat transfer to the fuel grain or the heat generation at the surface of the grain such as was attempted through the addition of embedding metal wires in the grain, which is highly effective for solid propellants as was attempted by Shin et al. (2005). This method did not prove effective for hybrids as it did not improve combustion at the wire, and the heat transfer was highly localized (Shin et al. 2005). Another method of potentially increasing the regression of solid propellants was the addition of catalytic particles to the matrix in order to obtain decomposition of the hydrogen peroxide fuel and hopefully increase the heat in close proximity to the fuel as was attempted by Castaneda and Natan. This method slightly decreased the theoretical Isp of the system, however, it did enable for hypergolic ignition without the use of commonly used hypergolic propellant combinations (Castaneda and Natan 2018).

1.4.4 Classical Hybrid Rocket Examples

One of the most well-known operational vehicles that uses a conventional hybrid propulsion system is Virgin Galactic's Spaceship 2, which can be seen in Fig. 7. Spaceship 2 uses a multi-port HTPB grain with Nitrous Oxide as the oxidizer, and is capable of achieving sub-orbital flights after being deployed from the White Night 2 mothership. This is the successor to the Spaceship 1, which won the X-prize for being the first privately funded vehicle to carry passengers into sub-orbit twice in rapid succession.

Figure 7 SpaceShipTwo.

1.5 Liquefying Hybrid Rockets

1.5.1 Liquefying Hybrid Rocket Introduction

During the 1990's, investigation began into hybrid propellants that used either cryogenically frozen fuels or in some cases cryogenically frozen oxidizers with liquid fuels in what would be commonly referred to as a "reverse hybrid" fuel combination. These propellant combinations were initially of interest solely due to the expected performance increase that could be achieved with the particular fuel combinations; however, it was soon found that they exhibited regression rates in some cases of several hundred percent over classical hybrid fuels. This is suspected to be due to a process that results in the formation of a thick, hydrodynamically unstable liquid melted layer on the regressing surface of the fuel, which allows for droplets to be pulled into the general flow and be burned in a similar manner to fuel droplets in a purely liquid propellant system. Further investigation of this phenomena indicated that certain non-cryogenic propellants such as paraffin could also exhibit this behavior (Karabeyoglu et al. 2002a) (Karabeyoglu et al. 2002b).

1.5.2 Liquefying Hybrid Rocket Regression Model

As was stated previously, the commonly accepted method by which liquefying hybrid fuels obtain their increased regression rate over classical fuels is the formation of a thick hydrodynamically unstable layer of liquid at the melting surface, which allows for the entrainment of liquid droplets into the flow, as can be seen in Fig. 8. The primary properties linked to this hydrodynamically unstable layer is low viscosity and low surface tension of the liquid phase of the fuel, other commonly used fuels such as HDPE, which do melt but do not exhibit fuel entrainment do so because of their high viscosity and or surface tension.

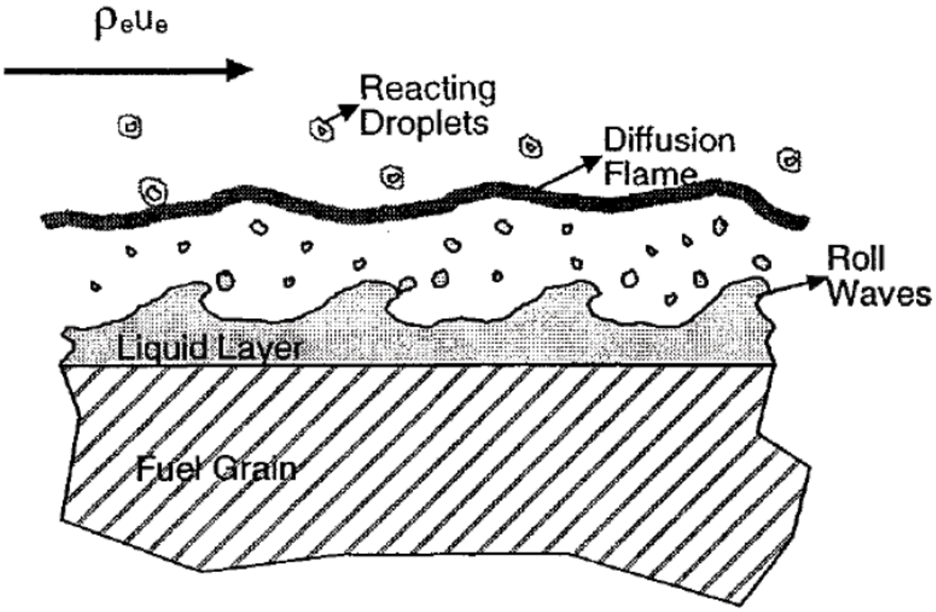

Figure 8 Fuel droplet entrainment mechanism (Karabeyoglu et al. 2001).

In addition to the fuel droplet entrainment that was theorized by Karabeyoglu et al. (2001), an additional mass loss mechanism has been proposed in which melted paraffin flows along the surface of the regressing surface but is not entrained into the flow. This results in either the accumulation of paraffin in the post combustion chamber of a stationary horizontal test stand. Or the likely ejection of additional unburned paraffin in a non-static case due to the acceleration forces, or simply the acceleration due to gravity in a vertical test scenario. Both of these scenarios cause a loss in performance since the paraffin is not being combusted properly. This model can be observed in Fig. 9 (Weinstein and Gany 2011).

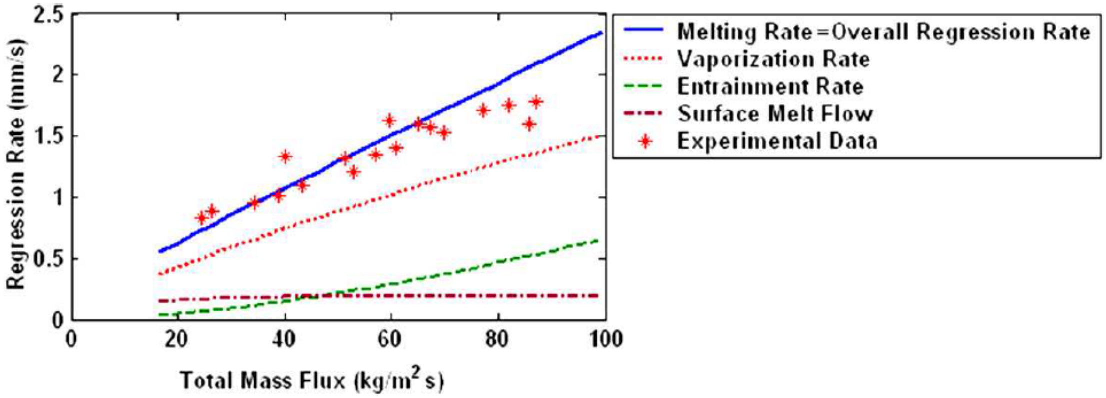

Figure 9 Paraffin regression model including surface flow (Weinstein and Gany 2011).

1.5.3 Liquefying Hybrid Rocket Advantages and Drawbacks

Liquefying Hybrid Propellants share all the previously stated advantages and drawbacks as classical hybrid propellants do over liquid and solid propellant systems. However, as was stated previously, liquefying fuels have regression rates several hundred percent those exhibited by classical fuels. This improvement in regression rate allows for single port grain designs that are much shorter than those required for classical fuels, removing the difficulties imposed by those methods of working around the low regression rates of non-liquefying fuels which were detailed previously.

However, this increased performance does come at a cost to the mechanical properties of liquefying fuels. The most commonly researched liquefying propellant is n-paraffin waxes, these waxes are mechanically weak, which can result in their inability to maintain their form under launch or storage loads.

1.5.4 Improving Structural Properties of Liquefying Hybrid fuels

The method by which the structural integrity of paraffin fuels can be improved which has been most extensively studied, is the blending of low percentages by mass of molten LDPE into molten paraffin. This was investigated by Kim et al. (Kim et al. 2010), who were able to successfully blend paraffin wax with LDPE at mass ratios up to 10% by weight, above these ratios they began to have difficulty with phase separations of the two blended materials. They were able to obtain relatively significant improvement in both the tensile and compressive strength of their fuel blends, increasing from 1.6 MPa to 2.2 MPa for tensile strength between pure paraffin and the 10 percent blend, whereas the compressive strength increased from 2.8 MPa to 3.9 MPa for the same blend percentages. They also performed slab burner experiments of the various fuel blends and found that the percentage of LDPE allowed for a certain amount of control over the fuel droplet entrainment rate and combustion efficiency of the fuels. They found that pure wax had the highest regression rate, however, the blended fuels obtained higher reaction rates with the flow as can be seen in Fig. 10, and Fig. 11.

Figure 10 Flame shape of pure paraffin wax (Kim et al. 2010).

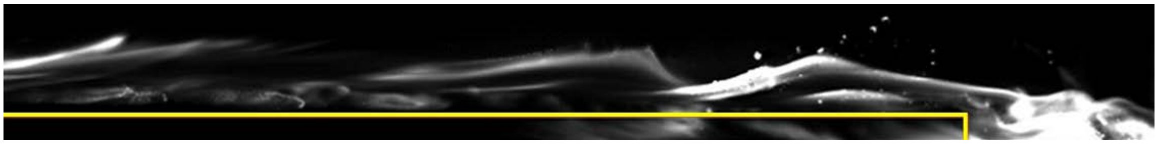

Figure 11 Flame shape of 90 percent wax 10 percent LDPE (Kim et al. 2010).

In addition to the testing of additive manufacturing technologies to improve the regression rate of classic fuels through the inducement of rotational flow, Armold et al. (2013) also investigated the effect of paraffin fuel grain reinforced with an acrylic like structure. These grains were manufactured through a material jetting additive manufacturing process, which used a paraffin-based material as support and a UV curable acrylic-like substance for the primary structure. In typical use cases, after manufacturing, the structure would be heated above the melting point of the paraffin and the paraffin would be drained through drainage ports. However, the drainage ports were designed to be too small to print and thus were not printed at all. This allowed for closed cells of acrylic like support structure to be manufactured around a paraffin grain. The focus of this research was the effect of rotational flow as well as turbulators on the regression rate of the paraffin, and for the most part, regression was negatively impacted by the addition of the acrylic structure (Armold et al. 2013).

1.5.5 Liquefying Hybrid Rocket Examples

As liquefying hybrid propellants are a relatively new technology, there is not a very large sample size of large-scale rocket systems utilizing paraffin based fuels. The most advanced system that is believed by us to have currently been developed is the Peregrine Sounding Rocket. This was an attempt to develop a sounding rocket utilizing a paraffin/nitrous oxide propellant combination. This program was started in October of 2006, and five project update papers were published starting in 2007. (Dyer et al. 2007) (Dyer et al. 2008) (Doran et al. 2009) (Ziliac et al. 2012) (Ziliac et al. 2014) The most recent of these status updates was published in 2014, at that time successful ground tests of the propulsion system were reported. No test flights have been reported.

1.6 FDM Fabrication Technology

1.6.1 Additive Manufacturing Introduction

Additive manufacturing techniques are beginning to see widespread adoption in the Aerospace field, from their use in the rapid generation of prototypes, to the use in some cases of parts of, or even entire propulsion systems manufactured through metal additive manufacturing techniques. Additive Manufacturing allows for the creation of structures that would either require expensive and difficult molds or tooling or be entirely impossible to manufacture through more traditional manufacturing techniques, as well as in certain cases, the ability to reduce the mass of material used while maintaining structural properties through the use of partially hollow structures commonly referred to as “infill”.

One commonly used method for additive manufacturing that is used for thermoplastics is Fused Deposition Modeling (FDM). In this method of additive manufacturing, a thermoplastic filament is extruded through a small heated nozzle and deposited in a layer by layer fashion in order to construct the final structure. It is also possible to add small solid particles to the thermoplastic filament during its manufacture in order to adjust the properties of the filament. One commonly used additive is wood particles, which are primarily used for hobby manufacturing as the final parts can be finished in a similar manner to actual wood. Another additive that can have a more practical purpose is carbon fiber. This additive can increase the tensile strength of the final part, as the carbon fibers will generally align with the print direction (Ning et al. 2015). There are also several commercially available filaments that contain metals such as bronze, or stainless steel. These filaments are currently used in a hobby setting for the finish that they allow, but there is no reason not to believe that metal powders such as Aluminum or Boron could be added to specially made filaments to be used in the manufacturing of fuel grains.

2. Background and Objectives of the present Research

2.1 Background

Hybrid propellant systems have significant theoretical benefits over both Solid and liquid propellant systems. They have significantly higher inherent safety than either of the commonly used rocket propulsion varieties. A hybrid system has the simplicity of a liquid mono-propellant system while having a theoretical I_{sp} more similar to that of a bi-propellant system. This performance can be further improved by the addition of solid performance enhancing particles such as aluminum, which can be stably suspended in a solid fuel, unlike in a liquid fuel. Additionally, catalytic particles can be suspended in the solid fuel to allow for previously non-hypergolic fuel combinations to be used in a hypergolic manner, allowing for higher ease of handling of the oxidizer. Hybrid systems also have the capability to be throttled, shut down and re-started, unlike solid propellant systems.

Historically, hybrid propulsion systems have been held back by the poor regression rates exhibited by classical fuels such as HTPB and LDPE. This poor regression rate is caused primarily by the fact that combustion for fuel grains composed of these fuels occurs only in a thin region near the surface of the grain. Additionally, the heat from that flame is remote enough from the regressing surface, so that heat transfer to the regressing surface is impaired. The combination of these factors leads to a poor regression rate, which can be compensated for in order to obtain a suitable fuel mass flow rate, however, the methods of compensation can lead to other issues some of which can be significant.

Liquefying fuels allow for a significantly increased regression rate when compared to classical hybrid fuels. This is due to liquid droplet entrainment in the flow, which allows the combustion to occur not just at the surface of the regressing fuel grain but in a similar manner to that of a liquid propellant system. However, despite their significantly improved regression rate, liquefying propellants have lower density and do not have comparable mechanical properties to classical propellants, two factors which have impaired their adoption in the industry.

Additionally, both the casting process of paraffin wax, and the fabrication of parts through additive manufacturing are non-hazardous, and therefore do not require specialized equipment to manufacture. This allows for the outsourcing of certain manufacturing tasks which could allow for significant cost reductions in the manufacturing process.

A performance comparison of the theoretical performance of several fuel and oxidizer mixtures can be seen in Fig. 12, Fig. 13, and Fig. 14. Methane was selected as a representative liquid fuel due to its increasing adoption in the industry, HTPB was included as it is one of the most commonly used solid fuels as well as being used for Hybrid systems, ABS and paraffin were selected due to their use in this research. Liquid oxygen was selected as it is a very commonly used oxidizer on launch systems, Nitrous Oxide was selected due to its common use in small scale systems as well as its use on the previously mentioned Peregrine sounding rocket, Hydrogen Peroxide was selected as it has been found to be capable of hypergolic ignition in hybrid systems through the use of catalytic powders. These simulations were performed with a 68.9 bar chamber pressure and a nozzle adapted to sea level. As can be observed, the theoretical C* and Isp of paraffin-based systems are only slightly inferior to methane based liquid systems, however this comes with much simpler plumbing, and does not account for the ability to add metal powders to the paraffin to further increase its performance. The $\rho \cdot I_{sp}$ of the paraffin-based systems far exceeds that of the methane-based systems due to the fuel density of paraffin being nearly double that of methane.

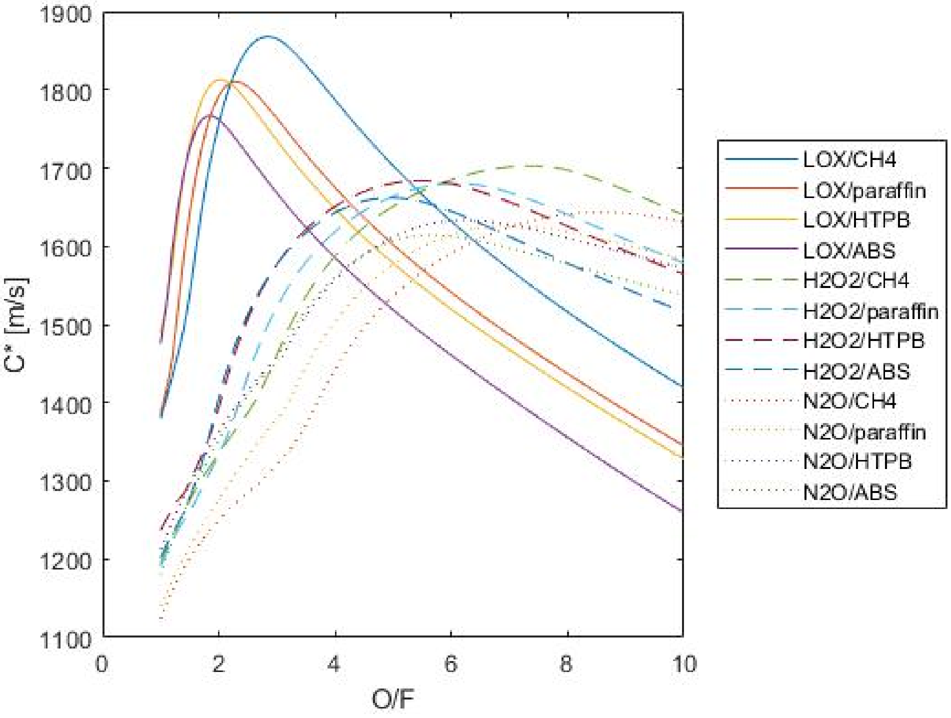

Figure 12 C* comparison for several fuel and oxidizer mixtures.

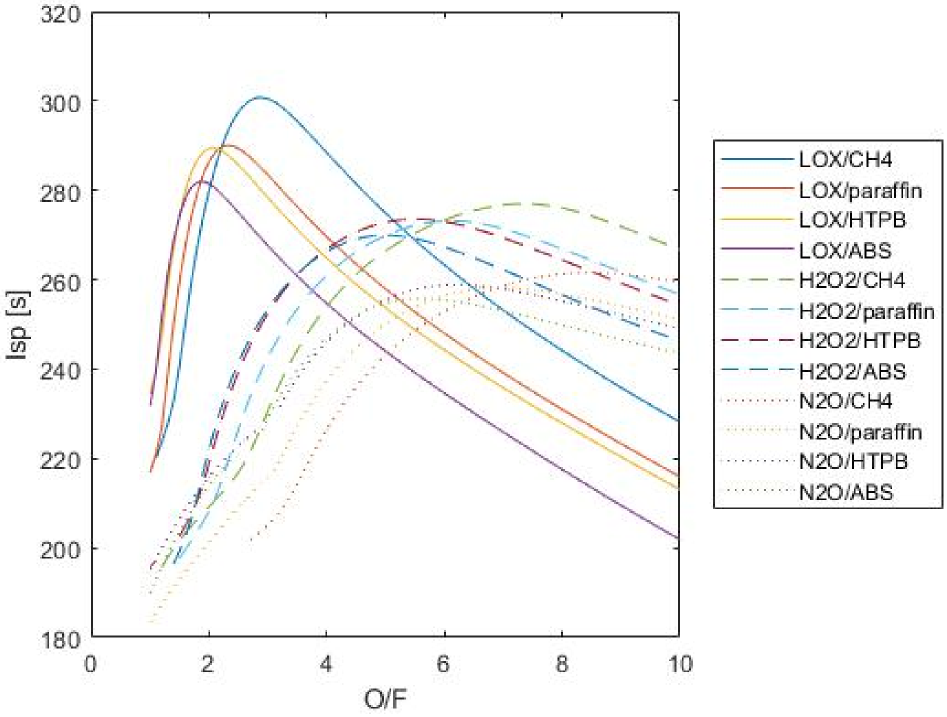

Figure 13 Isp comparison for several fuel and oxidizer mixtures.

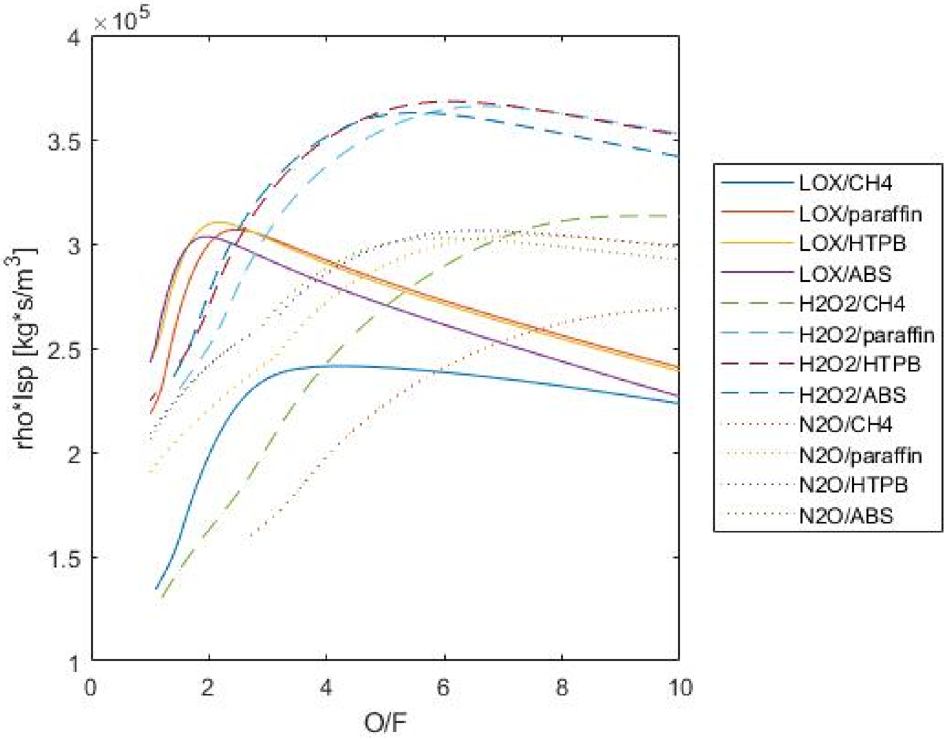

Figure 14 ρ*Isp comparison for several fuel and oxidizer mixtures.

2.2 Research Objectives

The objective of this research is to study the effect of adding a skeleton composed of ABS plastic manufactured through to a fuel grain composed primarily of paraffin. This research will be primarily focused on the effect of the skeleton on the regression rate of the paraffin, as well as the combustion and mixing efficiencies.

This topic was decided upon due to the novelty of the idea of using FDM technology to reinforce paraffin wax in order to increase its mechanical properties. Only one other paper was found where additive manufacturing processes were utilized to increase the regression rates of paraffin fuels, however that paper was primarily focused on inducing a swirl in the flow (Armold et al. 2013).

3. Grain Manufacturing Process

3.1 Manufacturing Difficulties Encountered

When this research was first started, the ABS skeletons were to be provided by Rafael Advanced Defense Systems Ltd., several skeletons had already been manufactured and tested; however, for various reasons, another source of printed skeletons quickly became needed. The task of finding an adequate and reliable method of obtaining 3d printed ABS skeletons was undertaken and eventually it was decided that the best course of action was to purchase a Raise 3D N2 plus dual extrusion printer for the laboratory and perform all manufacturing tasks on site, the printer can be seen in Fig. 15.

Figure 15 Raise 3d N2 Plus dual with Bondtech upgrade, without and with top enclosure.

The Raise 3d N2 plus dual utilizes the Fused Deposition Modeling (FDM) additive manufacturing technology. In this method of additive manufacturing, filaments of thermoplastics such as ABS or polylactic acid (PLA) are extruded through a heated extrusion nozzle and deposited in layers in order to manufacture the final part. In FDM manufacturing there are two common methods of dealing with structures that overhang previous layers with no material in the main structure to support them. The first method is to utilize temperature, extrusion speed, and print speed settings that allow for the structure to be printed with no additional support material, this method typically works for overhang angles up to 45^{o}-60^{o}, or for certain small overhangs of larger angles. For larger overhang angles, extra support material must be printed below the overhang in order to support it. This material can either be the primary extrusion material, which is subsequently removed through mechanical means after printing is completed or a secondary material that can be chemically dissolved after printing is completed with minimal damage to the primary structure.

Both ABS and PLA were originally considered for the support structures in the grains due to the fairly large general knowledge base around the settings required for their successful printing. ABS was ultimately selected for several reasons, the first and most important of which was its glass transition temperature of approximately 105^{o}C compared to PLA which can have a glass transition as low as 60^{o}C which would have been problematic with the casting process of the paraffin since the paraffin used in this research had a melting point of approximately 64^{o} C. The second reason was that ABS contains no oxygen in its chemical structure as it is composed solely of Hydrogen, Carbon, and Nitrogen as compared to PLA which is composed of Hydrogen, Carbon and Oxygen, the presence of oxygen in the fuel could have led to a quasi-solid combustion case where the regression of the fuel was tied to the chamber pressure which could lead to an unsafe situation during testing.

Due to several factors, it was originally believed that the skeletons could be printed as singular parts on the print bed using a soluble support material to support any overhangs on the ABS structure that could not be printed otherwise. The use of soluble support material was necessary for grains printed as single parts due to the impossibility of mechanically separating any support material due to the geometry of the grain. At the time the printer was purchased, the only commercially available soluble support material that was compatible with ABS in terms of printing temperature and adhesion properties was HIPS, which can be dissolved in Limonene. Due to the fact that Limonene also damages the Styrene component of ABS, attempts were made to find a method of satisfactorily removing the HIPS from the ABS with minimal damage to the ABS structure. The method that was attempted was as follows:

1. The portion of the grain containing HIPS was submerged in Limonene for no more than 1 hour
2. The portion of the grain that had been submerged in Limonene was then submerged in water in an attempt to dilute and rinse off the Limonene
3. The grain was suspended over a collection container in order to attempt to allow the liquid partially dissolved HIPS, which was highly viscous to drain from the grain

At this point in the research, grains with cone angles of 45^o, 60^o, 75^o, and 90^o were being attempted to more accurately test the effect of the cone angle on the regression. This method was successful for the grains that had 45^o cone angles, as the only parts of those that needed to be supported during printing were the very top, which was able to be supported from the cone directly below it. This allowed for relatively small amounts of HIPS to be required, and additionally, all HIPS that had been used on the entire grain could be submerged simultaneously in the 600 ml beakers that were being used for the removal process. All other grains were slightly less than twice the height of the 600 ml beakers and required two separate submersions in Limonene, and then two separate submersions in water before the suspension step in order to properly expose all of the HIPS to the Limonene. This resulted in some of the partially dissolved HIPS and ABS forming a solid ring at the water level, which could not easily be removed from the exterior and could not be removed at all from the interior. Additionally, as Limonene is flammable on its own, it was expected to possibly have an effect on the combustion of the ABS, it should be noted that one grain manufactured through this process was never cast, but the smell of the Limonene still remains over six months after exposure.

Due to the difficulties and issues related to using HIPS as a support material, when a new soluble support material came to market, called Hydrofill manufactured by Airwolf, which claimed to be soluble in water a decision was made to attempt to find a method to use it instead of the HIPS. Unfortunately, this material is very soft at room temperatures and becomes even more soft at temperatures above 50^0-60^0C, temperatures which the material can easily rise to due to the several heat sources during printing. This caused the material to be unable to be properly fed by the direct drive feed system employed on the Raise 3D N2 Plus, which resulted in several significant feed jams as can be observed in Fig. 16. This issue was unable to be resolved, although several methods including insulation of the feed path, as well as spacing of the motors from the feed assembly to limit heat transfer as well as allow for extra ventilation were attempted. Additionally, the Bondtech dual direct feed system upgrade was installed, partly in an attempt to resolve this issue, however it also jammed. Eventually, the Hydrofill support material had to be abandoned as unusable. We suspect that a printer utilizing a Bowden feed system would be capable of printing Hydrofill due to the feed system being remote from the heated extrusion nozzles as can be seen in Fig. 17.

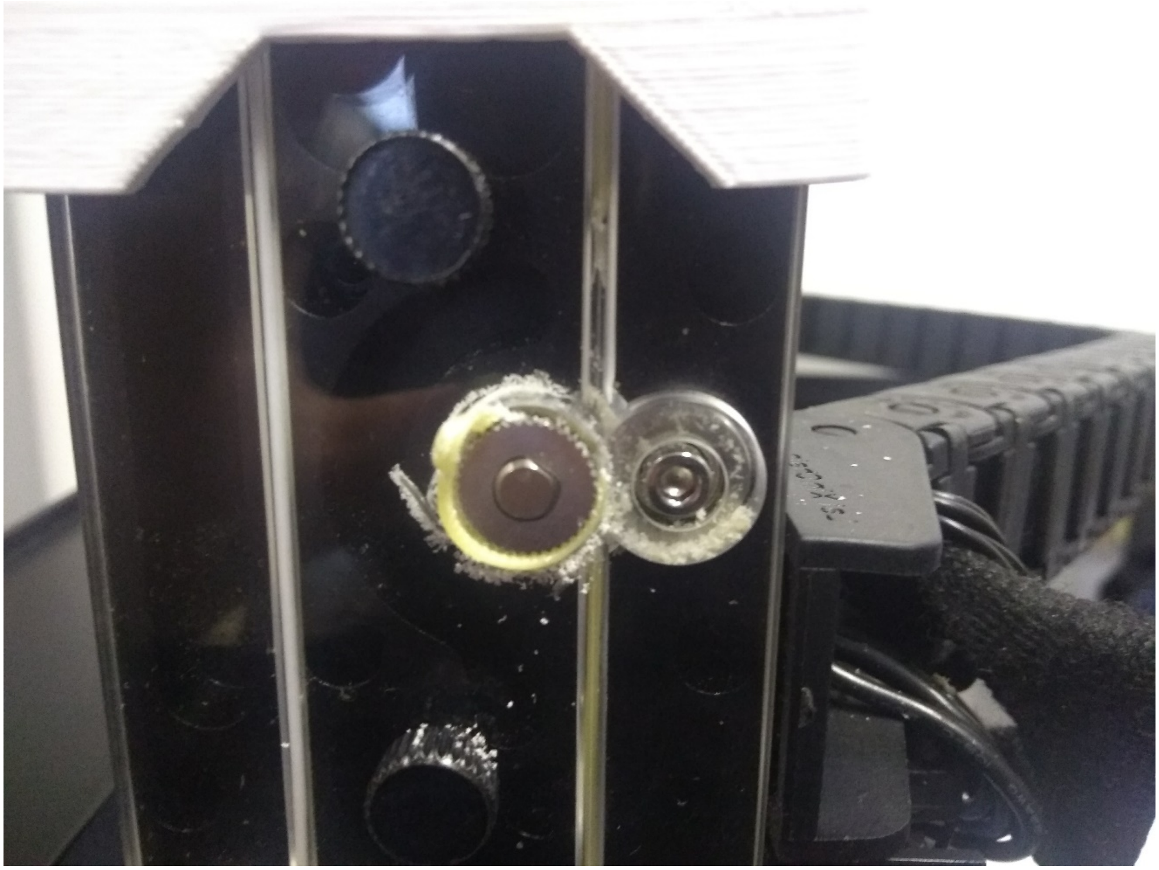

Figure 16 Hydrofill print failure.

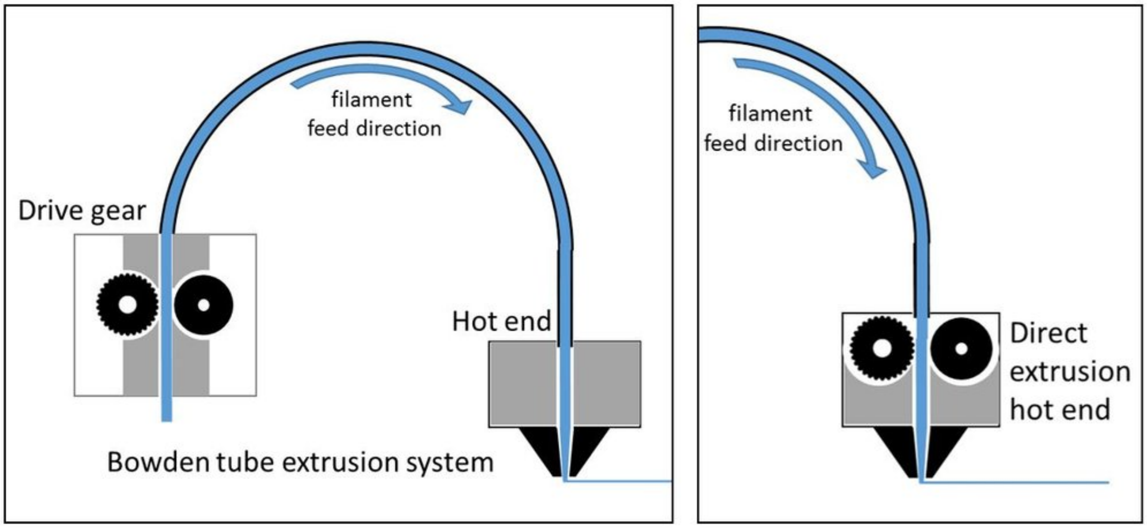

Figure 17 Bowden extruder vs. direct extruder (bowden extruder vs direct drive extruder).

Once it was determined that HIPS would be the only possible support material, it was decided to change the design of the support structure so that it could be printed in segments that would later be mechanically attached to each other. This was done in order to minimize the overhangs that required support material, as well as allow for the attempt to mechanically remove as much of the required support material in order to attempt to minimize the contact with Limonene. This did increase the thickness of the outer wall in order to facilitate the assembly of the structure, and thus increased the mass fraction of ABS in the overall fuel grain. However, it is known that the printing of overhangs is possible with industry standard FDM technology, as the initial skeletons provided by Rafael included overhang angles that were not able to be achieved with the commercially available printer that was used for the remainder of the manufacturing.

3.2 Final ABS Manufacturing Process

The results that will be presented in this Thesis were obtained using six different ABS structures. The simplest of these structures was a hollow cylinder with an outer diameter of 80 mm, an inner bore diameter of 23 mm and a length of 220 mm, this design was used in order to obtain the baseline regression rate curve for pure printed ABS, this grain is depicted in Fig. 18. The next two structures were designed in order to provide ABS end walls at either end of the skeleton, as well as 8 additional walls along the length of the grain at angles of either 45^{o} or 90^{o} to the end walls, additionally four walls were put at 90^{0} angles to each other that ran the length of the grains. Both of these skeletons were designed in such a manner that the distance between the walls at the 23 mm port were all the same, these skeletons can be seen in Fig. 19 and Fig. 20. Once it was determined that 220 mm length paraffin grains provided significantly higher fuel mass flows than stoichiometric, it was decided that grains of 50 mm length would be tested in order to provide the ability to test at values of ϕ that were close to 1. The same rules used in designing the 220 mm grains were used in that the distance between the walls at the 23 mm port would all be equal, but the number of non-exterior walls was reduced to 2, these grains can be seen in Fig. 21, Fig. 22, and Fig. 23. The reason for the design change between Fig. 21, and Fig. 22 was that we realized that we could eliminate the need for any support material in the manufacture of all of the parts.

All thin walls observed in all five skeletons were 0.8 mm wide and/or 0.8 mm tall in order to be easily compatible with the 0.4 mm extruder nozzle, and the 0.2 mm layer height that was used for the models. The maximum width of the outer walls was 4.2 mm, whereas the sections of the outer walls where interlocking occurred were 2 mm wide. This design decision was made in order to account for the nozzle width in the narrow segments while also affording a 0.2 mm tolerance between interlocking parts. Nozzle width did not need to be accounted for in the 4.2 mm sections of the walls since infill was utilized. The protrusions utilized on the interlocking sections also extended 0.4 mm from the main wall, again to account for the nozzle width.

Figure 18 Solid baseline ABS grain.

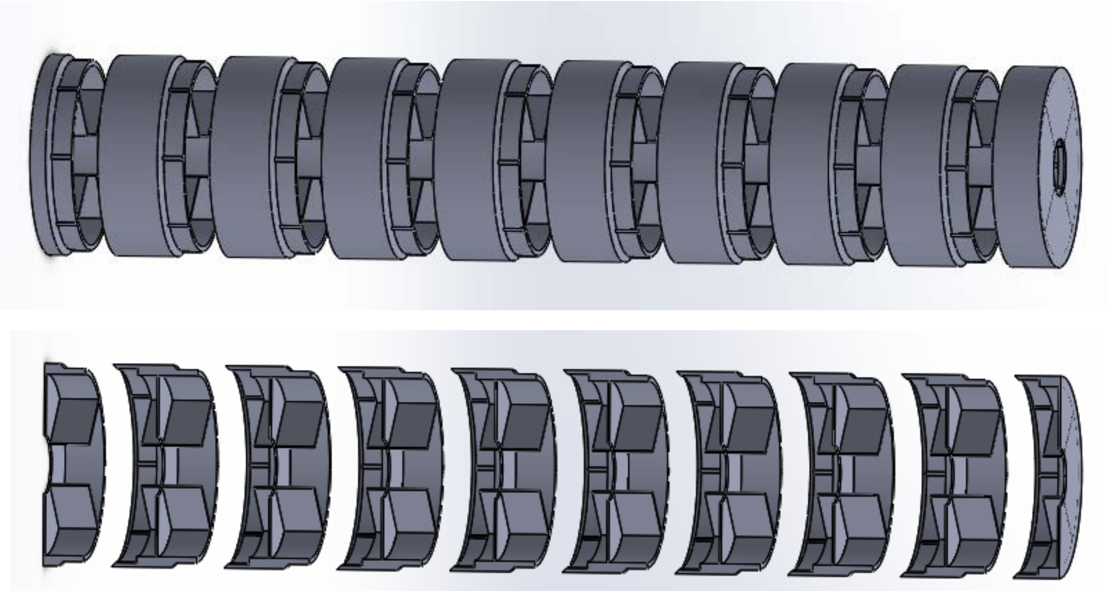

Figure 19 90° 220 mm skeleton.

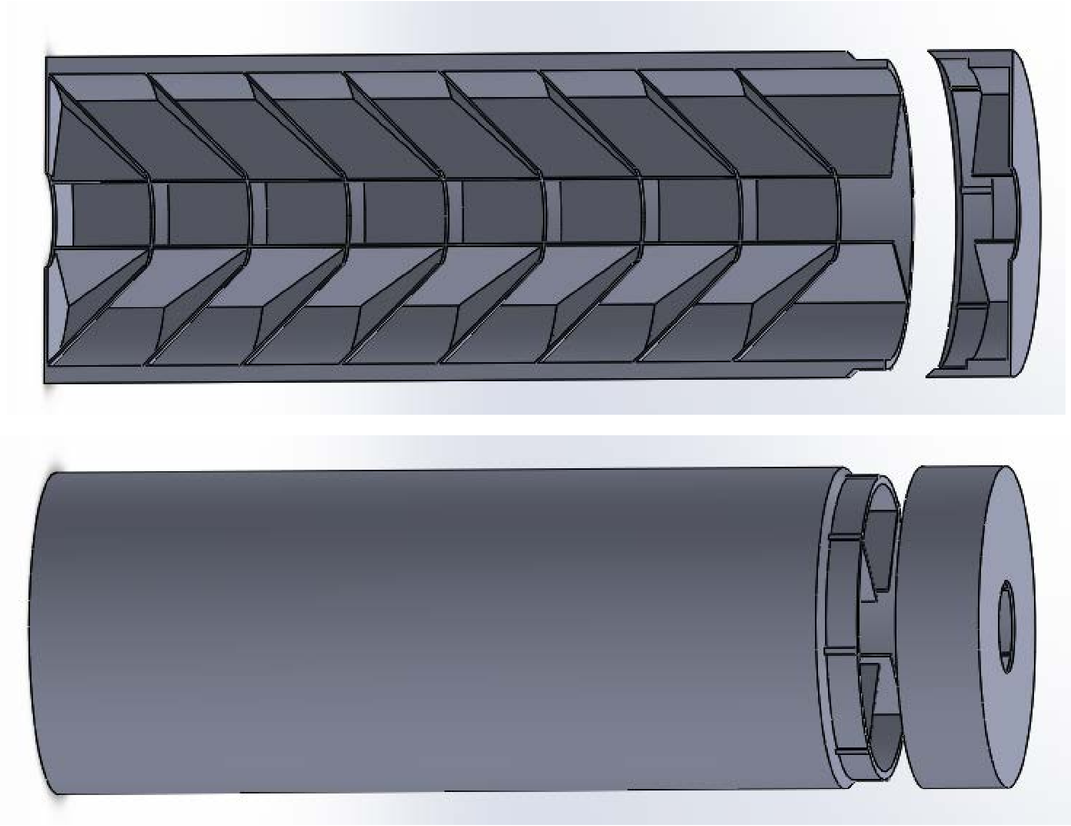

Figure 20 45° 220 mm skeleton.

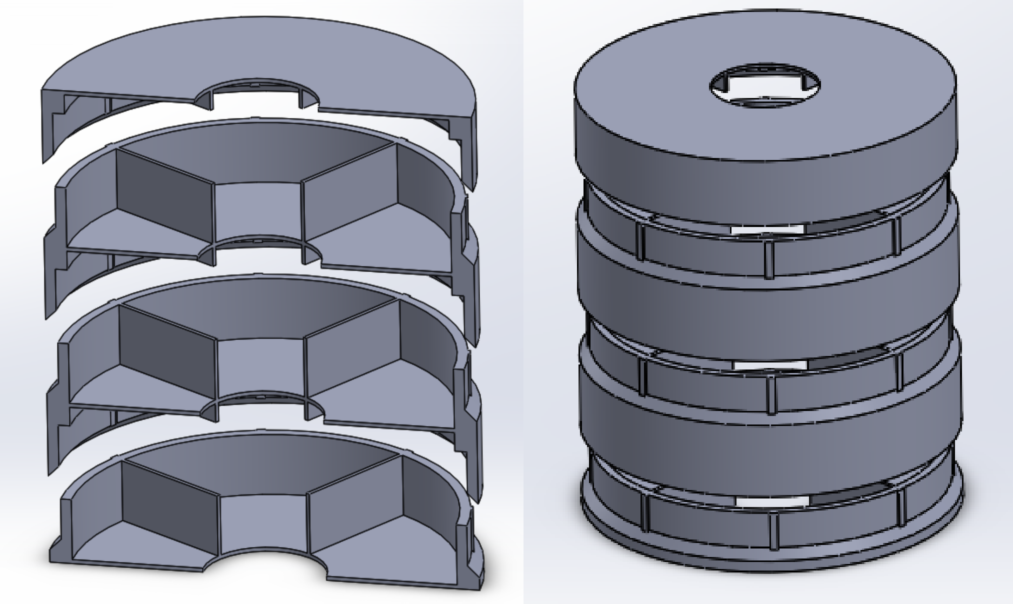

Figure 21 90^{o} 50 mm skeleton v1.

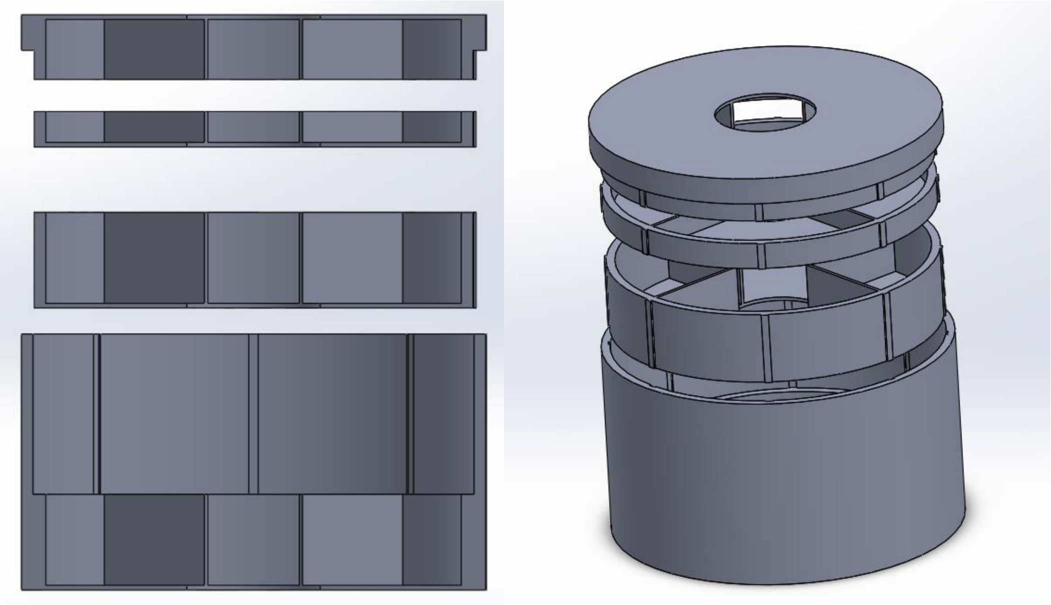

Figure 22 90^{0} 50 mm skeleton v2.

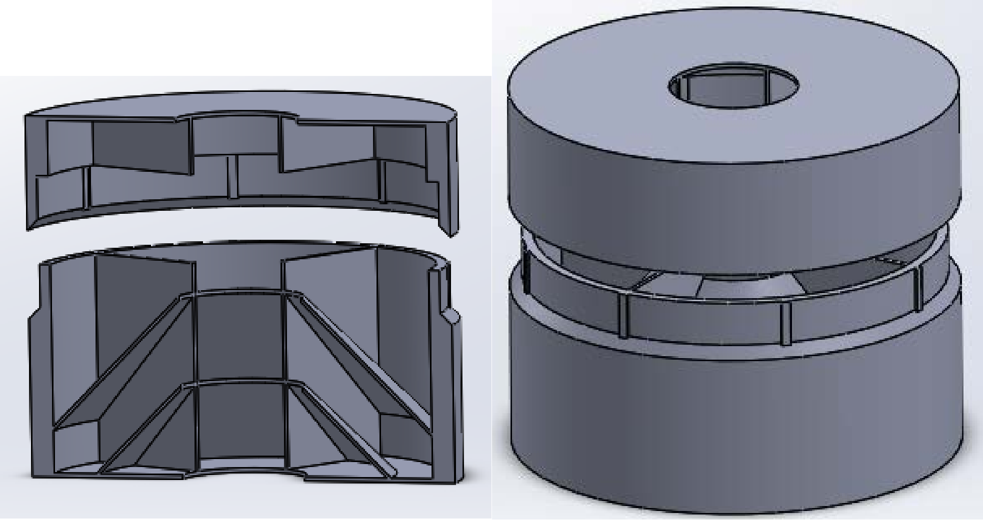

Figure 23 45^0 50 mm skeleton.

During the course of the research, the slicer that was used to generate the gcode files that were utilized by the printer was transitioned from Raise 3d's Ideamaker slicer to Simplify 3d. This transition was due to several factors, the primary of which was the reduction in print time, and access to features in Simplify 3d that had not yet been implemented in Ideamaker, which allowed for better printing results. The filament used was Filaform white ABS 1.75 mm diameter, and the following are the significant settings utilized in Simplify 3d.

- All models were printed with the use of an ABS raft in order to aid in bed adhesion.
- First layer was printed at 200% width in order to aid in bed adhesion.
- The print bed was maintained at 110 ^{o}C during the entire course of printing in order to aid in bed adhesion, as well as prevent warping of the ABS structure.
- Extruder temperature for ABS was 250 ^{o}C for raft.
- Extruder temperature for ABS was lowered to 230 ^{o}C for raft top layer and model first layer in order to aid in raft removal.
- Extruder temperature for ABS was 270 ^{o}C for all other layers of model.

- Layer height was 0.2 mm for all layers that did not include a 45° overhang, for layers that included a 45° overhang (only present on bottom segment of 45° skeletons) the layer height was lowered to 0.1 mm in order to avoid print failures.
- Outer walls were printed with 3 outline/perimeter shells, the rest of the walls were printed at 30% infill with a solid diaphragm every 20 layers. All infill was printed at .2 mm layer height regardless of other layer height settings.
- Infill was printed at 3600 mm/min, outline was printed at 1800 mm/min.

The only modifications that were made to the base Raise 3d N2 plus dual printer were the replacement of the stock feed system with the commercially available Bondtech Dual Direct feed system upgrade, as well as the thermal insulation of the hot ends through the use of Kapton tape in order to aid in their ability to maintain a constant temperature during printing.

3.3 Properties of ABS and Paraffin

The paraffin used in this research was PW-624, produced by Medina, LDA. and imported by Haifa Basic Oils. This paraffin has a Congealing point of 62-66 °C according to its material data sheet (Medina, LDA.)Due to the cited Congealing point of the paraffin, it is suspected that its chemical formula is $C_{28}H_{58}$, which also means that it has a boiling point above 400 °C (n-paraffins), additionally, it also has a density of 900 kg/m^3 at room temperature, although its molten density is approximately 780 kg/m^3 (Seyer et al. 1944). The theoretical calculations for paraffin combustion were computed using the built-in properties for crystalline CH_2 from NASA CEA.

ABS possesses a glass transition temperature of approximately 105 °C (Rahman et al. 2016). The chemical formula for ABS that was assumed is $C_{385}H_{485}N_{43}$, the heat of formation used for the NASA CEA calculations for the theoretical performance of ABS was 1097.4 kJ/mol. (Whitmore et al. 2011)

3.4 Casting of Paraffin into ABS skeletons

Once the ABS skeletons were printed and assembled, the next task was to fill them with paraffin Wax while also minimizing voids that could be produced by the significant difference in the volume of the solid and liquid phases of the paraffin. An additional difficulty that was encountered was caused by the poor heat conduction of paraffin while it is in solid phase, this poor heat conduction combined with the inability to control the temperature of the hot plate that was used to melt the paraffin led to the temperature of the molten paraffin generally reaching ~150 ^{o}C by the time all of the solid phase had melted, this issue was discovered when during the casting of two of the skeletons, the wax resulted in the damage seen in Fig. 24. This issue was easily resolved by the use of a thermometer placed in the molten paraffin, once the temperature was approximately 90^{o}-95^{o}C, the paraffin was able to be poured into the skeletons without causing damage, the various steps of this method can be seen in Fig. 25, and Fig. 26.

Figure 24 Grain damaged by overheated paraffin.

Figure 25 paraffin slabs (left), paraffin chunks (center), paraffin chunks in melting pot (right).

Figure 26 Molten paraffin with thermometer to achieve safe temperatures.

The following procedure was used when casting large batches of 50 mm grains, usual batch size included 4-5 90° grains, 8-10 45° grains, as well as anywhere from 10-16 previously burned solid ABS grains, which were filled with paraffin in order to be used for baseline testing.

Slightly different methods were used for the skeletons than for the baseline paraffin grains, the method detailed here was used for the skeletons. First, the bottom of the port was sealed with the use of fabric tape in order to prevent leakage of the molten paraffin, additionally the sides of the grains were also wrapped in fabric tape to ease in cleaning off excess paraffin so that the grains could be properly mounted on the lathe Fig. 30. Next a small amount of molten paraffin was poured into the bottom of each grain at a temperature of approximately 70 ^{o}C in order to fully seal the bottom, as the fabric tape did fail on some occasions. Once the seal was in place, molten paraffin was poured into each grain until it was full to the top with liquid, as the paraffin cooled and shrank, additional paraffin was poured into the port in order to maintain a slow cooling of the overall paraffin Fig. 29. All grains with cone angle of 45^{o} were cast with the tip of the cone pointing away from the ground in order to force the molten paraffin into the corner between the cone and the outer wall through gravity as the paraffin cooled.

For the paraffin baseline grains, the first task was to clean out the burned paraffin from the previous test, this was achieved through the use of a flat head screwdriver and a hammer, relatively low adhesion was observed between the paraffin and the ABS, as in multiple cases, the paraffin was able to be removed in large chunks, this can be observed in Fig. 27. Once the shells were cleaned, they were placed on a metal surface and each one was filled to a low level with low temperature molten paraffin in order to seal the bottom of the port. Once the port was sealed, they were filled to the top with paraffin, and again as with the skeletons, they were periodically topped off with additional paraffin to account for shrinkage.

Once the Paraffin was left to cool overnight, the final remaining task was to clean off the excess paraffin as well as drill the port. All cast grains required the manual removal of any paraffin from the outer curved wall so that they could be properly mounted on the lathe to be drilled with a 22.5 mm bit. However, differences did exist between the processing of the skeletons and the baseline grains. Due to the end walls on the skeletons, it was relatively simple to clean the grain ends off through the use of a box cutter. This also avoided any damage to the grains from the use of a lathe end mill.

This damage can be observed in Fig. 28; however, the baseline grains did not possess a clear end and additionally as long as the length was measured prior to test, it was not critical to be a precise length, so ends of the baseline grains were machined to be flat.

Figure 27 Pure paraffin grain before paraffin removal (left) cleaned of paraffin (center) paraffin removed from ABS (right).

Figure 28 Grains damaged by machining.

Figure 29 Grains on casting tray after filling (left) grains after being cleaned prior to machining (right).

Figure 30 Skeleton filled with paraffin and displaying fabric tape utilization in casting.

The theoretical mass of paraffin that should have been cast into each of the two ABS skeletons was calculated using the SolidWorks models with a 900 kg/m^3 density for the paraffin. The actual mass of paraffin was obtained by subtracting the mass of the ABS skeletons, which were weighed prior to testing from the mass of the grain immediately prior to the experiment. These results can be seen in Table 1. Test series 5 and 6 were omitted from the 90^o grains due to the fact that the ABS skeletons were not weighed prior to filling, so a paraffin mass could not be obtained. Test 15 for the 135^o and test 16 for the 45^o skeleton somehow provided a casting efficiency above 1 and test 19 for the 45^o skeleton was unable to be performed due to issues with the ignition system on the testing stand at high oxygen mass flow rates.

Table 1 Paraffin casting efficiencies in ABS skeletons

Test series	135^o grains	45^o grains	90^o grains
3	0.931	0.938	0.99
4	0.935	0.965	0.946
5	0.937	0.926	
6	0.915	0.929	
7	0.984	0.983	0.978
8	0.967	0.96	0.983
9	0.982	0.971	0.977
10	0.953	0.969	0.985
11	0.982	0.979	0.982
12	0.979	0.986	0.985
13	0.964	0.98	0.953
14	0.967	0.981	0.99
15	1.011	0.973	0.994
16	0.955	1.003	0.989
17	0.974	0.977	0.991
19	0.993		0.995
Average	0.965		0.981

The mass ratio between the ABS and the paraffin varies with scale as well as the number of baffles along the grain. Equation (8) shows the ratio between the area of the paraffin and the area of the entire port, this equation can be integrated from the initial port radius to the outer radius of the grain in order to obtain the ratio of the volumes which can then be easily converted to the mass ratio. As can be seen the ratio between the areas decreases with both radius and grain length, the value of n_{walls} is simply the number of walls along the length of the grain (for the 50 mm grains it was 4, for the 220 mm grains it was 10).

$$\frac{A_{paraffin}}{A_{total}} = 1 - \frac{4}{2 \cdot \pi \cdot r} \cdot \left(0.8 - \frac{n_{walls} \cdot 0.16}{l_{grain}}\right) - \frac{n \cdot 0.8}{l_{grain}} \tag{8}$$

4. Testing Process and Results

4.1 Experimental Setup

Multiple series of tests were performed at the Technion Sylvia and David I.A. Fine Rocket Propulsion Center. The variance of the diameter of the choked oxygen inlet as well as the exhaust nozzle allowed for a large range of oxygen mass flow rates, as well as multiple chamber pressures to be tested in order to rule out a pressure dependence in the fuel regression.

Due to the fact that the grains being tested were not directly compatible with the sealing system that was in use previously for the static firing test stand at the lab, as well as the fact that they could not be relied upon to support themselves structurally during the test firing, an adaptor was designed and manufactured in order to allow for the testing of the grains. The design drawings for this adaptor can be seen in Fig. 31, Fig. 32, and Fig. 33. The inlet and outlet adaptor plates are identical with the exception of the difference in the diameter of the central hole. The only change made when transitioning to the 50 mm grains was the manufacture of a tube of length 80 mm instead of the 250 mm shown in Fig. 32.

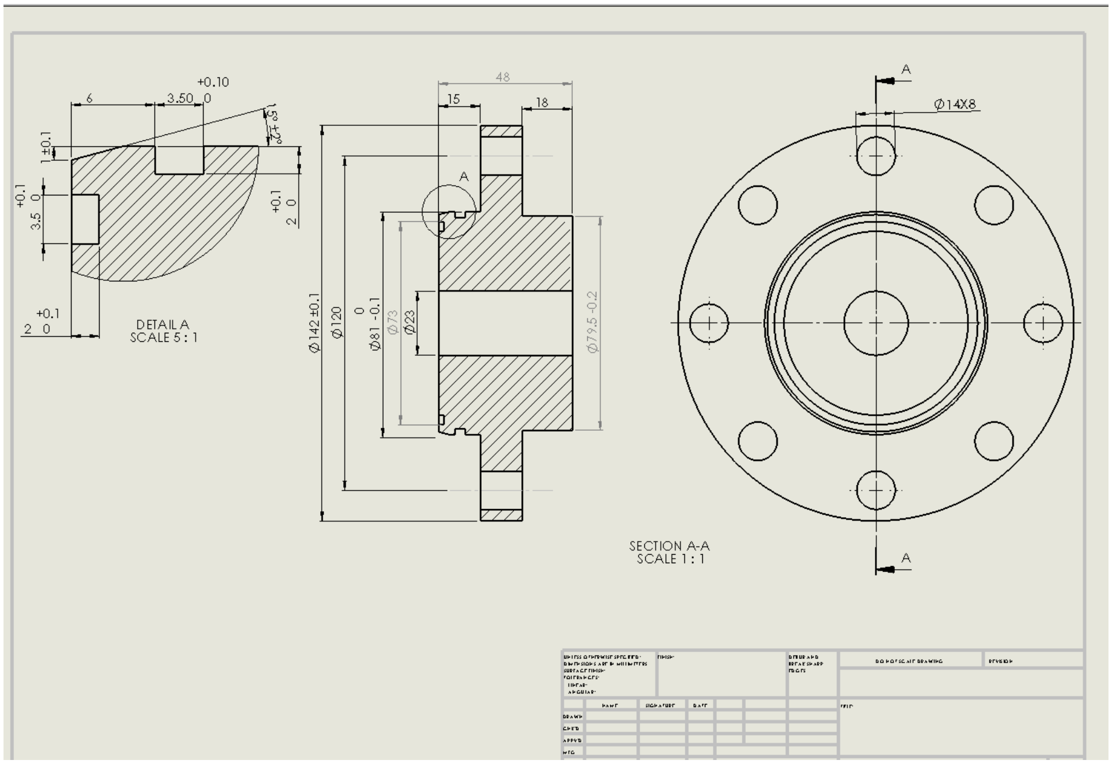

Figure 31 Inlet adaptor plate.

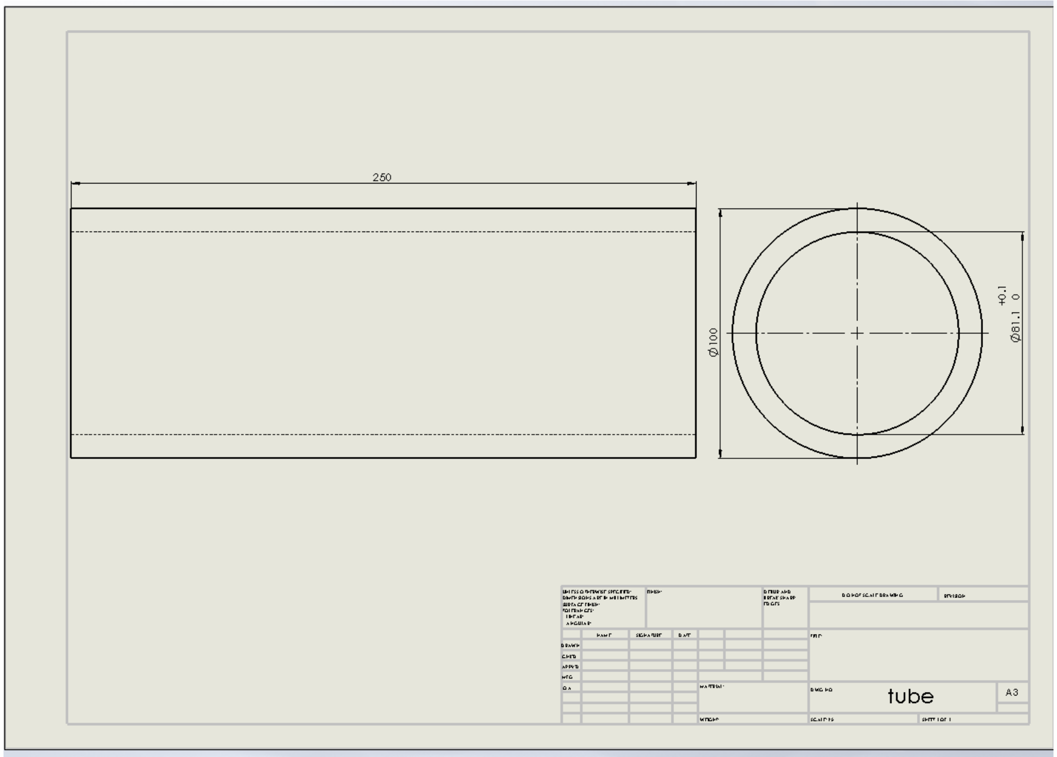

Figure 32 Tube for 220 mm grains

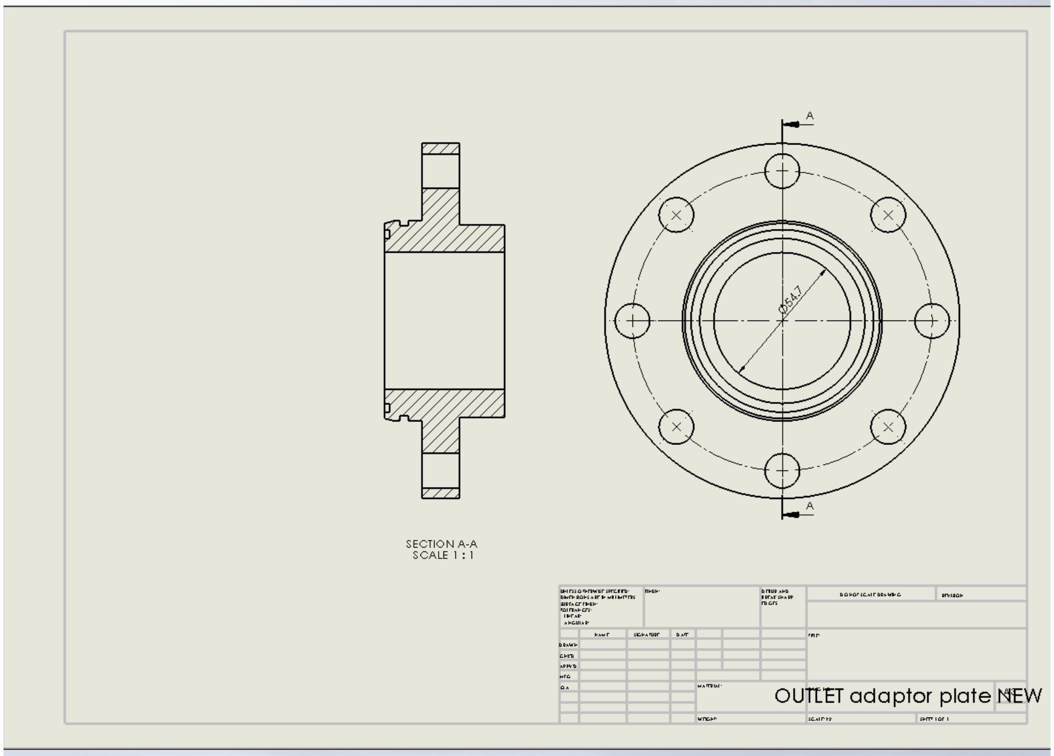

Figure 33 Outlet adaptor plate.

The experimental setup for the static firing tests consisted of a gaseous oxygen tank with a pressure regulator to allow for different feed pressures to be used, as well as an ethylene tank that was used for the ignition system. Both the oxygen and ethylene were independently choked at their injection points, additionally, a pressure transducer was placed immediately before the choked nozzle for the Oxygen in order to obtain a flow rate measurement. Ignition was obtained through the use of a spark plug placed before the solid fuel grain, along with a short burst of ethylene. The next section of the setup was composed of the adaptor and casing system that was designed for the grains used in this research. After the adaptor came a mixing chamber where a second pressure transducer was placed in order to obtain the chamber pressure reading. Immediately after the mixing chamber, a converging nozzle was placed in order to choke the flow in the combustion chamber. Finally thrust was measured through the use of an electronic force gauge. A full schematic of the test stand can be seen in Fig. 34, while photos of the two tested configurations (220 mm grains and 50 mm grains) can be seen in Fig. 35.

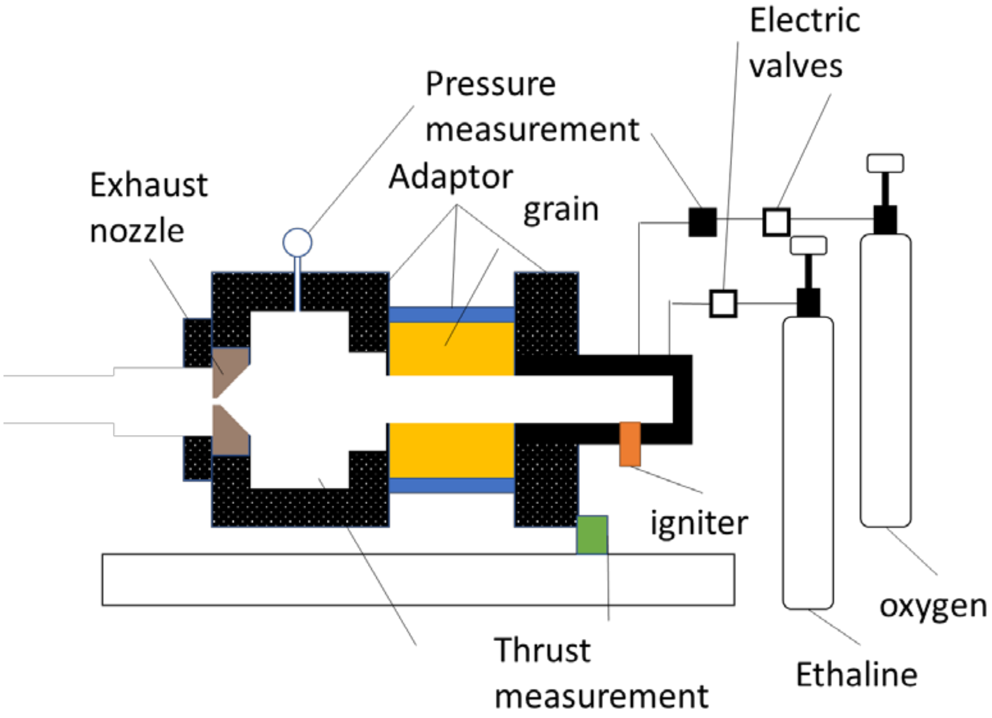

Figure 34 Schematic of test stand with adaptor.

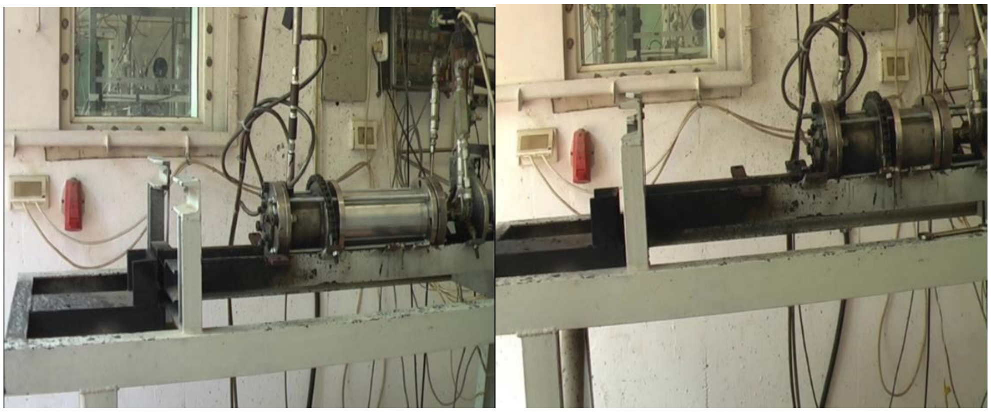

Figure 35 220 mm (left) and 50 mm (right) cases installed on test stand.

All data was acquired through the use of a Labview program, which also allowed for precise timing of the oxygen and ethylene valves, as well as the spark plug (Fig. 36). Oxygen mass flow was calculated according the choked flow equation using the instantaneous pressures obtained from the oxygen pressure transducer, which was situated immediately before the choked nozzle according to Eq. (9), temperature was assumed to be 300 K, since temperature is square rooted in the equation, small variances in external temperature should not have a significant impact on the mass flow rate of the oxygen. The instantaneous values were directly averaged for the calculation of G_{ox} for each test. Additionally, all grains were weighed before and after firing in order to obtain a value for the change in mass over the entire firing as can be seen in Fig. 37, and Fig. 38. The initial port diameter and length of the grains was also measured through the use of calipers in order to obtain a more accurate average regression rate. Finally, paraffin that accumulated in the mixing chamber instead of being ejected from the nozzle was weighed. This can be seen in Fig. 36. In some cases, this mass was a significant percentage of the total mass ejected from the grain, which could have a significant impact on efficiency calculations. It should also be noted that all grains containing paraffin fuel were refrigerated at a temperature of approximately 5^{o}C for a minimum of 24 hours prior to being fired, this was done in an effort to minimize the expected effect that initial temperature of the grains would have on the regression rate of the fuel.

$$\dot{m}_{ox} = \frac{A_t \cdot P_{ox}}{\sqrt{T_t}} \sqrt{\frac{\gamma_{ox}}{R_{ox}}} \left(\frac{\gamma_{ox}+1}{2}\right)^{-\frac{(\gamma_{ox}+1)}{2(\gamma_{ox}-1)}} = \frac{A_t \cdot P_{ox}}{\sqrt{300}} \sqrt{\frac{1.4}{259.8}} \left(\frac{1.4+1}{2}\right)^{-\frac{1.4+1}{2(1.4-1)}} \tag{9}$$

Figure 36 Data collection system, firing control box (left), and sample of unburned paraffin (right).

Figure 37 50 mm paraffin baseline grain before and after firing.

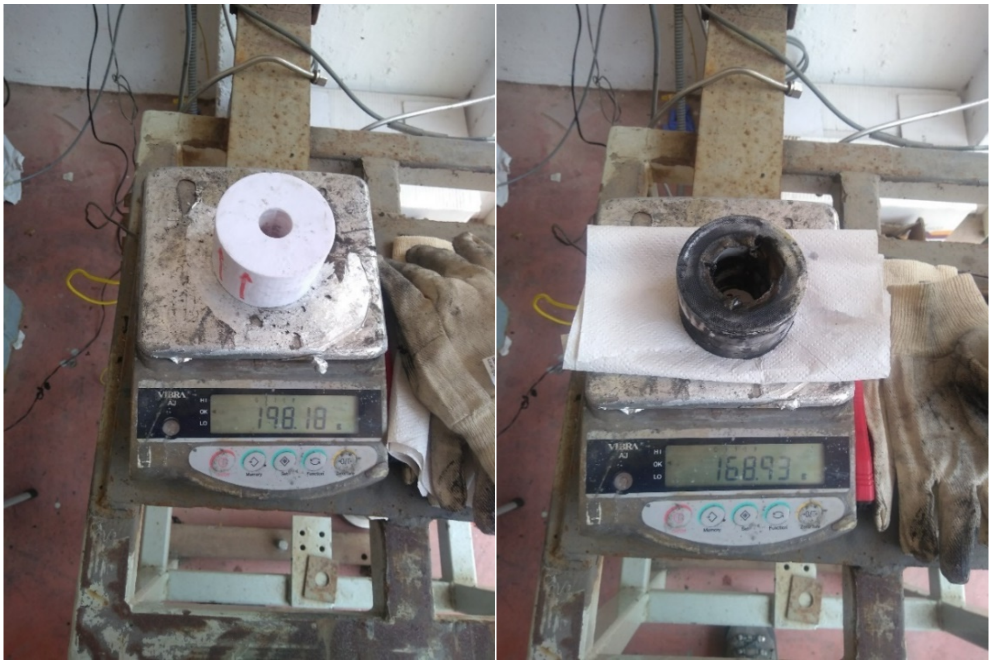

Figure 38 50 mm paraffin filled skeleton before and after firing.

4.2 ABS and Paraffin regression baselines

The first phase of this research was to investigate the performance of grains where the burning surface was composed solely of ABS manufactured through FDM techniques, or solely of paraffin cast into the burned-out shells of previously fired ABS grains. The primary value that was needed was a baseline for fuel regression rate that could later be compared to the values from the ABS skeleton grains. Additionally, in the paraffin baseline, C* efficiency and paraffin remaining in the mixing chamber (thus the mixing efficiency) were also relevant properties that were recorded.

For the baseline paraffin grains as well as the ABS baseline grains, a simple cylindrical approximation was able to be utilized to calculate an average final internal radius from the Δm through the use of Eq. (10). All radii for G_{ox} are the spatial average between the starting radius and the final radius of the experiment.

$$r_f = \sqrt{\frac{\Delta m}{\rho_f \cdot \pi \cdot l} + r_i^2} \tag{10}$$

$$\dot{r} = \frac{r_i - r_f}{t_b} \tag{11}$$

In order to obtain more data points without having to manufacture fresh ABS grains for each test, each grain was tested multiple times, as, due to the low regression rate, it was usually safe to test the grains up to 10 times each at test durations between 6 and 12 seconds. The results for the ABS baseline tests can be seen in Table 2 and Fig. 39, Grain 1 test 1 and grain 2 test 1 were both excluded due to being clear outliers, this appears to be related to the difference between burning a clean surface and a previously burned surface. Grain 3 test 1 was excluded due to a C* efficiency that was calculated to be above 1, indicating an error in measurement of either the oxygen mass flow or the start or end mass of the grain. Grain 4 test 1 and 3 were excluded due to O-ring failures during the tests leading to some exhaust gas leaking from the port seal and an unknown exhaust area. Grain 2 tests 5 and 8, as well as grain 3 test 8 were excluded due to being clear outliers from the remaining data.

Table 2 ABS regression data.

Grain 1	Test number	Exhaust nozzle diameter [mm]	Test duration [s]	Average chamber pressure [bar]	Average Oxidizer mass Flux [kg/(s*m^2)]	Average regression rate [mm/s]
	1	5.5	6.7	8.37	19.53	0.28
	2	5.5	6.8	9.37	19.58	0.23
	3	5.5	6.8	9.51	16.02	0.21
	4	5.5	6.8	9.1	13.45	0.19
	5	5.5	6.8	9.17	11.6	0.19
	6	5.5	6.7	9.33	10.45	0.18
	7	5.5	6.8	9.73	9.16	0.18
	8	5.5	6.7	9.88	8.15	0.19
	9	5.5	6.7	9.48	7.32	0.17
	10	5.5	12.8	9.89	6.44	0.16
Grain 2						
	1	4.3	6.6	20.03	37.69	0.32
	2	4.3	6.7	18.6	27.61	0.24
	3	4.3	6.4	18.67	22.25	0.2
	4	4.3	6.7	20.34	20.71	0.19
	5	4.3	6.7	20.01	17.84	0.15
	6	4.3	6.8	20.13	15.7	0.19
	7	4.3	6.5	19.27	13.96	0.19
	8	4.3	12.6	18.12	12.39	0.15
Grain 3						
	1	4.3	6.8	17.36	25.26	0.22
	2	4.3	6.8	15.96	21.54	0.19
	3	4.3	8.8	14.32	17.71	0.18
	4	4.3	8.8	14.04	14.44	0.17
	5	4.3	9	14.17	11.84	0.17
	6	4.3	8.9	15.17	10.13	0.18
	7	4.3	9	13.92	8.62	0.15
	8	4.3	10.8	13.68	7.7	0.13
	9	4.3	10.8	13.33	6.73	0.15
Grain 4						
	1	5.5	6.1	12.03	36.94	0.41
	2	5.5	6.6	12.86	27.8	0.22
	3	5.5	6.6	12.57	22.92	0.24
	4	5.5	6.3	10.54	19.34	0.17
	5	5.5	8.7	12.14	16.36	0.18
	6	5.5	8.7	12.48	13.61	0.17
	7	5.5	10.9	11.93	11.3	0.16
	8	5.5	10.7	12.15	9.68	0.17

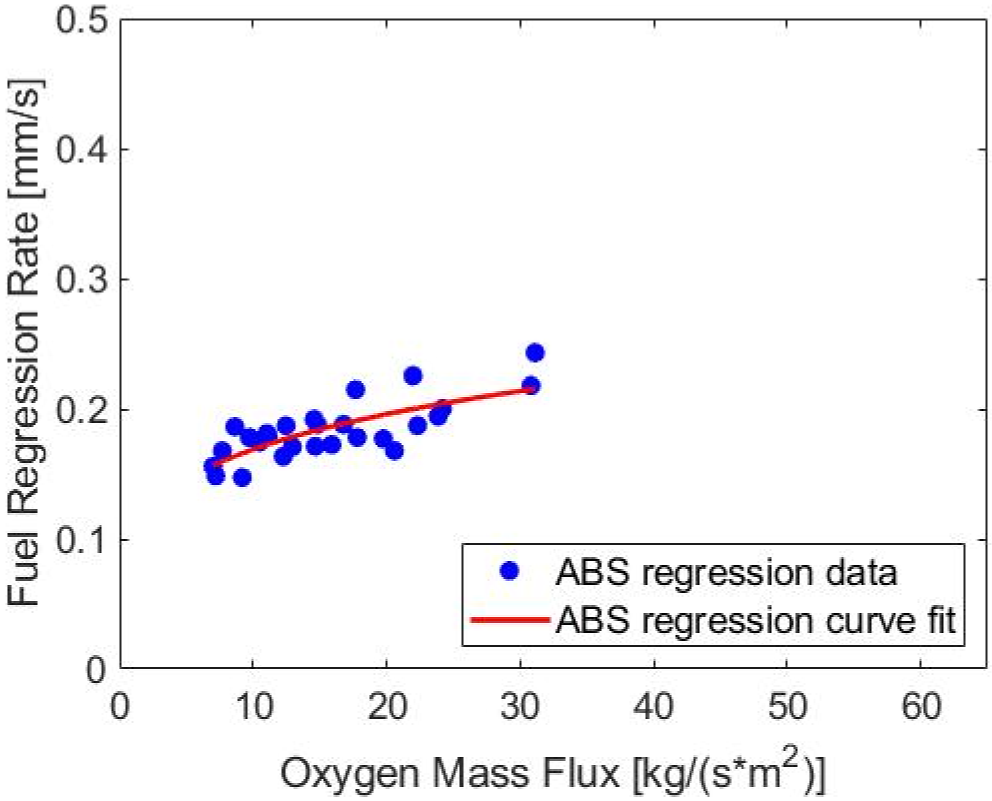

Figure 39 ABS regression curve.

The results for the baseline tests of the regression of pure paraffin can be seen below in Table 3, Fig. 40, and Fig. 41. Test series 1 and 2 were highlighted due to the difference in grain length, these tests were not included in the data for the regression fit, however they were compared to the rest of the data in Fig. 41.

Table 3 Baseline paraffin regression data.

Test series	Full grain length [mm]	Exhaust nozzle diameter [mm]	Average chamber pressure [bar]	Average Oxidizer mass Flux [kg/(s*m^2)]	Average regression rate [mm/s]
1	220	5.5	10.21	26.94	0.9
2	220	5.5	20.99	39.83	1.16
3	50	6.3	5.5	24.48	0.85
4	50	6.3	8.22	33.66	0.95
5	50.8	5.5	6.11	25.88	0.94
6	50.36	5.5	6.7	36.32	0.85
7	50.64	5.5	5.85	19.54	0.91
8	53.56	5.5	7.32	31.14	0.81
9	50	4.3	16.86	24.76	1.29
10	50.98	4.3	10.5	19.03	1.01
11	49.74	6.3	5.85	27.39	0.85
12	50.26	6.3	9.24	43.81	0.88
13	49.6	5.5	11.23	40.73	0.98
14	49.72	5.5	7.7	29.96	0.88
15	50.3	4.3	10.75	19.3	1
16	49.82	4.3	7.69	15.54	0.84
17	49.2	5.5	18.78	53.42	1.53
18	49.6	4.3	16.89	35.19	1.04
19	49.26	5.5	12.97	55.19	1.07

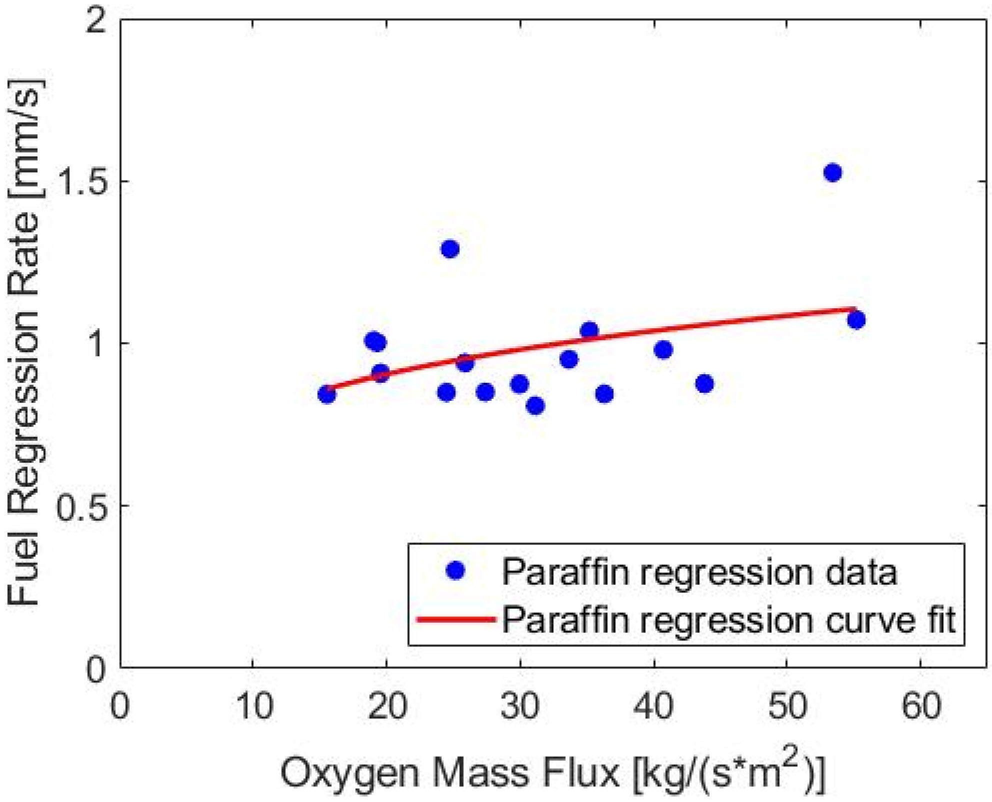

Figure 40 Baseline paraffin regression curve.

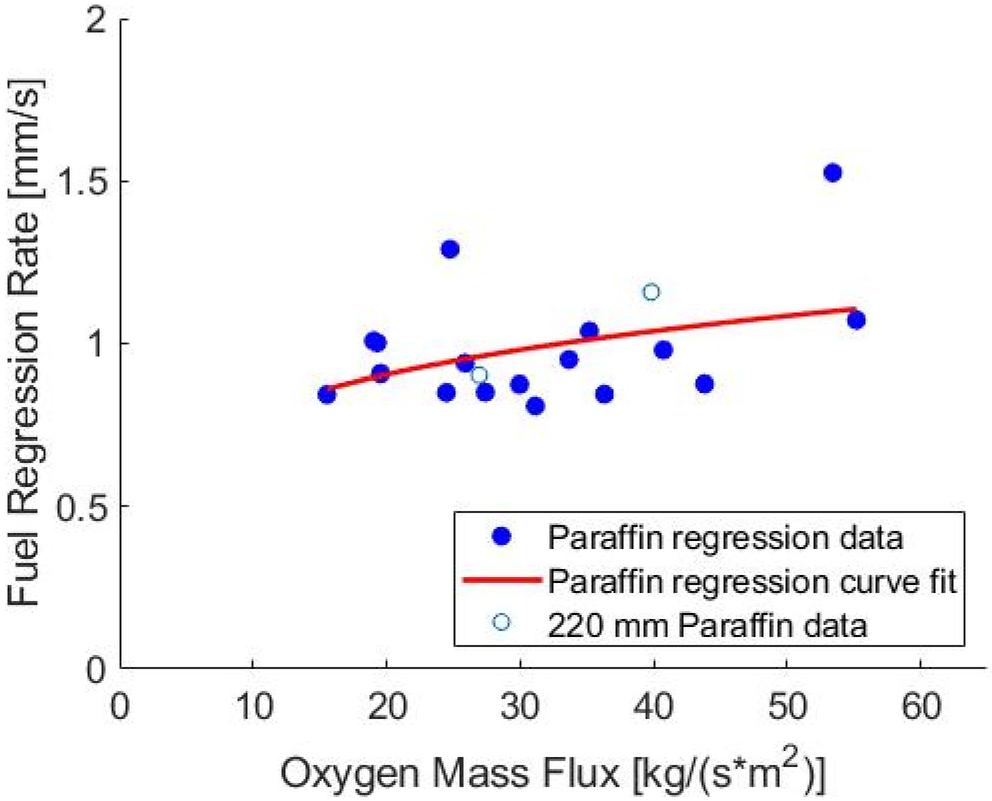

Figure 41 220 mm baseline grains compared to 50 mm grains.

The following equations characterize the regression fit curves shown in Fig. 39 and Fig. 40 respectively.

$$\dot{r}_{ABS}\left[\frac{mm}{s}\right] = 0.103 \cdot \left(G_{ox}\left[\frac{Kg}{m^2 \cdot s}\right]\right)^{0.215} \tag{12}$$

$$\dot{r}_{Paraffin}\left[\frac{mm}{s}\right] = 0.501 \cdot \left(G_{ox}\left[\frac{Kg}{m^2 \cdot s}\right]\right)^{0.198} \tag{13}$$

4.3 Regression of Paraffin in ABS structures.

The next stage was to test the regression of the paraffin within the printed ABS skeletons. An attempt was made to directly measure the separate regressions of the ABS structure as well as the paraffin fuel. The initial masses of the separate components were obtained by simply weighing the ABS skeleton prior to casting and then subtracting that mass from the total final casted mass of the grain in order to obtain the initial paraffin mass. The final separate masses were slightly more difficult to obtain, however the final process which was used was to forcibly submerge the grains in beakers filled with water which were placed on a temperature-controlled hotplate at a temperature of approximately 95^{o}C for a minimum of 4 hours in order to allow all of the paraffin to melt and float to the surface. The beakers were then removed from the hotplate and allowed to cool overnight. Once the paraffin had solidified, it was removed from the beaker and weighed. This mass was then subtracted from the total final mass of the grain in order to obtain a final ABS mass. The ABS skeletons could not be directly weighed reliably after this process due to the fact that ABS is mildly Hygroscopic and thus would likely have gained mass by absorbing the water while being submerged for 24 hours. A representative image of the paraffin separated from the ABS structure can be observed in Fig. 42. Unfortunately, as can be seen in Table 4, even excluding the measurement for test series 3 at 45 degrees to the flow, the results were too inconsistent, as well as in several cases suggesting that the ABS skeleton actually gained mass during the test. As such for all subsequent results, the ABS was assumed not to regress at all. Data for tests 5 and 6 of the 90^{o} grains was not included, as the original ABS mass was not recorded prior to casting so calculation of the initial paraffin mass was impossible.

Table 4 Measured separate mass delta.

135°	ABS start mass (measured) [g]	Total start mass (measured) [g]	Paraffin start mass (calculated from total mass and ABS start mass) [g]	Paraffin end mass (measured) [g]	Total end mass (measured) [g]	ABS end mass (calculated from total mass and paraffin end mass) [g]	ABS mass delta [g]	Paraffin mass delta [g]
Test 3	53.5	193.19	139.69	107.5	161.22	53.72	-0.22	32.19
Test 4	53.19	193.46	140.27	108.64	154.72	46.08	7.11	31.63
Test 5	53.53	194.12	140.59	110.56	162.94	52.38	1.15	30.03
Test 6	53.43	190.71	137.28	102.17	147.12	44.95	8.48	35.11
90°								
Test 3	54.89	202.21	147.32	113.72	172.5	58.78	-3.89	33.6
Test 4	54.69	195.48	140.79	98.02	162.03	64.01	-9.32	42.77
45°								
Test 3	53.6	194.31	140.71	135.95	172.87	36.92	16.68	4.76
Test 4	53.41	198.18	144.77	112.14	168.93	56.79	-3.38	32.63
Test 5	53.39	192.25	138.86	106.79	161.17	54.38	-0.99	32.07
Test 6	54.16	193.5	139.34	100.33	153.66	53.33	0.83	39.01

Figure 42 Paraffin removed from grain being weighed.

The final average radius of the paraffin was calculated slightly differently than for the baseline grains due to the ABS skeletons, which were assumed not to regress. The method of calculation for the radius of the grains with the skeletons was as follows. The 4*0.8 value in Eq. (4) is to account for the 4 walls that run the length of the grain and are 0.8 mm thick.

$$\Delta V = V_i - V_f = l_p \cdot (\pi \cdot (r_f^2 - r_i^2) - 4 \cdot 0.8 \cdot (r_f - r_i)) \tag{14}$$

$$\Delta m = \rho_p \cdot \Delta V = \rho_p \cdot l_p \cdot \left(\pi \cdot (r_f^2 - r_i^2) - 3.2 \cdot (r_f - r_i)\right) \tag{15}$$

$$r_f^2 - \frac{3.2}{\pi} \cdot r_f - \left(\frac{\Delta m}{\pi \cdot \rho_p \cdot l_p} - r_i^2 + \frac{3.2}{\pi} \cdot r_i\right) = a \cdot r_f^2 + b \cdot r_f + c = 0 \tag{16}$$

Eq. (16) can be solved through the use of the quadratic formula to obtain the final average radius of the grain.

The results for the 45^o grains can be seen in Table 5, Fig. 43 and Fig. 44. As with the baseline tests, the data for test series 1 and 2 were marked because of the difference in grain length from the rest of the data, this data was not used in the curve fit due to that fact. However, these points were compared to the rest of the data in Fig. 44. Test 13 was excluded because the C* efficiency was above 1 indicating an error somewhere in the measurement. Tests 3, 6, and 9 were excluded as they were clear outliers from the rest of the data.

Table 5 45^o regression data.

Test series	Full grain length [mm]	Exhaust nozzle diameter [mm]	Average chamber pressure [bar]	Average Oxidizer mass Flux [kg/(s*m^2)]	Average regression rate [mm/s]
1	220	5.5	18.69	23.1	1.16
2	220	5.5	27.02	35.12	1.42
3	50	6.3	6.33	24.43	0.87
4	50	6.3	9.7	31.99	1.14
5	49.72	5.5	7.2	21.39	1.18
6	49.74	5.5	11.32	27.49	1.45
7	50.32	5.5	8.3	20.71	1.07
8	50.2	5.5	9.18	26.01	1.1
9	50.18	4.3	18.99	22.12	1.51
10	50.18	4.3	12.46	17.71	1.18
11	50.36	6.3	13.5	28.3	1.03
12	50.34	6.3	11.7	36.37	1.22
13	50.2	5.5	13.08	35.34	1.29
14	50.26	5.5	8.73	26.45	1.06
15	50.32	4.3	12.28	18.91	1.04
16	50.14	4.3	9.88	14.41	0.94
17	50.2	5.5	20.28	59.5	1.32

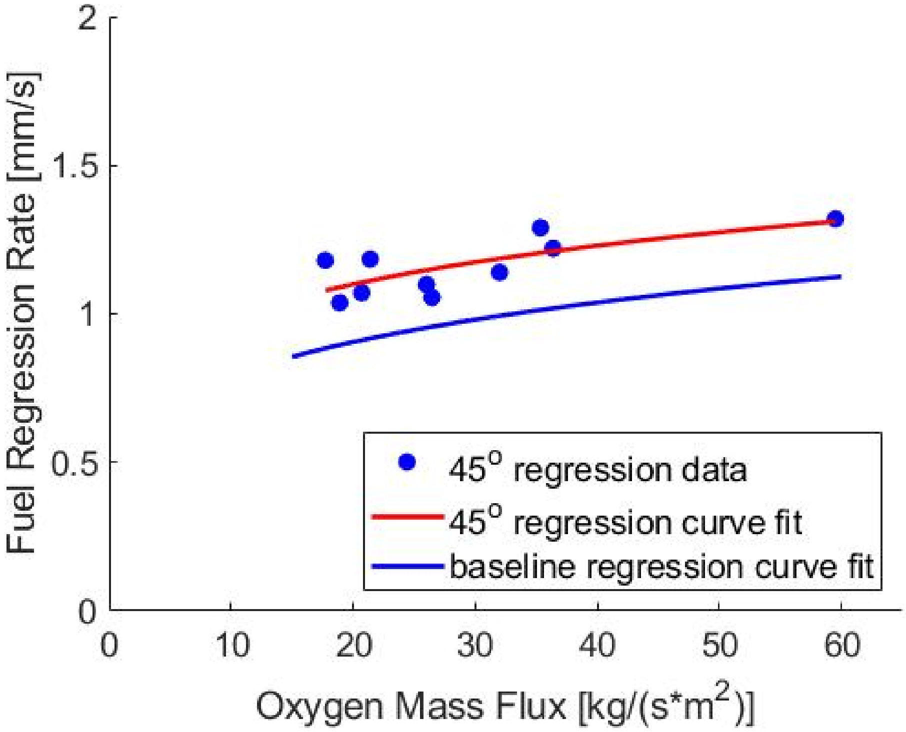

Figure 43 45° 50 mm skeleton regression rate fit.

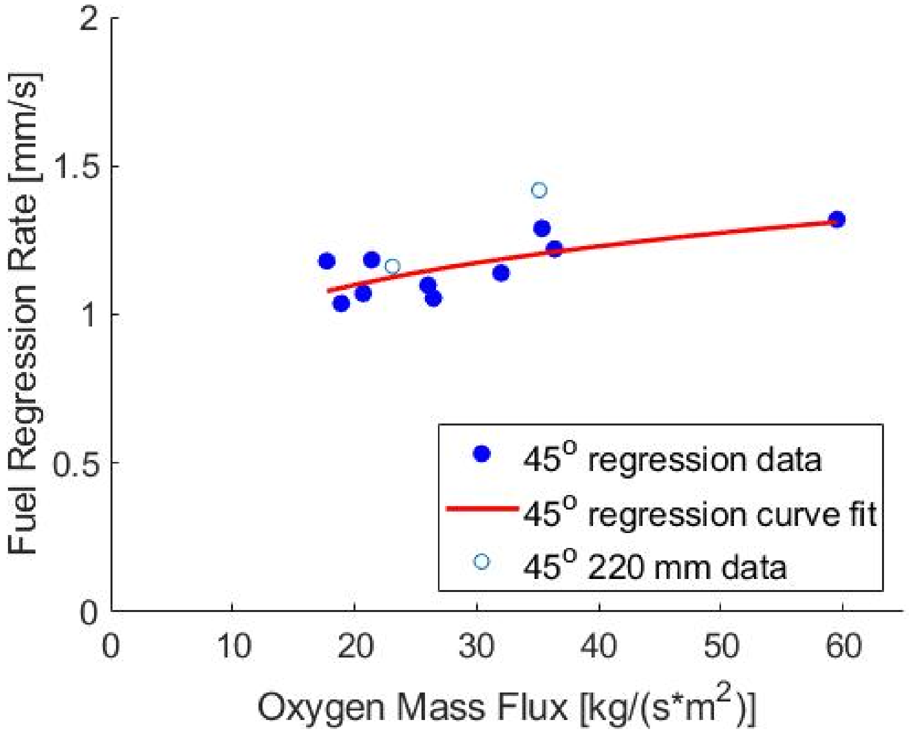

Figure 44 45^o comparison between 50 and 220 mm 45^o grains.

Results for the 90^o tests are reported in Table 6, Fig. 45, and Fig. 46. As with all other tests performed with paraffin, test series 1 and 2 were not included in the regression fit due to the difference in grain length, although again, these points are compared to the rest of the data in Fig. 46. Test series 9-11 were excluded due to being outliers from the rest of the data.

Table 6 90^{o} regression data.

Test series	Full grain length [mm]	Exhaust nozzle diameter [mm]	Average chamber pressure [bar]	Average Oxidizer mass Flux [kg/(s*m^2)]	Average regression rate [mm/s]
1	220	5.5	18.91	22.89	1.3
2	220	5.5	28.49	34.25	1.51
3	50	6.3	8.25	21.66	1.14
4	50	6.3	10.57	30.63	1.23
5	50.6	5.5	7.62	22.22	1.18
6	50.33	5.5	10.78	28.09	1.33
7	50.7	5.5	9.16	18.51	1.3
8	50.7	5.5	9.95	23.65	1.33
9	50.36	4.3	20.7	22.17	1.49
10	50.6	4.3	13.5	15.13	1.45
11	50.5	6.3	7.31	30.12	0.99
12	50.64	6.3	12.64	37.59	1.24
13	50.16	5.5	14.32	32.8	1.46
14	50.6	5.5	9.37	24.53	1.23
15	50.7	4.3	13.27	18.42	1.05
16	50.68	4.3	9.43	14.28	0.93
17	50.68	5.5	21.74	57.18	1.42
18	50.4	5.5	18.31	44.85	1.38

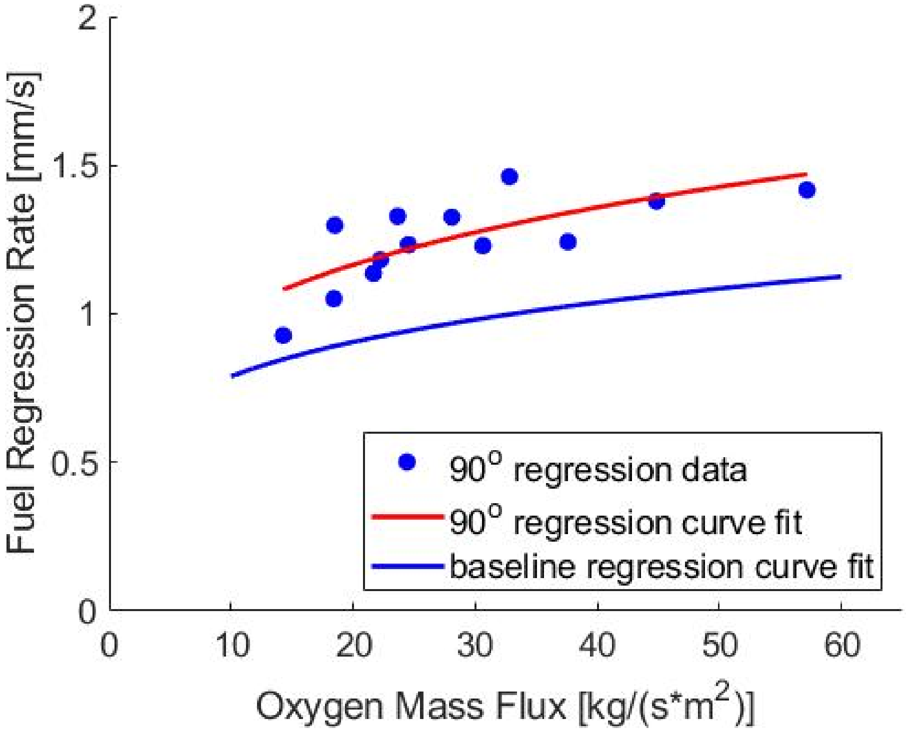

Figure 45 90º regression rate fit.

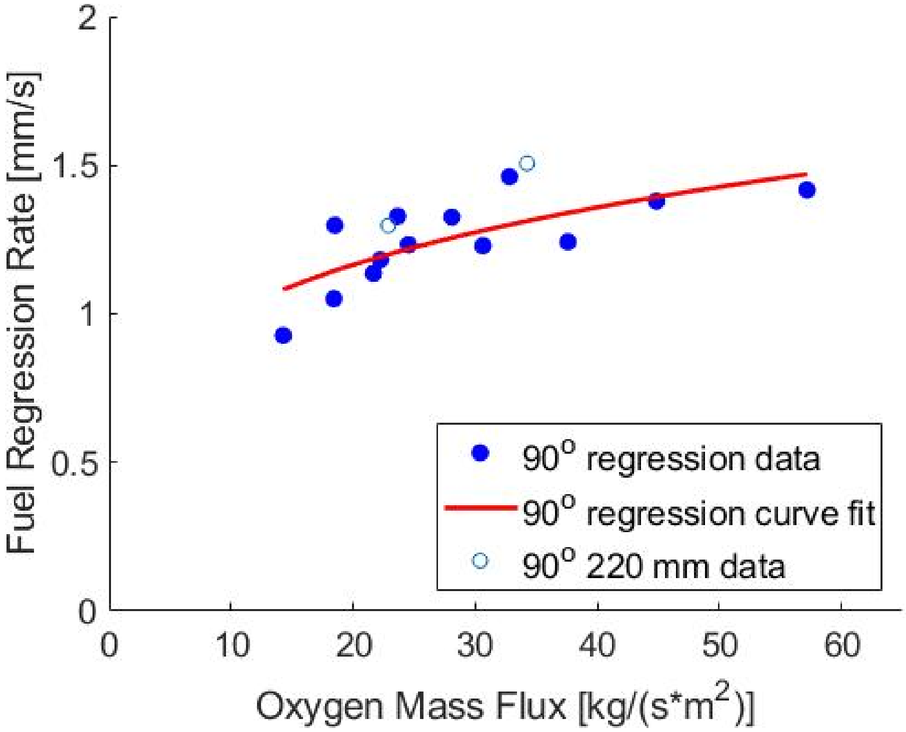

Figure 46 comparison between 50 and 220 mm 90º grains.

Results for all 135° tests are reported in Table 7, Fig. 47, and Fig. 48. Again, the results from test series 1 and 2 were not included in the curve fit due to the difference in length, however as with all other tests, they were compared to the rest of the results in Fig. 48. Tests 6 and 9 were excluded due to being outliers.

Table 7 135° regression data.

Test series	Full grain length [mm]	Exhaust nozzle diameter [mm]	Average chamber pressure [bar]	Average Oxidizer mass Flux [kg/(s*m^2)]	Average regression rate [mm/s]
1	220	5.5	18.7	23.46	1.21
2	220	5.5	28.25	31.27	1.69
3	50	6.3	8.97	20.87	1.19
4	50	6.3	11.66	29.07	1.4
5	50.04	5.5	8.54	22.52	1.2
6	49.55	5.5	12.58	26.31	1.54
7	50.06	5.5	8.68	17.83	1.03
8	50.62	5.5	12.52	23.71	1.33
9	50.1	4.3	21.06	22.5	1.48
10	50.1	4.3	13.62	17.23	1.24
11	50.18	6.3	9.81	23.92	1.15
12	50.26	6.3	14.1	35.98	1.33
13	50.16	5.5	16.54	33.76	1.42
14	50.2	5.5	12.52	24.53	1.3
15	50.4	4.3	14.32	18.92	1.1
16	50.18	4.3	10.07	13.88	1.05
17	50.06	5.5	23.67	50.04	1.54
18	49.9	5.5	21.51	43.36	1.45

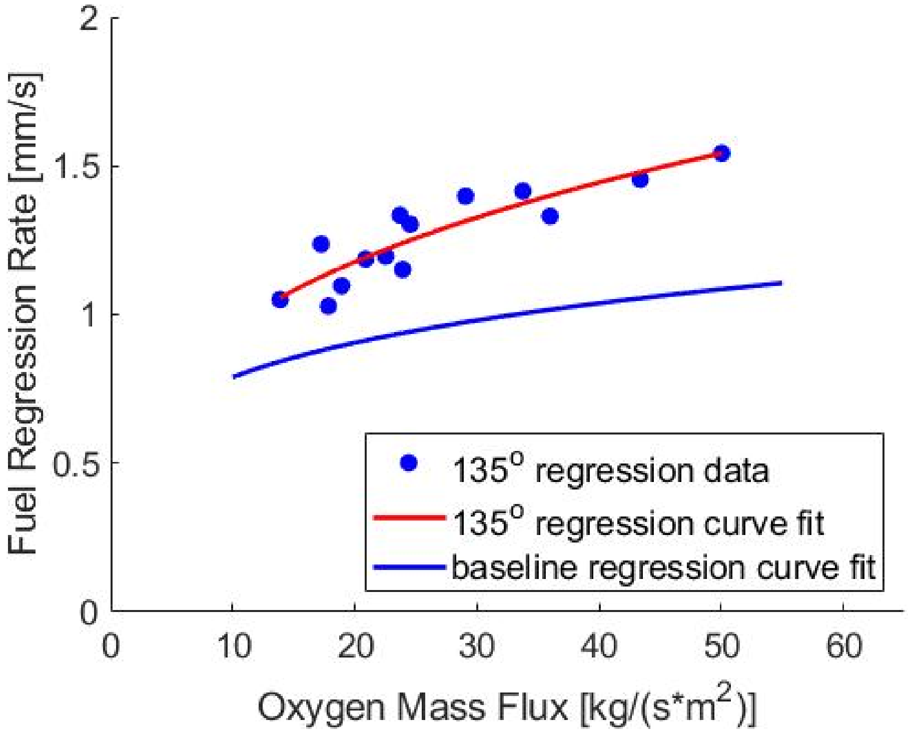

Figure 47 135^o regression rate fit.

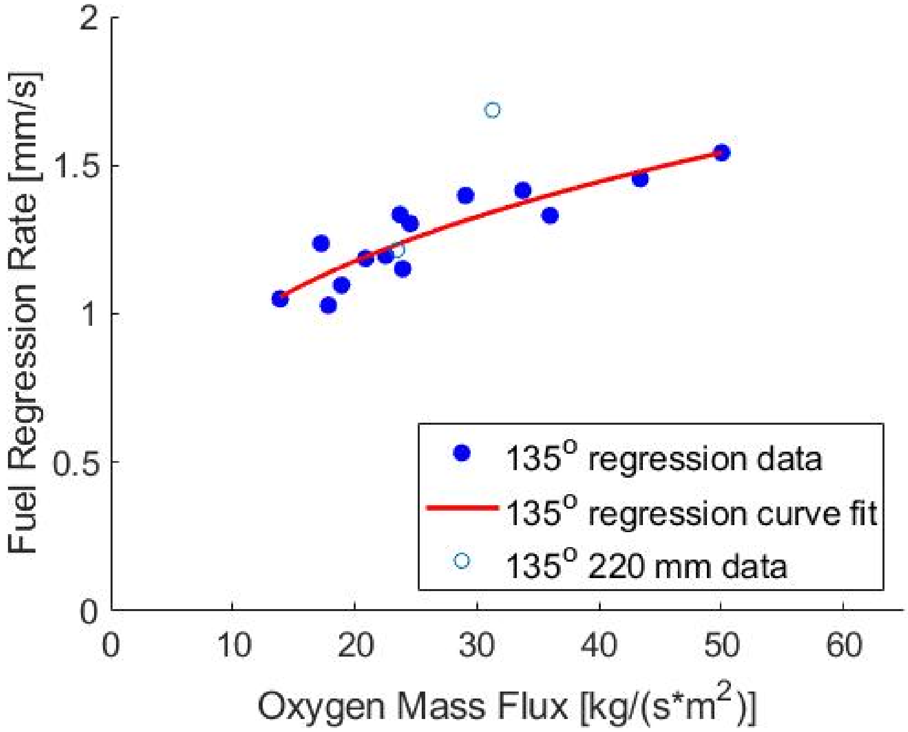

Figure 48 Comparison between 50 and 220 mm 135^o grains.

For ease of direct comparison between all regression rates, the respective regression curves are all presented in Fig. 49. It is suspected that at least one factor that led to the increased regression rate is a similar mechanism to the mechanism observed by Gany and Manheimer-Timnat (1972). (Gany and Manheimer-Timnat 1972).

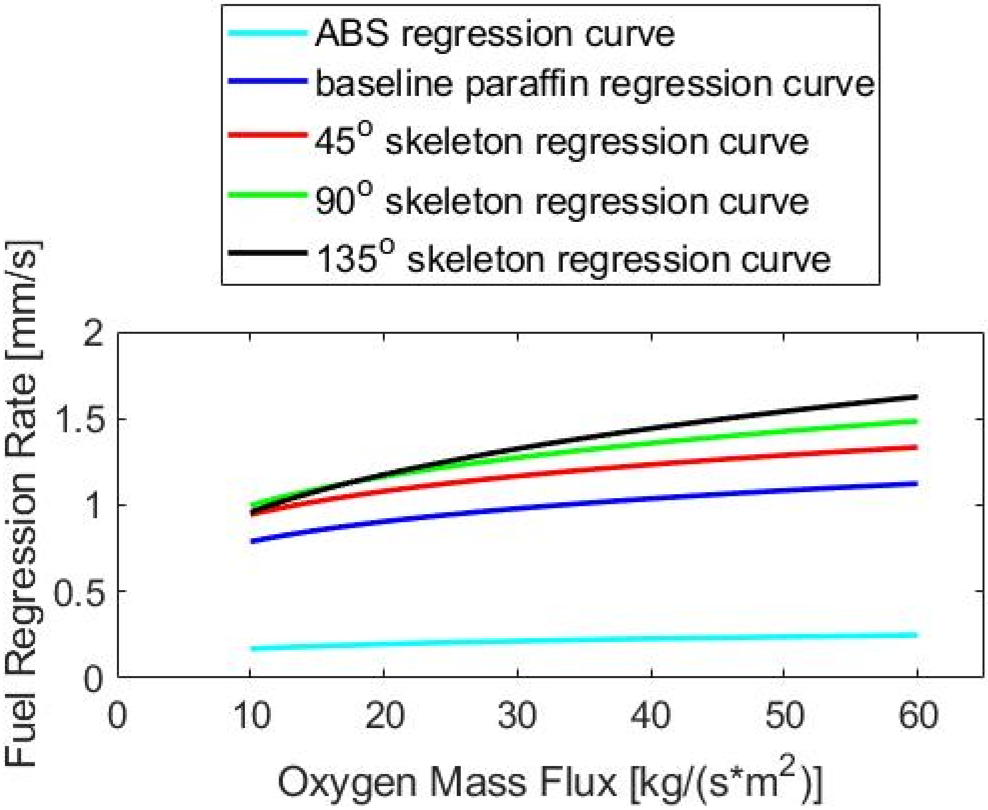

Figure 49 Comparison between regression rate curves for all grains.

As can be observed, the 135° angle caused the highest increase in regression rate, followed by the 90° angle and finally the 45° angle. Additionally, the power of the regression rate curve increased significantly with the angle of the skeleton, as shown in Eqs. (17-19). Angles are defined as the angle between the flow vector and the half angle of the cone in the skeleton, in the 45° case, the 45° skeleton was placed with the tip of the cone pointing towards the exhaust, whereas in the 135° case, the tip of the cone would be pointing towards the oxygen injection.

$$\dot{r}_{45\ degrees}\left[\frac{mm}{s}\right] = 0.678 \cdot \left(G_{ox}\left[\frac{kg}{m^2 \cdot s}\right]\right)^{0.162} \tag{17}$$

$$\dot{r}_{90\ degrees}\left[\frac{mm}{s}\right] = 0.6 \cdot \left(G_{ox}\left[\frac{kg}{m^2 \cdot s}\right]\right)^{0.222} \tag{18}$$

$$\dot{r}_{135\ degrees}\left[\frac{mm}{s}\right] = 0.486 \cdot \left(G_{ox}\left[\frac{kg}{m^2 \cdot s}\right]\right)^{0.295} \tag{19}$$

It should be noted that the exponents found in this research are generally significantly lower than other paraffin-based systems, including previous tests performed on the test stand used in this research. Such as the research presented in Kormornik (2014) where for the same range of oxidizer mass fluxes, the baseline regression of paraffin was found to be characterized by the power curve shown in Eq. (20) (Komornik 2014). This difference is suspected to be related to an erroneous behavior that occurs in the test stand used for this research. Due to the fact that the endplates which are in direct contact with the ends of the paraffin grains are not actively cooled, they become very hot during repeated firings. This leads to a decrease in the length of the paraffin within the casing as it melts away from the walls. In this research that length change was found to be as high as 10 mm in some cases. For the length of grains that were tested in Kormornik (2014) that did not compose a significant part of the initial length, since the grains tested in that research were 190 and 380 mm in length; therefore a 10 mm change would cause a ratio of final length to original length of 0.947 or 0.974 respectively. However, in the present research this ratio would be 0.8. The equations that were used to calculate the final radii of the grains do not take into account a change in length of the grain during the firing and assume that all mass loss from the grain was caused by the heat transferred from the flow and not from the case. The theory that the decreased exponent and increased multiplier were caused by the length of the tested grains is further supported by the results from Kormornik and Gany (2018). The regression curves from Kormornik (2014) and Kormornik and Gany (2018) for a 90 mm grain length (performed at the same test stand as the present research) can be seen in Eqs. (20) and (21) respectively. An attempt was made to find a method of accounting for the regression from the end walls, however it was unsuccessful.

$$\dot{r}_{190mm-330mm}\left[\frac{mm}{s}\right] = 0.15\left(G_{ox}\left[\frac{kg}{m^2 \cdot s}\right]\right)^{0.6} \tag{20}$$

$$\dot{r}_{90mm}\left[\frac{mm}{s}\right] = 0.35\left(G_{ox}\left[\frac{kg}{mm \cdot s}\right]\right)^{0.3} \tag{21}$$

From Figs. 46, 48, and 50, it would appear that there may be a correlation between the length of the sections between the baffles and the regression of the paraffin. The distance between the baffles on the 50 mm grains was 15.6 mm, whereas the distance between the baffles on the 220 mm grains was 25.6 mm. This theory is further supported by a cross section that was taken of one of the grains originally provided by Rafael which had a slightly different design to the ones reported here, and which can be seen in Fig. 50. This grain was originally cut in half in an attempt to use a 3D scan of the regressed surface to directly measure the regression as a function of length of the grain, however the 3D scan was not of a high enough resolution to be used.

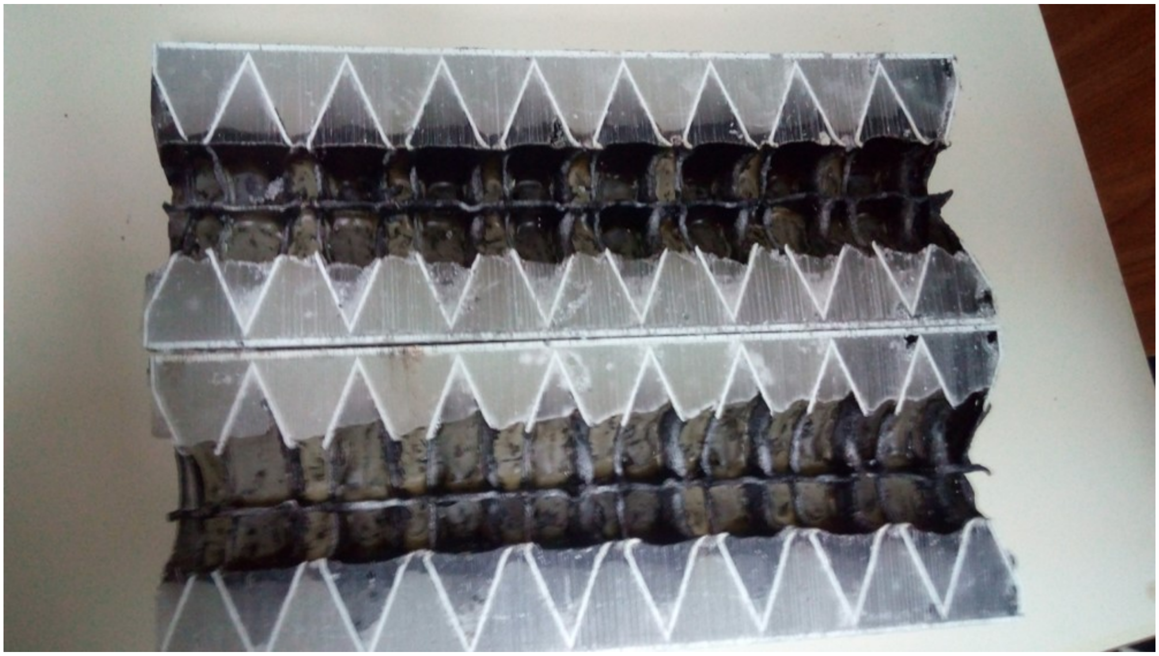

Figure 50 Cross sectioned Rafael Grain.

One behavior that was observed in the paraffin baseline tests as well as a behavior that has been observed during previous work performed on the test stand here is that a significant portion of paraffin that is ejected from the fuel grain does not exit the mixing chamber. (Weinstein and Gany 2011) As this mass does not exit the control volume, it does not provide any thrust and thus cannot be considered when calculating the performance of the system. The un-ejected mass as a fraction of total mass ejected from the grain can be seen in Figs. 53-57 as well as Table 8. Test series 11 for the 45^o grains was excluded as both measured C* efficiencies exceeded 1. The curve fits are for illustrative purposes only; however, they do show a clear trend in that the paraffin grains without any added structure failed to eject a significant amount of mass from the mixing chamber whereas the 45^o, 90^o, and 135^o cones each provided successively better mixing quality between the paraffin and the oxygen resulting in better combustion efficiency. An additional method by which the skeletons may have limited the paraffin remaining in the mixing chamber was that the baffles along the length of the grain may have caught some of the paraffin flowing along the bottom of the grain, which was modeled by Weinstein and Gany (Weinstein and Gany 2011). This would also account for the 135^o baffles being the most efficient, while the 45^o baffles were the least efficient in preventing liquid paraffin melt layer flow since the 135^o baffles would be more likely to trap liquid paraffin while the 45^o baffles would be more likely to allow it to continue flowing.

Table 8 Mixing chamber mass fractions.

Series	Average oxidizer mass flow [g/s]	Baseline Paraffin	135°	90°	45°
5	16.33	0.489	0.12	0.22	0.212
6	22.15	0.527	0.105	0.126	0.262
7	13.48	0.371	0.049	0.126	0.163
8	18.68	0.522	0.05	0.242	0.41
9	18.39	0.371	0.045	0.203	0.232
10	12.67	0.406	0.302	0.108	0.269
11	18.4	0.408	0.082	0.101	0.178
12	27.58	0.278	0.067	0.169	0.109
13	26.86	0.37	0.108	0.112	0.245
14	18.8	0.534	0.102	0.127	0.236
15	13.22	0.43	0.22	0.133	0.289
16	9.71	0.336	0.258	0.264	0.161
17	44.26	0.405	0.085	0.191	0.26
18	32.21	0.417			
19	38.14	0.281	0.112	0.136	

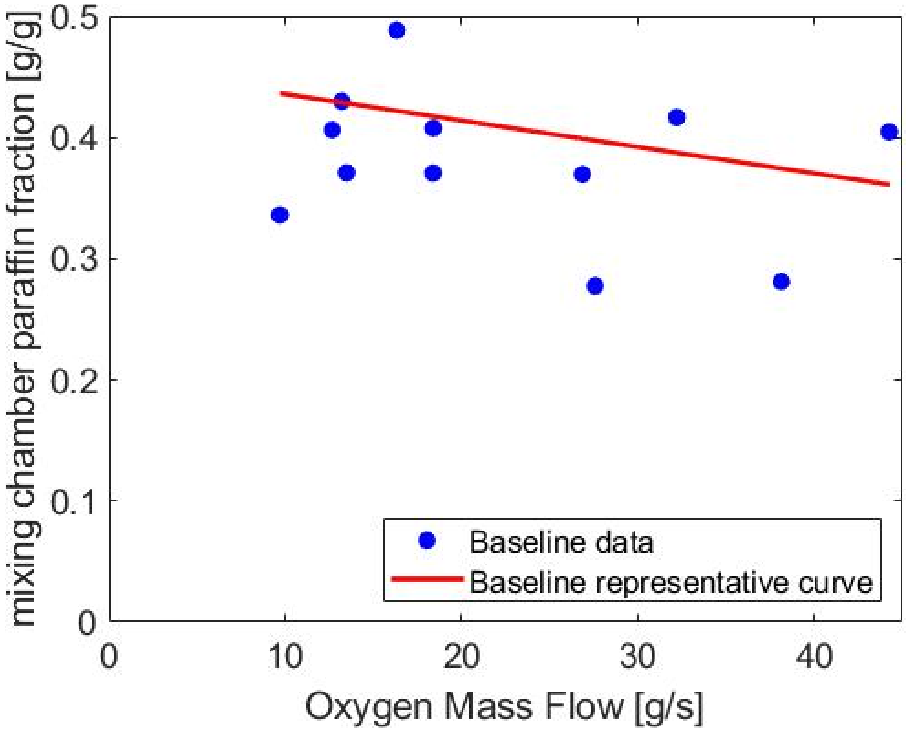

Figure 51 Baseline paraffin mixing chamber fraction.

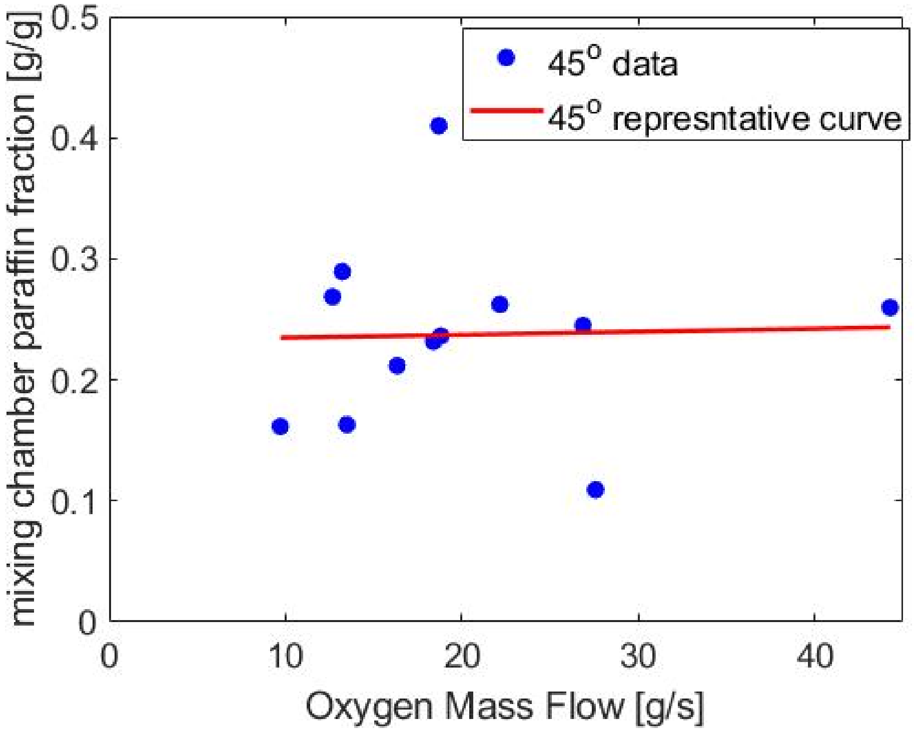

Figure 52 45° mixing chamber paraffin fraction.

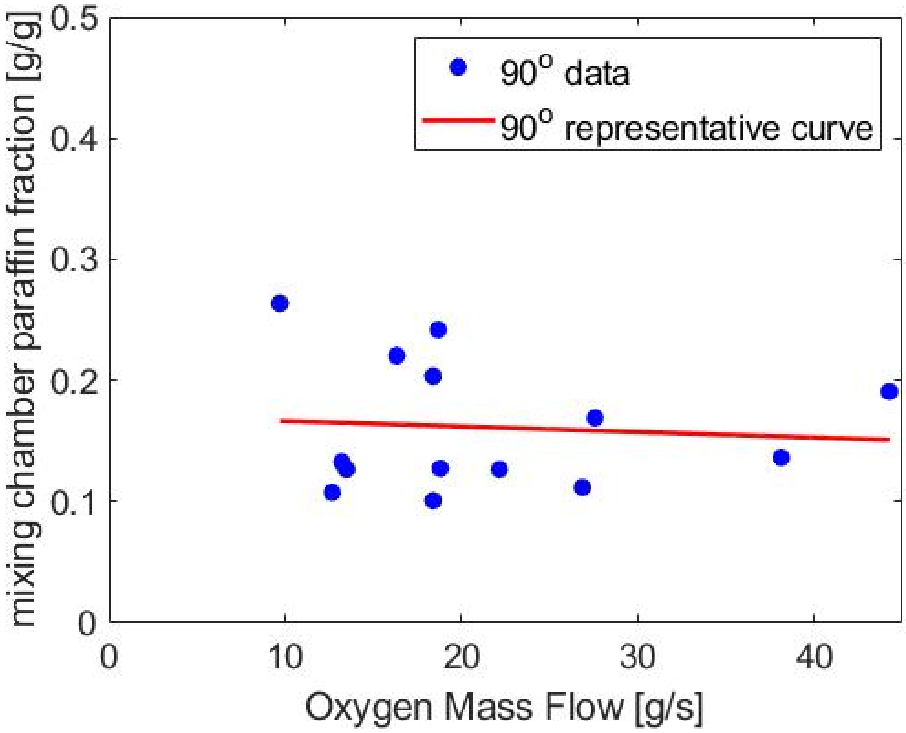

Figure 53 90º mixing chamber paraffin fraction.

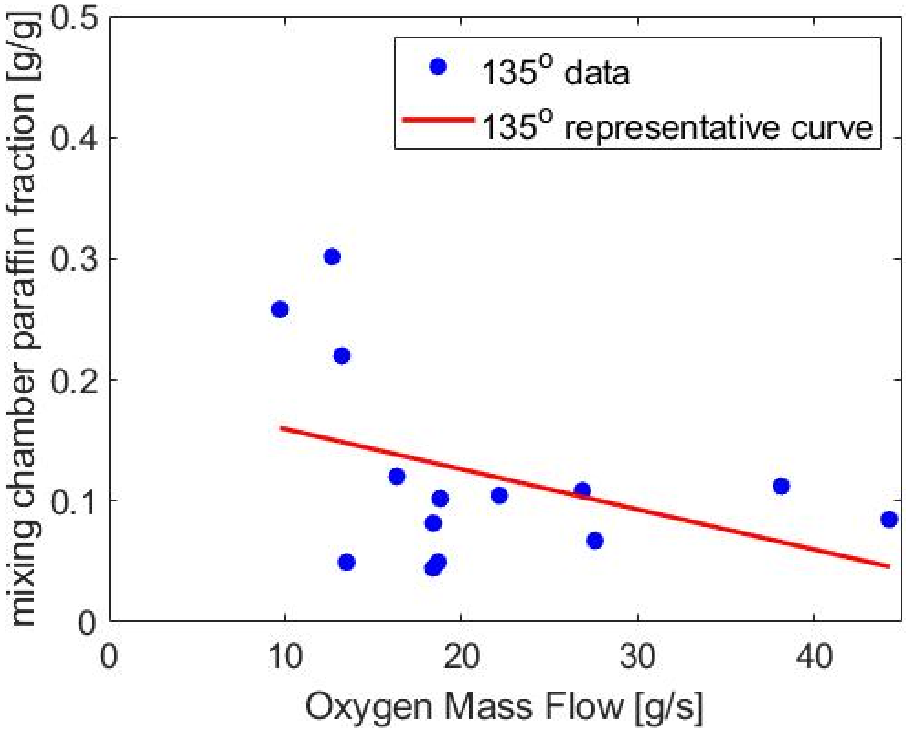

Figure 54 135º mixing chamber paraffin fraction.

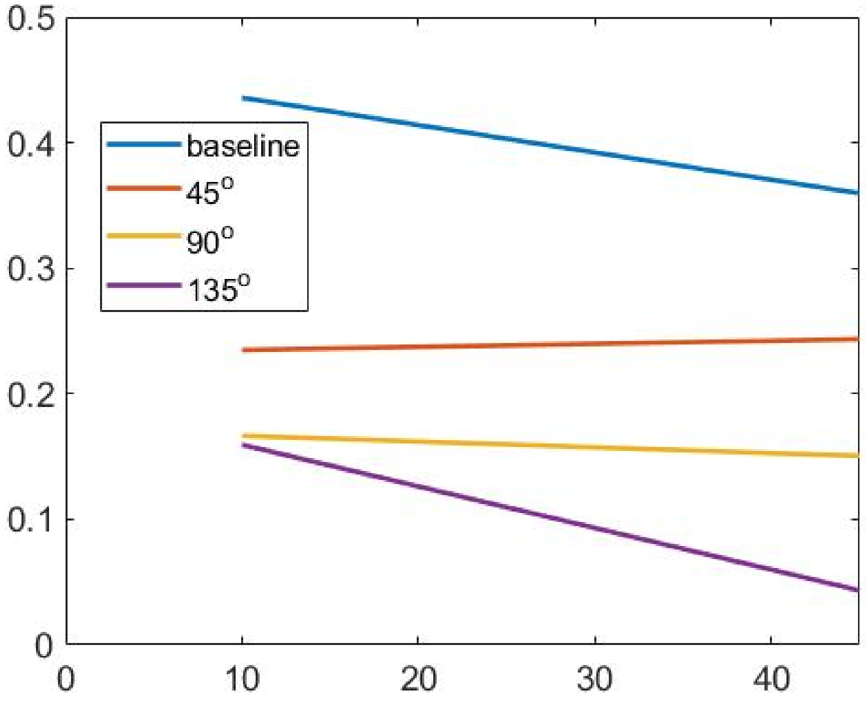

Figure 55 Comparison of mixing efficiency representative curves.

One of the most important performance factors in the design of rocket propulsion systems is the C* or characteristic velocity, and more specifically the C* efficiency when compared to theoretical values. For this research, the theoretical C* of the paraffin-based systems was obtained through the use of NASA CEA in the Rocket Problem setting. The combustion chamber was assumed to be of infinite area, which would cause zero flow velocity in the combustion chamber, additionally the flow composition was assumed to freeze in the combustor. Since paraffin was not available as a built-in fuel, $CH_2\ (cr)$ was used instead as it should have similar performance to paraffin. The C* value from the experiments was obtained by using Eq. (22).

$$C^* = \frac{P_c \cdot A_t}{\dot{m}_{ox} + \dot{m}_{fuel}} \tag{22}$$

Two sets of figures and tables will be used to present the C* efficiency of the tests, the first of the sets of figures, Figs.(56-61) as well as Tables (9-12) assume that all mass that left the grain left the engine, this assumption was also used when inputting the ϕ value into CEA, which means that it assumes that this fuel was burned when in fact it was not. The trend lines are for illustrative purposes only, but clearly show that all three skeleton angles provided an improved C* efficiency when compared to the baseline paraffin grains. Test series 11 for the 45° grains was excluded from Figs. (57-61) as it exceeded an efficiency of 1 as can be seen in Fig. 56.

Table 9 Baseline C* data assuming that all mass that left the grains left the nozzle.

series	oxygen mass flow rate [g/s]	ϕ	paraffin test C* [m/s]	paraffin theoretical C* [m/s]	paraffin C* efficiency
1	17.62	3.17	717	1397.8	0.513
2	29.18	2.597	974.4	1570.1	0.621
3	15.72	0.753	894.2	1554.8	0.575
4	22.5	0.6	969.9	1501.6	0.646
5	16.62	0.8	708.6	1573.9	0.45
6	22.31	0.52	619.9	1458.3	0.425
7	12.54	1.021	854.2	1640.9	0.521
8	18.75	0.624	785.3	1509.5	0.52
9	18.65	1.043	1007.7	1675.4	0.601
10	12.71	1.149	900.3	1688.8	0.533
11	16.94	0.683	898.6	1529.3	0.588
12	27.54	0.441	927.7	1419.2	0.654
13	27.03	0.509	859.9	1462.7	0.588
14	19.03	0.633	812.6	1514.9	0.536
15	13.26	1.095	893.7	1676.5	0.533
16	9.82	1.183	846.7	1688.1	0.502
17	44.63	0.534	865.6	1486.2	0.582
18	23.96	0.616	868.3	1524.6	0.57
17	38.14	0.4	724.1	1397.5	0.518

Table 10 135° C* data assuming that all mass that left the grain left the nozzle.

series	Oxygen mass flow rate [g/s]	ϕ	135° test C* [m/s]	135° theoretical C* [m/s]	135° C* efficiency
1	17.62	4.258	1128	1289	0.875
2	29	4.002	1071	1317	0.813
3	15.72	1.03	1369	1655	0.827
4	23.77	0.838	1230	1603	0.767
5	16.36	0.98	965	1640	0.589
6	22.2	0.995	1045	1654	0.632
7	12.48	1.084	1257	1668	0.754
8	18.76	1.009	1226	1658	0.739
9	18.3	1.15	1253	1708	0.733
10	12.66	1.32	1129	1731	0.653
11	17.24	0.894	1408	1617	0.871
12	27.82	0.666	1324	1542	0.858
13	27.22	0.738	1189	1575	0.755
14	18.92	0.956	1231	1643	0.749
15	13.37	1.092	1181	1684	0.702
16	9.74	1.425	1063	1738	0.611
17	41.7	0.533	1168	1490	0.784
18					
17	36.42	0.576	1202	1510.3	0.796

Table 11 90° C* data assuming that all mass that left the grain left the nozzle.

series	oxygen mass flow rate [g/s]	ϕ	90° test C* [m/s]	90° theoretical C* [m/s]	90° C* efficiency
1	17.6	4.607	1093	1266	0.862
2	29.29	3.397	1164	1377	0.845
3	15.84	0.964	1268	1634	0.776
4	23.51	0.721	1159	1558	0.744
5	16.4	0.986	858	1638	0.524
6	21.86	0.848	940.3	1605	0.586
7	14.35	1.272	1107	1711	0.647
8	18.6	1.012	983	1653	0.595
9	18.48	1.166	1215	1711	0.71
10	12.58	1.68	1048	1761	0.595
11	20.18	0.634	954	1514	0.63
12	27.77	0.613	1204	1517	0.794
13	26.4	0.785	1050	1590	0.66
14	18.59	0.92	945	1624	0.582
15	13.01	1.083	1127	1679	0.671
16	9.59	1.262	1045	1710	0.611
17	45.55	0.444	1005	1435	0.7
18					
17	36.25	0.543	1036	1490	0.695

Table 12 45^o C* data assuming that all mass that left the grain left the nozzle.

series	oxygen mass flow rate [g/s]	ϕ	45^o test C* [m/s]	45^o theoretical C* [m/s]	45^o C* efficiency
1	16.87	4.192	1187	1294.4	0.917
2	29.21	3.16	1146	1407.1	0.815
3	15.85	0.695	1035	1536.1	0.674
4	23.25	0.657	1092	1530.1	0.714
5	15.93	1.003	831	1641.4	0.506
6	22.25	0.921	954	1629.3	0.585
7	14.55	0.976	1056	1637.5	0.645
8	18.63	0.788	953	1579.8	0.603
9	18.13	1.191	1130	1714.6	0.659
10	12.73	1.24	1045	1713.3	0.61
11	19.22	0.699	1821	1555.4	1.171
12	27.2	0.615	1137	1515.9	0.75
13	26.8	0.662	973	1539.2	0.632
14	18.66	0.75	912	1564.8	0.583
15	13.23	1.037	1035	1665.2	0.622
16	9.69	1.246	1087	1708.1	0.637
17	45.18	0.402	955	1405.6	0.679

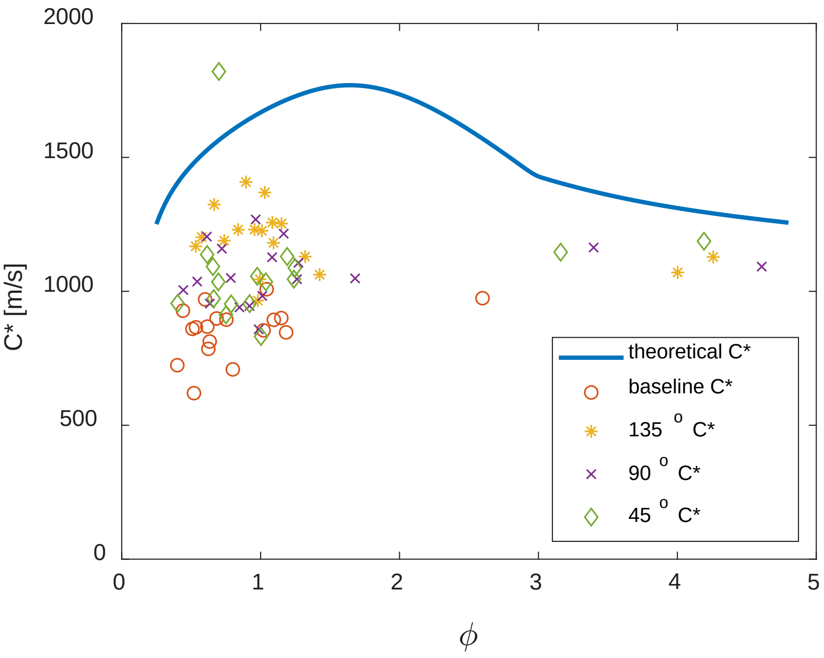

Figure 56 C* comparison for mass ejected from grain.

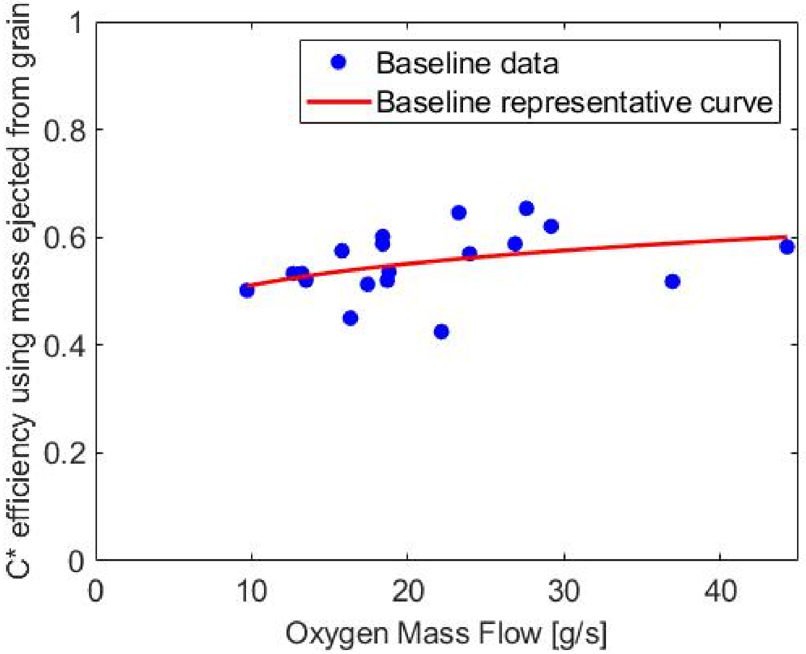

Figure 57 C* efficiency for baseline paraffin grains using mass ejected from grains.

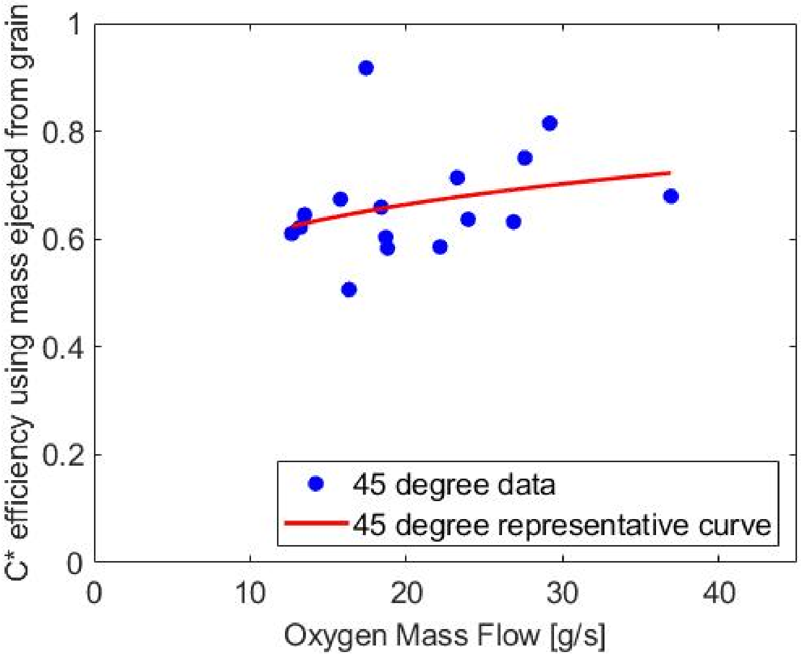

Figure 58 C* efficiency for 45^o grains using mass ejected from grains.

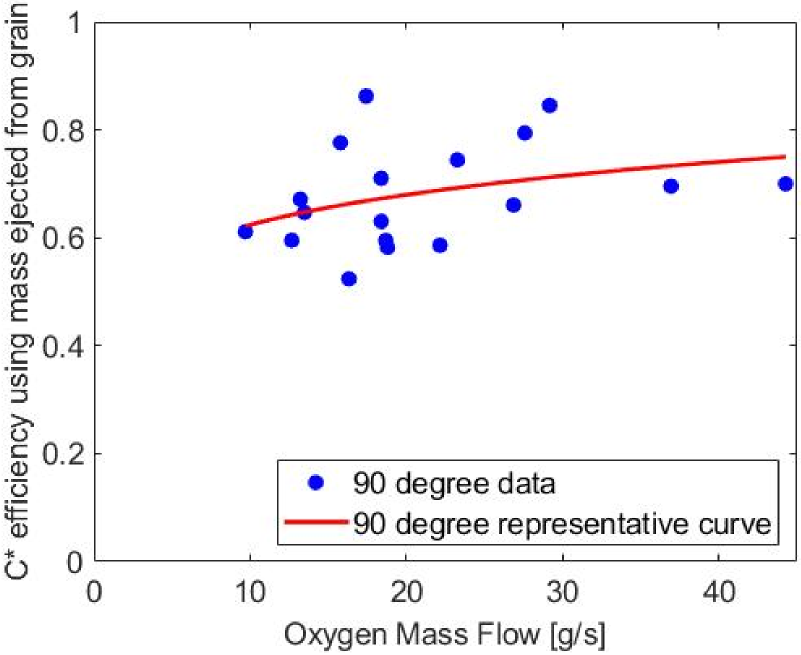

Figure 59 C* efficiency for 90o grains using mass ejected from grains.

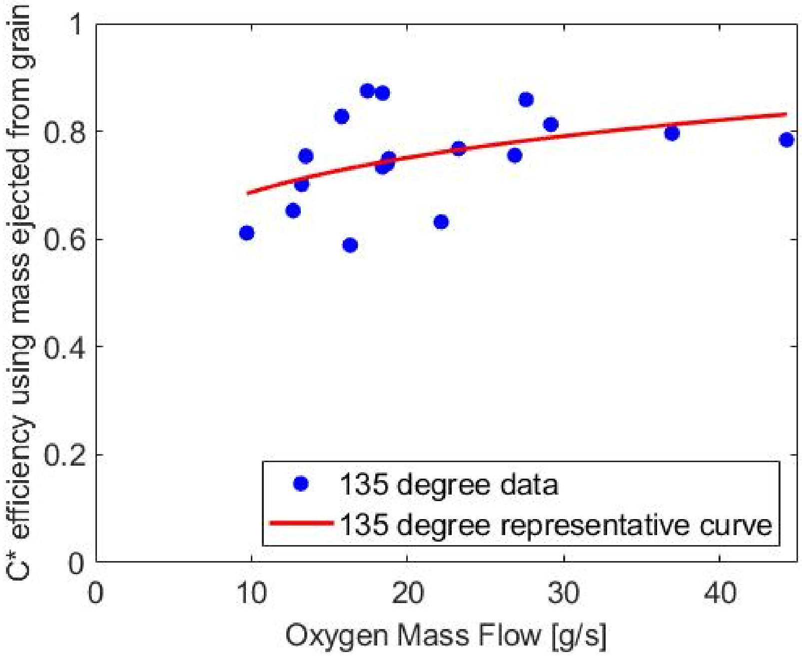

Figure 60 C* efficiency for 135º grains using mass ejected from grains.

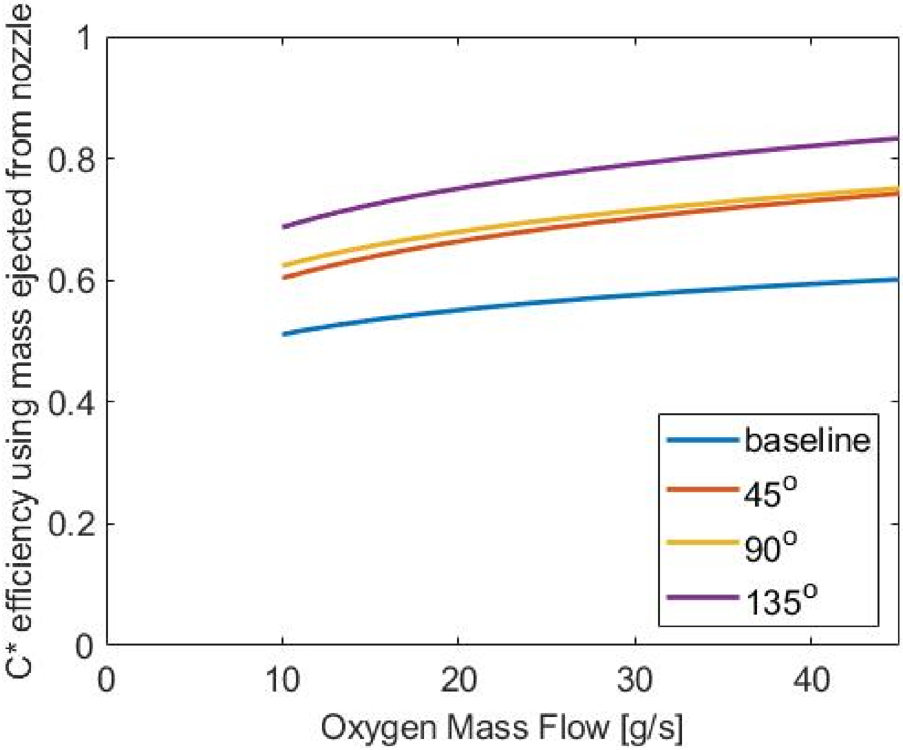

Figure 61 Comparison of C* efficiencies using mass ejected from grains.

Figs. (62-67) as well as Tables (13-16), on the other hand account for the unburned and un-ejected mass when calculating the C* efficiency, this includes in its implementation of Eq. (14), as well as the ϕ value input into NASA CEA in order to obtain the theoretical value. Again, the trend lines are only for easier visualization of the improved performance granted by the ABS skeletons. Series 1-4 were not included since the paraffin remaining the mixing chamber was not weighed for those tests, again the 45^o skeleton test 11 data was excluded from Figs. (63-67) due to an efficiency exceeding 1 which can be seen in Fig. 62.

Table 13 Baseline C* data accounting for unburned paraffin in mixing chamber.

series	Oxygen mass flow rate [g/s]	ϕ	paraffin test C* [m/s]	paraffin theoretical C* [m/s]	paraffin C* efficiency
5	16.62	0.409	780	1574	0.496
6	22.31	0.246	666	1458	0.457
7	12.54	0.642	933	1641	0.569
8	18.75	0.298	853	1509	0.565
9	18.65	0.657	1103	1675	0.658
10	12.71	0.682	1002	1689	0.593
11	16.94	0.404	964	1529	0.63
12	27.54	0.318	958	1419	0.675
13	27.03	0.321	903	1463	0.617
14	19.03	0.295	886	1515	0.585
15	13.26	0.624	997	1676	0.595
16	9.82	0.786	926	1688	0.549
17	44.63	0.318	915	1486	0.616
18	23.96	0.359	927	1525	0.608
17	38.14	0.288	746	1397	0.534

Table 14 135° C* data accounting for unburned paraffin in mixing chamber.

series	Oxygen mass flow rate [g/s]	ϕ	135° test C* [m/s]	135° theoretical C* [m/s]	135° C* efficiency
5	16.36	0.862	992	1603	0.619
6	22.2	0.891	1070	1623	0.659
7	12.48	1.031	1272	1654	0.769
8	18.76	0.959	1240	1643	0.754
9	18.3	1.099	1267	1696	0.747
10	12.66	0.922	1233	1634	0.754
11	17.24	0.821	1432	1593	0.899
12	27.82	0.621	1339	1523	0.879
13	27.22	0.658	1212	1543	0.786
14	18.92	0.859	1259	1612	0.781
15	13.37	0.852	1247	1613	0.773
16	9.74	1.057	1149	1665	0.69
17	41.7	0.488	1181	1464	0.807
18					
17	36.42	0.511	1222	1476	0.828

Table 15 90° C* data accounting for unburned paraffin in mixing chamber.

series	oxygen mass flow rate [g/s]	ϕ	90° test C* [m/s]	90° theoretical C* [m/s]	90° C* efficiency
5	16.4	0.769	902	1568	0.575
6	21.86	0.741	964	1566	0.616
7	14.35	1.111	1145	1676	0.684
8	18.6	0.767	1040	1574	0.661
9	18.48	0.929	1281	1647	0.778
10	12.58	1.499	1087	1754	0.62
11	20.18	0.57	969	1485	0.653
12	27.77	0.509	1236	1465	0.843
13	26.4	0.697	1072	1556	0.689
14	18.59	0.803	971	1586	0.613
15	13.01	0.939	1164	1639	0.71
16	9.59	0.929	1125	1627	0.691
17	45.55	0.359	1027	1372	0.748
18					
17	36.25	0.469	1056	1449	0.729

Table 16 C* data accounting for unburned paraffin in mixing chamber.

series	oxygen mass flow rate [g/s]	ϕ	45° test C* [m/s]	45° theoretical C* [m/s]	45° C* efficiency
5	15.93	0.791	873	1575	0.554
6	22.25	0.679	1010	1543	0.654
7	14.55	0.817	1096	1587	0.69
8	18.63	0.465	1032	1434	0.72
9	18.13	0.915	1201	1641	0.732
10	12.73	0.907	1125	1627	0.692
11	19.22	0.575	1877	1500	1.251
12	27.2	0.548	1157	1484	0.78
13	26.8	0.5	1013	1460	0.693
14	18.66	0.573	952	1490	0.639
15	13.23	0.737	1110	1568	0.708
16	9.69	1.045	1136	1661	0.684
17	45.18	0.298	981	1312	0.748

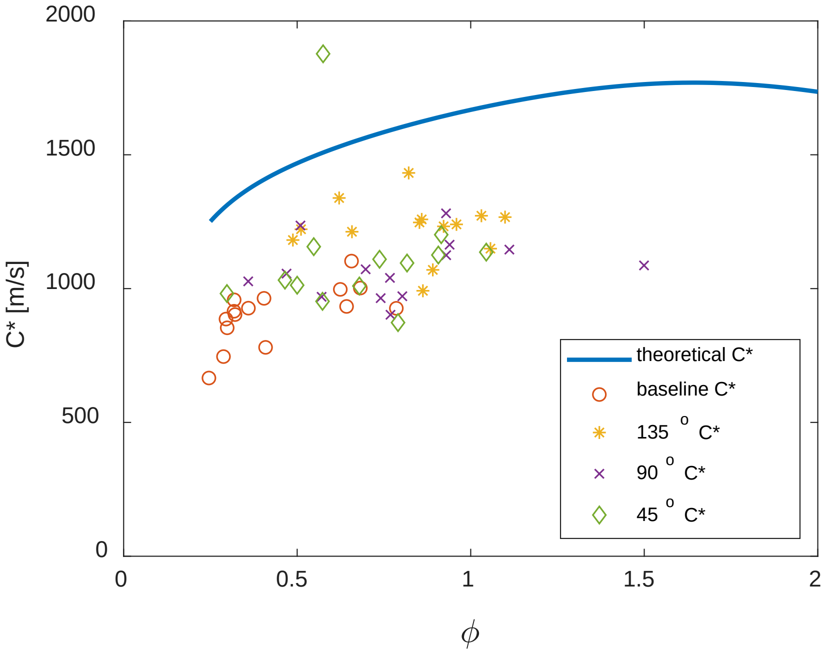

Figure 62 C* comparison for mass ejected from nozzle.

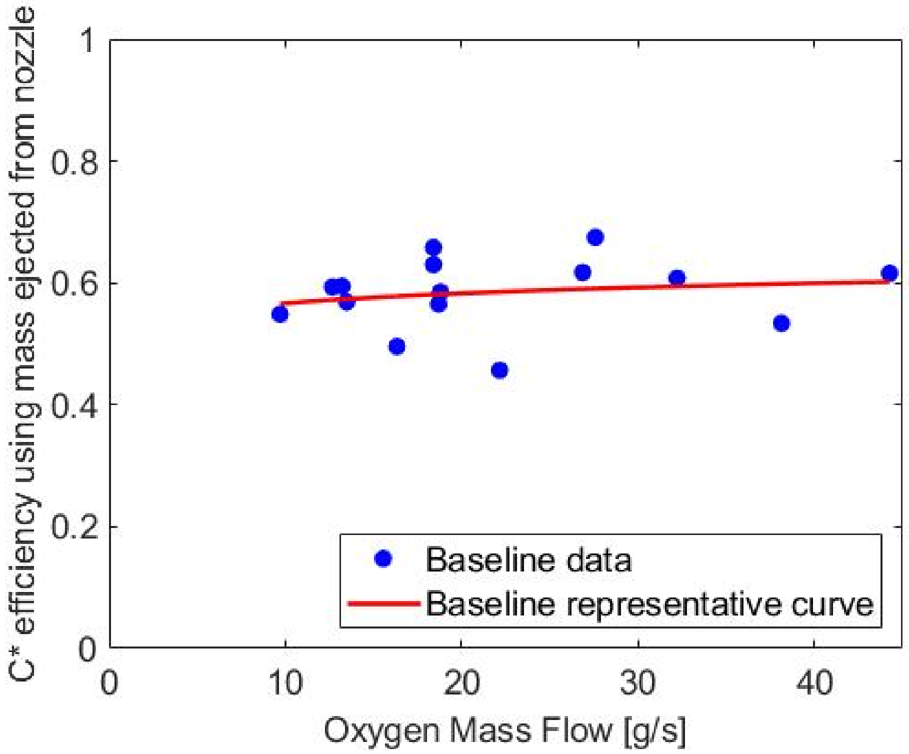

Figure 63 C* efficiency for baseline paraffin grains using mass ejected from nozzle.

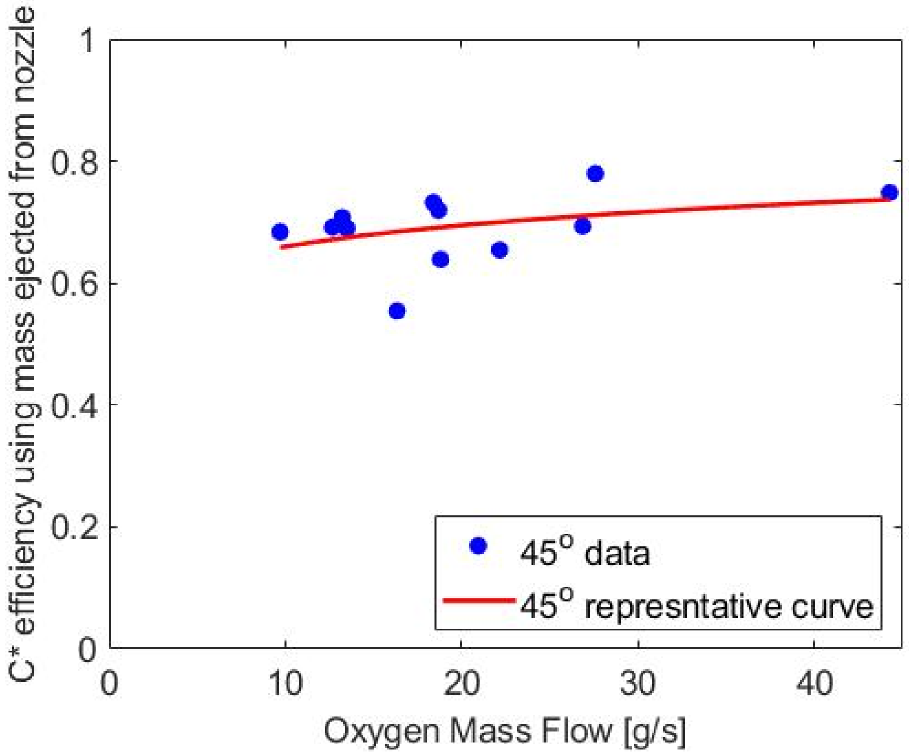

Figure 64 C* efficiency for 45^o grains using mass ejected from nozzle.

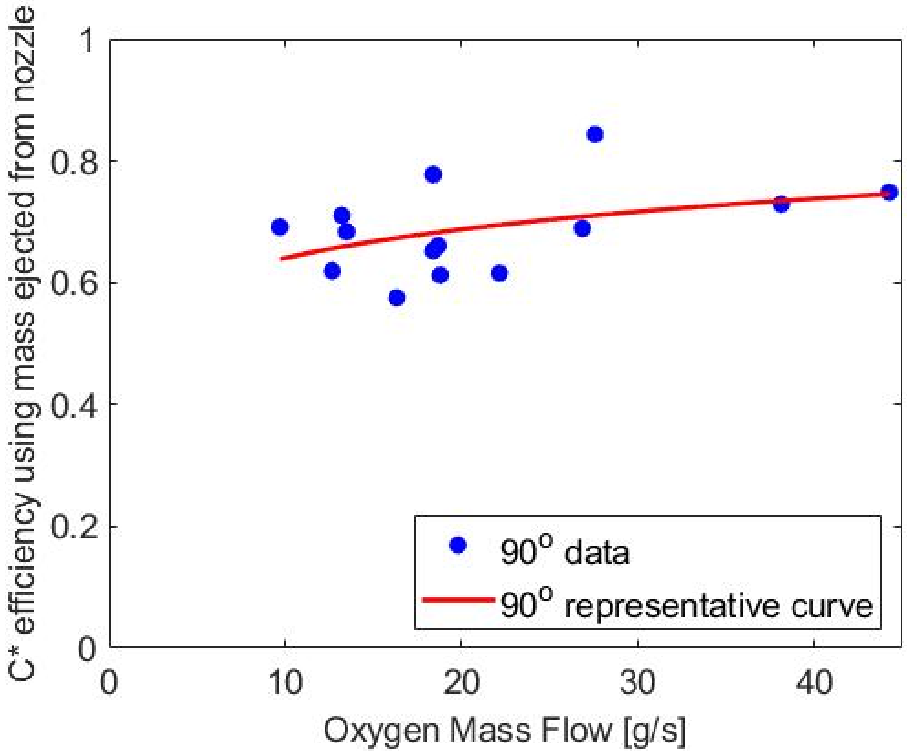

Figure 65 C* efficiency for 90° grains using mass ejected from nozzle.

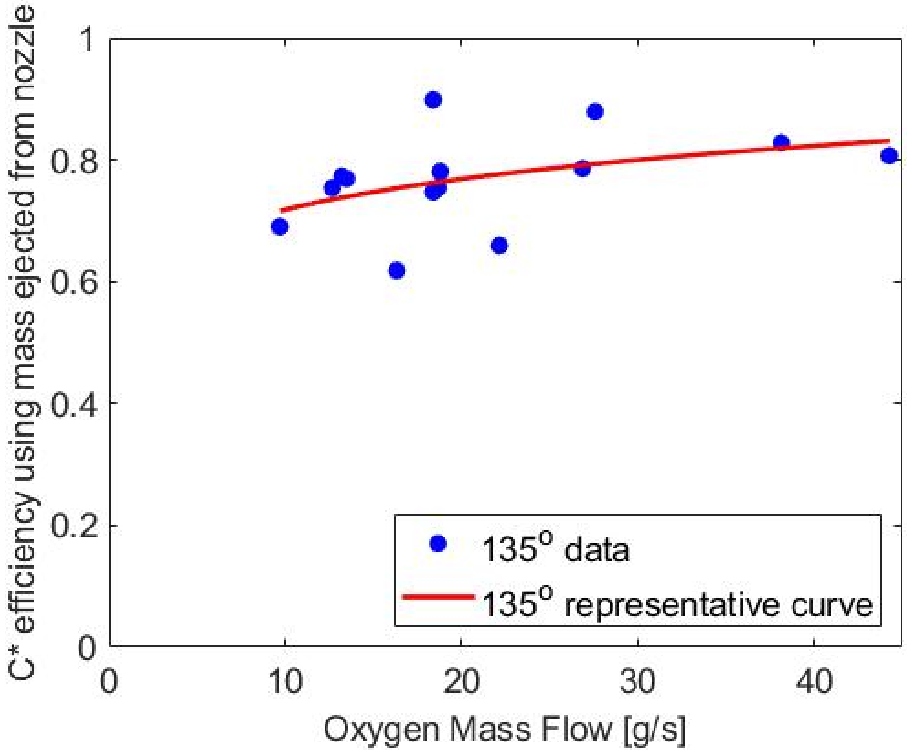

Figure 66 C* efficiency for 135° grains using mass ejected from nozzle.

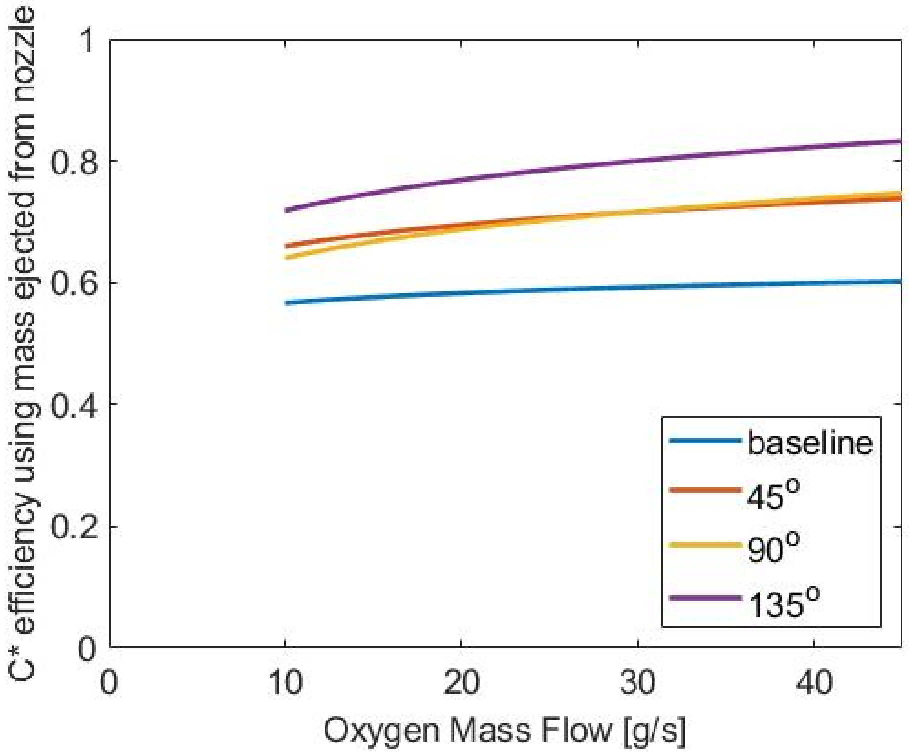

Figure 67 Comparison of C* curves using mass ejected from nozzle.

In an actual rocket, it is likely that the mass that was remaining in the mixing chamber would be ejected due to acceleration of the vehicle as well as gravity, so it is likely that C* efficiency would be somewhere between what is seen for the two cases shown.

5. Conclusions

- A method of successfully manufacturing hybrid fuel grains consisting of ABS skeletons that were manufactured using commercially available FDM additive manufacturing technology and cast paraffin wax was developed

- Paraffin Wax was selected due to the following properties
  - High regression rate when compared to Classic Hybrid Fuels
  - Low cost
  - Availability
  - Ease of handling
  - Storability

- Testing of paraffin grains with added ABS skeletons showed significant increases in regression rate, mixing efficiency, and combustion efficiency when compared to paraffin grains without added structure. Functionally acting as a lighter weight integral mixing chamber that simultaneously increases the regression rate of the fuel.

- This research was fairly novel as to our knowledge, only one other experiment has utilized additive manufacturing technology to increase the regression rate of paraffin wax, but that research did not demonstrate added mixing efficiency to go along with the added regression rate, and additionally was focused on inducing a rotation to the flow. This added performance has several possible applications including improving the volumetric loading factors in systems already using Paraffin fuels, such as the Peregrine Sounding rocket program or in research such as that being conducted by Daniel Kormornik, into the use of Paraffin fuel in a gas generator for a Ducted rocket, since the added regression rate allows for even lower ϕ values then previously tested with the same grain length.

- Regression rates were experimentally found to be the following

$$\dot{r}_{baseline}\left[\frac{mm}{s}\right] = .501 \cdot \left(G_{ox}\left[\frac{kg}{m^2 \cdot s}\right]\right)^{.198} \tag{23}$$

$$\dot{r}_{45\ degrees}\left[\frac{mm}{s}\right] = .678 \cdot \left(G_{ox}\left[\frac{kg}{m^2 \cdot s}\right]\right)^{.162} \tag{24}$$

$$\dot{r}_{90\ degrees}\left[\frac{mm}{s}\right] = .6 \cdot \left(G_{ox}\left[\frac{kg}{m^2 \cdot s}\right]\right)^{.222} \tag{25}$$

$$\dot{r}_{135\ degrees}\left[\frac{mm}{s}\right] = .486 \cdot \left(G_{ox}\left[\frac{kg}{m^2 \cdot s}\right]\right)^{.295} \tag{26}$$

6. Future Work

Future recommended research includes:

- Tests of longer grains to confirm the theory that the low exponents observed in this research were in fact due to the length of the grains and the lack of cooling on the test stand. Additionally, ceramic insulation plates could be inserted between the end walls of the grains and the metal casing to further remove this source of error.
- Tests of grains with varying lengths of the paraffin segments in order to investigate the possible link between paraffin segment length and average regression of the grain.
- Slab burner experiments to verify the assumption that the mechanism behind the increased regression rates is indeed similar to that observed previously by Gany et al. (Gany and Manheimer-Timnat 1972).
- Investigation of the effectiveness of grains manufactured in this technique for usability in a Hybrid gas generator as in Komornik's work.
- Investigation of the possible use of catalytic powders embedded in either the ABS skeleton or the Paraffin in order to obtain hypergolic ignition with Hydrogen Peroxide.
- Investigation of the possible use of aluminum powders embedded in either the ABS skeleton or the Paraffin in order to further increase performance of the fuel.
- Investigation into the use of alternate ABS formulations, or even other thermoplastics for the support structure in order to improve combustion of support structure.
- Since the exponent of the regression rate appears to be strongly linked to the angle of the skeleton, this could provide for a method of obtaining a constant O/F ratio through a burn by varying the angle of the skeleton as a function of radius, thus allowing for higher regression rates then would be possible by simply using an exponent of 0.5. This warrants further investigation.

References

Air Force Propulsion Directorate. 1990's.

Armold, D., E. J.. Boyer, K. K. Kuo, J. D.. DeSain, T. J. Curtiss, and J. K. Fuller. 2013. "Test of Hybrid Rocket Fuel Grains with Swirl Patterns Fabricated Using Rapid Prototyping Technology." *AIAA 2013-4141, 49th AIAA/ASME/SAE/ASEE Joint Propulsion Conference.* San Jose, CA: AIAA. doi:10.2514/6.2013-4141.

n.d. *Bowden extruder vs direct drive extruder.* Accessed July 2018. http://3dprinterpower.com/bowden-extruder-vs-direct-extruder-showdown/.

Castaneda, D. A., and B. Natan. 2018. "Experimental Investigation of the hydrogen peroxide-solid hydrocarbon hypergolic ignition." *Acta Astronautica.* doi:10.13009/EUCASS2017-107.

DeSain, J. D., B. B. Brady, K. M. Meltzer, T. J. Curtiss, and T. V. Albright. 2009. "Tensile Tests of Paraffin Wax for Hybrid Rocket Fuel Grains." *AIAA 2009-5115, 45th AIAA/ASME/SAE/ASEE Joint Propullsion Conference & Exhibit.* Denver, Colorado. doi:10.2514/6.2009-5115.

Doran, E., J. Dyer, M. Marzoña, A. Karabayaglu, G. Zilliac, R. Mosher, and B. Cantwell. 2009. "Status Update Report for the Peregrine Sounding Rocket Project: Part III." *AIAA 2009-4840, 45th AIAA/ASME/SAE/ASEE Joint Propulsion Conference & Exhibit.* Denver, CO. doi:10.2514/6.2009-4840.

Dyer, J., E. Doran, Z. Dunn, K. Lohner, C. Bayart, A. Sadhwani, G. Ziliac, B. Cantwel, and A. Karabeyoglu. 2007. "Design and Development of a 100 km Nitrous Oxide/Paraffin Hybrid Rocket Vehicle." *AIAA 2007-5362, 43rd AIAA/ASME/SAE/ASEE Joint Propulsion Conference & Exhibit.* Cincinnati, OH. doi:10.2514/6.2009-4840.

Dyer, J., G. Zilliac, E. Doran, M. T. Marzona, K. Lohner, E. Karlik, B. Cantwell, and A. Karabeyoglu. 2008. "Status Update Report for the Peregrine 100km Sounding Rocket Project." *AIAA 2008-4829, 44th AIAA/ASME/SAE/ASEE Joint Propulsion Conference & Exhibit.* Hartford, CT. doi:10.2514/6.2008-4829.

Fuller, Jerome K., Daniel A. Ehrlich, Paul C. Lu, Ryan P. Jansen, and Justin D. Hoffman. 2011. "Advantages of Rapid Prototyping for Hybrid Rocket Motor Fuel Grain

Fabrication." *AIAA 2011-5821, 47th AIAA/ASME/SAE/ASEE Joint Propulsion Conference & Exhibit.* San Diego, California. doi:10.2514/6.2011-5821.

Gany, A., and Y. Manheimer-Timnat. 1972. "Parametric Study of a Hybrid Rocket Motor." *Israel Journal of Technology* 1-2: 85-96.

1992. In *Mechanics and Thermodynamics of Propulsion*, by Philip Hill and Carl Peterson, 598. Addison-Wesley Publishing Company.

Karabeyoglu, M. A., and B. J. Cantwell. 2002. "Combustion of Liquefying Hybrid Propellants: Part 2 Stability of Liquid Films." *Journal of Propulsion and Power* 18: 621-630. doi:10.2514/2.5976.

Karabeyoglu, M. A., B. J. Cantwell, and D. Altman. 2001. "Development and Testing of Paraffin-Based Hybrid Rocket Fuels." *AIAA 2001-4503, 37th AIAA/ASME/SAE/ASEE Joint Propulsion Conference and Exhibit.* Salt Lake City. doi:10.2514/6.2001-4503.

Karabeyoglu, M. A., D. Altman, and B. J. Cantwell. 2002. "Combustion of Liquefying Hybrid Propellants: Part 1." *Journal of Propulsion and Power* 18: 610-620. doi:10.2514/2.5975.

Kim, S., J. Lee, H. Moon, H. Sung, J. Kim, and J. Cho. 2010. "Effect of Paraffin-LDPE Blended Fuel in Hybrid Rocket Motor." *AIAA 2010-7031, 46th AIAA/ASME/SAE/ASEE Joint Propulsion Conference & Exhibit.* Nashville, TN. doi:10.2514/6.2010-7031.

Komornik, D. 2014. "Study of a Hybrid Gas Generator for a Ducted Rocket, M.Sc." Haifa: Technion- Israel Institute of Technology, May.

Kormornik, D., and A. Gany. 2018. "Experimental Investigation of a Paraffin/Nano-Aluminum Hybrid Rocket." *58th Isral Annual Conference on Aerospace Sciences.* Tel-Aviv & Haifa, Israel. 895-903.

Lee, C., Y. Na, and G. Lee. 2005. "The Enhancement of Regression Rate of Hybrid Rocket Fuel By Helical Grain Configuration and Swirl Flow." *AIAA 2005-3906, 41st AIAA/ASME/SAE/ASEE Joint Propulsion Conference & Exhibit.* Tuscon, Arizona. doi:10.2514/6.2005-3906.

Medina, LDA. 2010. "Export Product Data Paraffin Waxes PW-624." October. Accessed 2018. http://www.medinatex.com/fichas/ft_parafina_PW624.pdf.

NASA Glenn Research Center. n.d. *Mass Flow Choking.* Accessed 2018. https://www.grc.nasa.gov/www/K-12/airplane/mflchk.html.

Ning, F., W. Cong, J. Qiu, J. Wei, and S. Wang. 2015. "Additive Manufacturing of Carbon Fiber Reinforced Thermoplastic Composites Using Fused Deposition Modeling." *Composites Part B: Engineering* 80: 369-378. doi:10.1016/j.compositesb.2015.06.013.

n.d. "n-Paraffins." *chemicalland21.* Accessed 2018. http://www.chemicalland21.com/petrochemical/n-PARAFFINS.htm.

Rahman, M., N. R. Schott, and L. K. Sadhu. 2016. "Glass Transition of ABS in 3D Printing." *Comsol Conference.* Boston.

Raiano, M. 2013. *Aerospace Engineering.* November 21. Accessed February 21, 2018. http://www.aerospacengineering.net/?p=1255.

n.d. *Science Learning Hub.* Accessed 2018. https://www.sciencelearn.org.nz/resources/393-types-of-chemical-rocket-engines.

Seyer, W.. F., R. F. Patterson, and J. L. Keays. 1944. "The Density and Transition Points of the n-Paraffin Hydrocarbons." *Journal of the American Chemical Society* 179-182.

Shin, K. H, C. Lee, S. Y. Chang, and J. Y. Koo. 2005. "The Enhancement of Regression Rate of Hybrid Rocket Fuel by Various Methods." *AIAA 2005-359, 43rd AIAA Aerospace Sciences Meeting and Exhibit.* Reno, Nevada. doi:10.2514/6.2005-359.

Weinstein, A,, and A. Gany. 2011. "Investigation of Paraffin-Based Fuels in Hybrid Combustors." *International Journal of Energetic Materials and Chemical Propulsion* 10: 277-296.

Whitmore, S. A., S. D. Walker, and D. P. Merkley. 2015. "High Regression Rate Hybrid Rocket Fuel Grains with Helical Port Structures." *Journal of Propulsion and Power* 31 (6): 1727-1738.

Whitmore, S. A., Z. W. Peterson, and S. D. Eilers. 2011. "Analytical and Experimental Comparisons of HTPB and ABS as Hybrid Rocket Fuels." *AIAA 2011-5909, 47th AIAA/ASME/SAE/ASEE Joint Propulsion Conference & Exhibit.* San Diego, California. doi:10.2514/6.2011-5909.

Ziliac, G., B. S. Waxman, B. Evans, A. M. Karabeyoglu, and B. Cantwell. 2014. "Peregrine Hybrid Rocket Motor Development." *AIAA 2014-3870, 50th AIAA/ASME/SAE/ASEE Joint Propulsion Conference.* Cleveland, OH. doi:10.2514/6.2014-3870.

Ziliac, G., B. S. Waxman, J. Dyer, M. A. Karabeyoglu, and B. Cantwell. 2012. "Peregrine Hybrid Rocket Motor Ground Test Results." *AIAA 2012-4017, 48th AIAA ASME/SAE/ASEE Joint Propulsion Conference & Exhibit.* Atlanta Georgia. doi:10.2514/6.2012-4017.

Appendix A: Error Analysis

As the results presented in this thesis were largely experimental in nature and included the measuring and computing of several parameters, the accuracy of the instruments needs to be accounted for in presenting any results. Some results, such as lengths of grains as well as port diameters, were measured manually, whereas other results were collected electronically through pressure gauges connected to a measurement board, which in turn was collected through Labview. Since several parameters that were reported were calculated from several measurements each of which has their own individual error, the errors accumulate in the calculations.

Instrument Errors

- Time $\pm$ 0.1s
- Oxygen nozzle diameter $\pm$ 0.01 mm
- Combustion chamber exhaust nozzle $\pm$ 0.02 mm
- Grain length/ initial port diameter $\pm$ 0.02 mm
- Grain mass $\pm$ 1g
- Pressure gauges $\pm$ 0.3 bar

Error Calculations

The general term for statistical error can be seen in Eq. (23).

$$\varepsilon_F = \sqrt{\sum_{i=1}^{N}\left(\frac{\partial F}{\partial x_i}\cdot\varepsilon_i\right)^2} \; when\ F = (x_1, x_2, \dots, x_N) a\ general\ function \tag{23}$$

Mass Delta

$$\Delta m = m_i - m_f$$

Therefore

$$\varepsilon_{\Delta m} = \sqrt{\varepsilon_{m_i}^2 + \varepsilon_{m_f}^2} = \sqrt{1^2 + 1^2} = 1.4142$$

Regression Rate

The regression rate for the ABS and baseline paraffin grains was calculated from Eq. (24)

$$\dot{r} = \frac{r_f - r_i}{t_b} \tag{24}$$

r_i and t_b were both directly measured, however r_f was calculated with Eq. (9) using measurements for the initial and final masses, as well as the initial length of the grain and the initial diameter of the port as follows

$$r_f = \sqrt{\frac{\Delta m}{\rho_f \cdot \pi \cdot l} + \left(\frac{d_i}{2}\right)^2}$$

As such, the error in the final radius can be computed as follows

$$\varepsilon_{r_f} = \sqrt{\left(\frac{\frac{d_i}{4} \cdot \varepsilon_{d_i}}{\sqrt{\frac{\Delta m}{\rho_f \cdot \pi \cdot l} + \frac{d_i^2}{4}}}\right)^2 + \left(\frac{\frac{\varepsilon_{\Delta m}}{2 \cdot \rho_f \cdot \pi \cdot l}}{\sqrt{\frac{\Delta m}{\rho_f \cdot \pi \cdot l} + \frac{d_i^2}{4}}}\right)^2 + \left(-\frac{\frac{\Delta m}{2 \cdot \rho_f \cdot \pi \cdot l^2} \cdot \varepsilon_l}{\sqrt{\frac{\Delta m}{\rho_f \cdot \pi \cdot l} + \frac{d_i^2}{4}}}\right)^2}$$

Which can be simplified to

$$\varepsilon_{r_f} = \frac{\sqrt{\left(\frac{d_i}{4} \cdot \varepsilon_{d_i}\right)^2 + \frac{\varepsilon_{\Delta m}^2}{\left(2 \cdot \rho_f \cdot \pi \cdot l\right)^2} + \left(-\frac{\Delta m}{2 \cdot \rho_f \cdot \pi \cdot l^2} \cdot \varepsilon_l\right)^2}}{\sqrt{\frac{\Delta m}{\rho_f \cdot \pi \cdot l} + \frac{d_i^2}{4}}}$$

The regression rate error can be calculated as follows using Eq. (24) for the calculation of the regression rate

$$\varepsilon_{\dot{r}} = \frac{1}{t_b}\sqrt{{\varepsilon_{r_f}}^2 + {\varepsilon_{r_i}}^2 + \left(-\frac{\left(r_i - r_f\right) \cdot \varepsilon_{t_b}}{t_b}\right)^2}$$

Which can be solved relatively easily by inputting the values, here for the lowest regression rate observed in the paraffin tests (test series 8)

$$\varepsilon_{r_f} = \frac{\sqrt{\left(\frac{d_i}{4}\cdot\varepsilon_{d_i}\right)^2 + \frac{\varepsilon_{\Delta m}^2}{\left(2\cdot\rho_f\cdot\pi\cdot l\right)^2} + \left(-\frac{\Delta m}{2\cdot\rho_f\cdot\pi\cdot l^2}\cdot\varepsilon_l\right)^2}}{\sqrt{\frac{\Delta m}{\rho_f\cdot\pi\cdot l} + \frac{d_i^2}{4}}}$$

$$= \frac{\sqrt{\left(\frac{22.26}{4}\cdot 0.02\right)^2 + \frac{1.4142^2}{(2\cdot 0.0009\cdot\pi\cdot 53.56)^2} + \left(-\frac{22.74}{2\cdot 0.0009\cdot\pi\cdot 53.56^2}\cdot 0.02\right)^2}}{\sqrt{\frac{22.74}{0.0009\cdot\pi\cdot 53.56} + \frac{22.26^2}{4}}}$$

$$= 0.282$$

Therefore

$$\varepsilon_{\dot{r}} = \sqrt{\left(\frac{0.282}{6.7}\right)^2 + \left(-\frac{0.02}{6.7}\right)^2 + \left(-\frac{(16.55409 - 11.13)\cdot 0.1}{6.7^2}\right)^2} = 0.0439$$

It should be noted that for the ABS grains, the initial radius of the subsequent tests was the final radius for the previous test, so some errors did accumulate from test 1 to the final test for each grain.

Skeleton Final radius

$$r_f = \frac{\frac{3.2}{\pi} + \sqrt{\left(\frac{3.2}{\pi}\right)^2 + 4\cdot\left(\frac{\Delta m}{\pi\cdot\rho_p\cdot l_p} - (r_i^2 + \frac{3.2}{\pi}\cdot r_i\right)}}{2}$$

$$= \frac{1.6}{\pi} + \sqrt{\frac{2.56}{\pi^2} + \frac{\Delta m}{\pi\cdot\rho_p\cdot l_p} - r_i^2 + \frac{3.2}{\pi}\cdot r_i}$$

Therefore ($\varepsilon_{r_i} = \sqrt{\left(\frac{\varepsilon_{d_i}}{2}\right)^2} = \frac{\varepsilon_{d_i}}{2} = 0.01$)

$$\varepsilon_{r_f} = \left(\left(\frac{\frac{\varepsilon_{\Delta m}}{\pi \cdot \rho_p \cdot l_p}}{\sqrt{\frac{2.56}{\pi^2} + \frac{\Delta m}{\pi \cdot \rho_p \cdot l_p} - r_i^2 + \frac{3.2}{\pi} \cdot r_i}} \right)^2 + \left(- \frac{\frac{\Delta m \cdot \varepsilon_{l_p}}{\pi \cdot \rho_p \cdot l_p^2}}{\sqrt{\frac{2.56}{\pi^2} + \frac{\Delta m}{\pi \cdot \rho_p \cdot l_p} - r_i^2 + \frac{3.2}{\pi} \cdot r_i}} \right)^2 + \left(\frac{\left(2 \cdot r_i + \frac{3.2}{\pi}\right) \cdot \varepsilon_{r_i}}{\sqrt{\frac{2.56}{\pi^2} + \frac{\Delta m}{\pi \cdot \rho_p \cdot l_p} - r_i^2 + \frac{3.2}{\pi} \cdot r_i}} \right)^2 \right)^{\frac{1}{2}}$$

Which can be simplified to

$$\varepsilon_{r_f} = \frac{\sqrt{\left(\frac{\varepsilon_{\Delta m}}{\pi \cdot \rho_p \cdot l_p}\right)^2 + \left(\frac{\Delta m \cdot \varepsilon_{l_p}}{\pi \cdot \rho_p \cdot l_p^2}\right)^2 + \left(2 \cdot r_i + \frac{3.2}{\pi}\right)^2 \cdot \varepsilon_{r_i}^2}}{\sqrt{\frac{2.56}{\pi^2} + \frac{\Delta m}{\pi \cdot \rho_p \cdot l_p} - r_i^2 + \frac{3.2}{\pi} \cdot r_i}}$$

Fuel Mass Flow Rate

Similar to the regression rate, the fuel mass flow rate is defined as

$$\dot{m}_f = \frac{\Delta m}{t_b}$$

Thus

$$\varepsilon_{\dot{m}_f} = \sqrt{\left(\frac{\varepsilon_{\Delta m}}{t_b}\right)^2 + \left(-\frac{\Delta m}{t_b^2}\right)^2} = \frac{1}{t_b} \cdot \sqrt{\varepsilon_{\Delta m}^2 + \left(\frac{\mathrm{\Delta m} \cdot \mathrm{\varepsilon_{t_b}}}{\mathrm{t_b}}\right)^2}$$

Oxygen Nozzle Area

$$A_t = \frac{\pi}{4} \cdot d_i^2$$

Thus

$$\varepsilon_{A_t} = \sqrt{\left(\frac{\pi \cdot d_i \cdot \varepsilon_{d_i}}{2}\right)^2} = \frac{\pi \cdot d_i \cdot \varepsilon_{d_i}}{2}$$

Oxidizer Mass Flow Rate

$$\dot{m}_{ox} = \frac{A_t \cdot P_{ox}}{\sqrt{T_t}} \sqrt{\frac{\gamma_{ox}}{R_{ox}}} \left(\frac{\gamma_{ox} + 1}{2}\right)^{-\frac{(\gamma_{ox}+1)}{2(\gamma_{ox}-1)}} = A_t \cdot P_{ox} \cdot C$$

Thus

$$\varepsilon_{\dot{m}_{ox}} = \sqrt{\left(P_{ox} \cdot C \cdot \varepsilon_{A_t}\right)^2 + \left(A_t \cdot C \cdot \varepsilon_{P_{ox}}\right)} = C \cdot \sqrt{\left(P_{ox} \cdot \varepsilon_{A_t}\right)^2 + \left(A_t \cdot \varepsilon_{P_{ox}}\right)}$$

Average Oxidizer Mass Flux during test (spatial average)

$$G_{ox} = \frac{\dot{m}_{ox}}{\pi \cdot \left(\frac{r_i + r_f}{2}\right)^2} = \frac{4 \cdot \dot{m}_{ox}}{\pi \cdot \left(r_i + r_f\right)^2} = \frac{4 \cdot \dot{m}_{ox}}{\pi\left(r_i^2 + r_i \cdot r_f \cdot r_f^2\right)}$$

Thus

$$\varepsilon_{G_{ox}} = \frac{4 \cdot \sqrt{\varepsilon_{\dot{m}_{ox}}^2 + \dot{m}_{ox}^2 \cdot \left(\left(\frac{\left(2_{r_i} + r_f\right) \cdot \varepsilon_{r_i}}{\left(r_i + r_f\right)^2}\right)^2 + \left(-\frac{\left(2 \cdot r_f + r_i\right) \cdot \varepsilon_{r_f}}{\left(r_i + r_f\right)^2}\right)^2\right)}}{\pi \cdot \left(r_i + r_f\right)^2}$$

Average Oxidizer to Fuel ratio during test (O/F)

$$\frac{O}{F} = \frac{\dot{m}_{ox}}{\dot{m}_f}$$

Thus

$$\varepsilon_{\frac{O}{F}} = \sqrt{\left(\frac{\varepsilon_{\dot{m}_{ox}}}{\dot{m}_f}\right)^2 + \left(\frac{\dot{m}_{ox} \cdot \varepsilon_{\dot{m}_f}}{\dot{m}_f^2}\right)^2} = \frac{1}{\dot{m}_f} \cdot \sqrt{\varepsilon_{\dot{m}_{ox}}^2 + \left(\frac{\dot{m}_{ox} \cdot \varepsilon_{\dot{m}_f}}{\dot{m}_f}\right)^2}$$

Error summary

The following table details the minimum and maximum errors and percent errors of each measured and calculated value reported, since the ABS was used only for a baseline and was not relevant to the major results, the errors were not calculated.

Measurement	(min, max) value	(min, max) absolute error	(min, max) error percentage
Fuel mass delta [kg]	(0.0214,0.229)	0.0014	(0.62,6.60)
Test duration [s]	(6.3,6.9)	0.1	(1.45,1.59)
Grain lengths [m]	(0.0463,0.220)	2e-5	(0.0091,0.0432)
Initial port radii [m]	(0.0111, 0.0116)	1e-5	(0.0862,0.0901)
Final port radii [m]	(0.0166, 0.0229)	(2.05e-5,2.979e-4)	(0.09,1.76)
Regression rate [m/s]	(0.0008, 0.0017)	(1.378e-5,4.791e-4)	(1.48,5.47)
Fuel mass flow rate [kg/s]	(0.0032, 0.0337)	(2.112e-4,4.8e-4)	(1.39,6.76)
Oxygen nozzle area [m^2]	(1.003e-6, 2.987e-6)	(3.550e-8,6.126e-8)	(2.05,3.54)
Oxygen pressure [kPa]	(3.586e6, 6.8502e6)	30	(4.579e-4,8.407e-4)
Oxygen mass flow rate [kg/s]	(0.0096, 0.0455)	(3.395e-4,9.344e-4)	(2.0513,3.5398)
Oxygen mass flux [kg/s*m^2]	(14.2826, 59.5028)	(0.4767,1.2991)	(1.96,3.56)
Oxidizer to Fuel ratio	(0.7477,8.5679)	(0.0250,0.4271)	(2.9008,7.3185)

המחקר נעשתה בהנחיית פרופ׳ בנבניסטה נתן בפקולטה להנדסת אוירונוטיקה וחלל.

המחקר נתמך ע״י קרן הטכניון למחקר בטחוני ע״ש פיטר מאנק.

אני מודה לטכניון על התמיכה הכספית הנדיבה בהשתלמותי.

חקירת דלקים על בסיס פרפין – ABS המיוצרים ע״י מדפסת תלת-ממד למנועים היברידיים רקטיים

חיבור על מחקר

לשם מילוי חלקי של הדרישות לקבלת התואר מגיסטר
למדעים בהנדסת האוירונוטיקה וחלל

יעקב ברסלר

הוגש לסנט הטכניון - מכון טכנולוגי לישראל

אב תשע״ח חיפה אוגוסט 2018

חקירת דלקים על בסיס פרפין – ABS המיוצרים ע״י
מדפסת תלת-ממד למנועים היברידיים רקטיים

יעקב ברסלר